BLOCKING, GAP FLOW AND MOUNTAIN WAVE INTERACTION ALONG THE COASTAL ESCARPMENT OF SOUTH AFRICA

by

Markus Geldenhuys

Submitted in partial fulfilment of the requirements for the degree

Masters of Science (Meteorology)

in the

Department of Geography, Geoinformatics and Meteorology

Faculty of Natural and Agricultural Sciences

UNIVERSITY OF PRETORIA

May 2018

SUMMARY

BLOCKING, GAP FLOW AND MOUNTAIN WAVE INTERACTION ALONG THE COASTAL ESCARPMENT OF SOUTH AFRICA

by

Markus Geldenhuys

Supervisor: Dr Liesl L. Dyson
Mr Deon van der Mescht
Department: Geography, Geoinformatics and Meteorology
Faculty: Natural & Agricultural Sciences
University: University of Pretoria
Degree: Master of Science (Meteorology)

Keywords: Blocking, Gap flow, Mountain wave, Turbulence, Experimental design, Dronesonde, Mountain wave formation criteria, Scorer parameter, Bernoulli equation, expansion fan, rotor, small-scale topography

ABSTRACT

A fatal light aircraft crash, within the Kareedouw mountains, highlighted the need to equip forecasters with the knowledge of the turbulence produced when wind flow encounters complex small-scale terrain near a cold front. With this in mind, an experiment was designed, according to the 6 W's (*why, who, where, when, what, whereby*) of design, to measure and address the unanswered questions regarding blocking, gap flow and mountain waves. Experiments were conducted with party balloons, dronesondes, dropsondes, thethersondes, parasails, simultaneous ascents and smoke grenades within the Kareedouw Pass. The topographical extent of the pass is the smallest where such a field experiment have ever been conducted.

Data were collected during six radiosonde field experiments and from an installed Automatic Weather Station network. Numerous parameters were calculated, where features were successfully characterised by the; Burger-, Froude number, Froude derived height scale and thermal wind equation. The upwind blocking region rendered the Bernoulli equation, which governs gap flow, unusable. Gap flow was identified by pressure- and temperature gradients during non-blocking and weak synoptic conditions.

The nocturnal inversion positively influenced gap flow, in a Venturi-type effect. Mountain wave trapping criteria and the Scorer parameter were ineffectual, due to the constantly changing and unstable upwind conditions. Turbulence was identified using potential temperature, cumulative normalised ascent rate, Ellrod Turbulence Index, vorticity, Richardson number, standard deviation from the gust and also by subjectively judging the wind directional and speed shear.

Blocking jets reached wind speeds up to 26ms^{-1} producing virtually no turbulence with scales of 600m deep, 80km wide and penetrating to 30km downwind of its exit region. The blocking wind speed measured second strongest wind speed, second to the ridge; (44.7ms^{-1}) due to the compressional effect. The blocking jet changed the synoptic scale surface wind and sea-level pressure, while driving gap flow and altering the mountain wave formation criteria; via a dynamic barrier. Gap flow, weakened the blocking region and measured below average wind speeds, while remaining the most turbulent feature. Phenomena observed at the gap exit included, divergence, hydraulic jump/expansion fan, eddies, maximum updraft and downdraft observations as well as large wind directional and speed shear.

Mountain waves, and its associated severe rotors, were found to be the second most turbulence producing feature and measured the most severe ever measured in South Africa, while being the smallest in wavelength and amplitude. Mountain wave formation criteria were updated given that mountain waves were observed during previously defined unfavourable conditions. Erratic-moving and complex-shaped mountain waves formed during unstable conditions with the wind almost perpendicular to the ridge. Severity of these mountain waves was found to be unpredictable; a nomogram or numerical weather prediction product is suggested. The results of this study are widely applicable, from the aviation industry to the renewable energy sector. Pilots are recommended, to keep a ground clearance of at least 1.5-2 times the highest topography; in a 10km upwind radius. It is recommended that forecasters keep in mind the blocking-induced dynamic barrier and to not exclude mountain waves under unstable conditions as well as to use a cross-barrier wind speed ≥7ms^{-1}.

I, Markus Geldenhuys declare that the dissertation, which I hereby submit for the degree MSc Meteorology at the University of Pretoria, is my own work and has not previously been submitted by me for a degree at this or any other tertiary institution.
SIGNATURE:……M. G……
DATE: ……04/05/2018……

ACKNOWLEDGEMENT

I would like to express my sincere gratitude to:

- God for providing me with a sound mind and ability to have completed this study.
- Eshanè Geldenhuys, my loving wife, for all her support, encouragement and all the proof reading into the late hours of the evening. Without your support, this would not have been possible!
- Dr LL Dyson, my Academic supervisor, for all her guidance and support during the project.
- Mr D van der Mescht, my field work supervisor, for all his assistance, guidance and patience under trying conditions during the field campaign. Climbing the gruelling Africa Peak multiple times in extreme weather conditions; ranging from 40°C in temperature to -7°C apparent temperature and 160km/h winds.
- Mr E Engelbrecht, for always availing himself during field campaigns and for not complaining to climb Africa Peak during 160km/h winds and -7°C apparent temperature.
- The late Prof. J van Heerden, for teaching me everything I know with regards to experiment design. We will miss him dearly.
- Ms A Demertzis and Ms K Oxley, the South African Weather Service Library staff, for all the assistance in digging up all the un-digitised reading material that formed the basis of this dissertation.
- Ms J Savy for the compilation of Figure 6.1.
- Mr H van Niekerk and the South African Weather Service Eastern Cape forecasting team, without your support and standing in for my shifts, this project would have been a failure.
- South African Weather Service for the time you provided me with and the study bursary.
- InterMet Africa Systems for sponsoring 20 radiosondes for my use and for Air Liquide for sponsoring Hydrogen gas.

TABLE OF CONTENTS

LIST OF SYMBOLS AND ABBREVIATIONS

A	Cross-sectional area
Agl	Above ground level
Amsl	Above mean sea level
AWS	Automatic Weather Station
B	Burger number
CAA	Civil Aviation Authority
CAT	Clear air turbulence
cm	Centimeter
c_p	Specific heat for dry air at constant pressure
CSIR	Council for Scientific and Industrial Research
DEF	Deformation
DSH	Shearing deformation
DST	Horizontal stretching deformation
E	East
ERA	European Re-analysis
ETI	Ellrod Turbulence Index
f	Coriolis parameter
F_{Gas}	Force of gas
$F_{Gravity}$	Force of gravity
F_M	Froude calculated to mountain top
Fr	Froude
F_W	Force of wind
g	Gravitation 9.81ms^{-1}
GMT	Greenwich Meridian Time
H	Depth of lower layer

h	Height difference
h_m	Mountain height
hPa	Hectopascal
Hrs	Hours
h_1	Froude derived height scale
ICAO	International Civil Aviation Organization
J	Joule
JB	Joubertina
K	Kelvin
k	Horizontal wavenumber
kg	Kilogram
l	Scorer parameter
L_M	Mountain halfwidth
L_R	Rossby Radius
m	Meter
m^2	Square meter
m^3	Cubic meter
Min	Minute
ms^{-1}	Meters per second
N	Brunt-Väisälä frequency
Nw	Newton
NWP	Numerical Weather Prediction
p	Pressure
PB	Plettenberg Bay
PE	Port Elizabeth
Q-GIS	Quantum GIS
R	Gas constant

Ri	Richardson number
S	South
s	Second
T	Temperature
TTK	Tsitsikamma
T_V	Virtual Temperature
U	Total wind vector in i, j and k directions
u	u wind speed
ù	Barrier corrected along-barrier wind speed
V	Total wind speed
V	v wind speed
ѵ̀	Barrier corrected cross-barrier wind speed
Vol	Volume
VWS	Vertical wind shear
W	Vertical component of flow vector
X	X-direction
Y	Y-direction
Z	Z-direction (vertical)
$\bar{\theta}$	Potential temperature (overbar indicates a layer Average)
∅	Latitude
σ	Variability
σ^2	Standard deviation
ρ	Density
η	Vorticity
∆	Delta
∇	Nabla operator

π	Pie = 3.14
°	Degrees from north
°C	Degrees Celsius
’	Minutes
’’	Seconds
<	Less than
>	Greater than
≤	Less than and equal
≥	Greater than and equal
≫	Much greater than
≪	Much less than
%	Percentage

LIST OF FIGURES

LIST OF TABLES

LIST OF EQUATIONS

CHAPTER 1 : INTRODUCTION

1.1 BACKGROUND

On 16 December 2015, a Cessna 182Q aircraft crashed en route from Graaff-Reinet to Plettenberg Bay, killing two passengers and injuring the pilot. The crash took place near Kareedouw in the Kareedouw-Tsitsikamma Mountains, South Africa (A in Figure 1-1). The pilot reported severe turbulence which knocked him unconscious moments before the crash. Analysis of meteorological information revealed that mountain waves were present, and the associated turbulence was most likely the cause of the crash (Van der Mescht & Geldenhuys, 2017). Other turbulence producing processes in the area included blocking and gap flow. This document is a description of the experiment designed to measure these processes, the observations made and the calculated parameters explaining these processes and the turbulence generated.

According to the Australian Government (2014), turbulence is a normal, frequent and a threatening phenomenon. Turbulence is driven by kinetic energy and is handed down from larger to smaller masses until finally converted to thermal energy at molecular scale (American Meteorological Society, 2012; Ahmad & Proctor, n.d.). Turbulence is defined as having the attribute of rapid temperamental changes through all three velocity components. For this to take place, the horizontal and vertical wind component needs to change, producing wind shear (American Meteorological Society, 2012). In aviation wind shear is responsible for the most weather-related in-flight injuries. Besides threatening the structural integrity of a light aircraft, wind shear may cause flying luggage or even, the pilot to lose control of the aircraft; both a threat to passengers and crew (Australian Government, 2014). Other effects of turbulence include increased flying time, due to reduced airspeed and increased fuel consumption. This translates into an economic impact, combined with a negative public image - an uncomfortable flight arriving late (Ellrod, 1992 cited in De Villiers & Van Heerden, 2001). A $100 million is spent annually on wind-shear-related injuries, by the worldwide aviation industry (Australian Government, 2014).

“Turbulence is a hazard to both commercial and general aviation” (Uhlenbrock et al., 2006). In 2014, a commercial pilot crashed, into the Tsitsikamma Mountains (A in Figure 1-1), while crop spraying in a Cessna A188B. The pilot experienced a significant loss in airspeed and inevitably crashed into the side of the mountain. According to Civil Aviation Authority (CAA), this crash was a product of mountain wave turbulence (CAA, n.d.). Multiple

other CAA Incident Reports of crashes exist; all relating to turbulence of which mountain wave turbulence is most prominent. Not one CAA Accident and Incident Report were found mentioning gap flow or blocking. This indicates one of two things; either, the phenomena are rarely hazardous enough to result in a crash, or, the phenomena is unrecognized in the South African aviation industry.

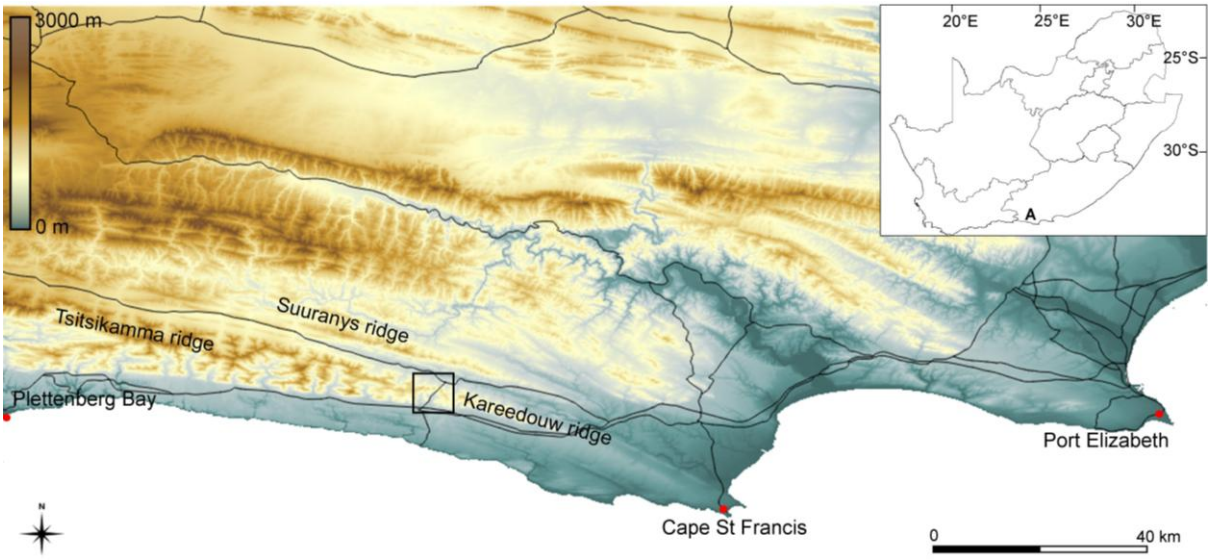

Figure 1-1: Topographical map surrounding the study site. The A in the inset indicates the crop spraying mountain wave induced crash site, the Kareedouw crash, and the study site in relation to the rest of South Africa. The study gap is indicated by the block.

1.2 MOTIVATION

Literature suggests three main wind flow patterns as wind encounters topography. These patterns are; blocking, gap flow and mountain waves. These regimes take form in isolation or in a combined ‘chaotic’ wind flow pattern. A blocking jet coming at a crosswind, in relation to the gap jet, provides a significant hazard to aircraft. Gap flow creates; a low-level jet, confluence and difluence; pushing an already slightly tilted plane into a wayward direction. The mountain wave regime, as defined by Gaberšek & Durran (2004), is a good example of a combination of gap flow and mountain waves. During a low-level flight into a mountain-wave-gap-flow environment, a pilot experiences a chaotic environment full of turbulence with constant increased and decreased flow over the wing. Exiting this environment into a blocking jet provides a new hazard; a possible severe jet coming at a 90° crosswind. Mountain waves create; small turbulent pockets of rotors, areas of increased and

decreased wind speeds as well as fluctuations in lift. A singular or combined effect of these can be catastrophic, if the pilot is unaware of the flow in mountainous terrain.

Unfortunately, gap flow is a phenomenon which is not recognised nor forecast in South Africa. According to UCAR (2012), gap flow is only accurately forecast by numerical weather prediction if a mesoscale model, with at least a few grid points inside the gap, is available. The South African Unified Model with a horizontal resolution of 1.5km (the finest resolution available to forecasters) (Landman, 2016), is usable to forecast gap flow in gaps wider than 3km. Most of the Eastern Cape mountain gaps are less than 1.5km wide, therefore; gap flow is extremely difficult to predict for operational forecasters. Numerical weather predictions with 'sufficient' resolution predicts blocking jets, given, it's such a 'large' scale phenomena that it alters synoptic conditions (Overland & Bond, 1995). No mountain wave numerical weather prediction support exists for operational forecasters in South Africa.

Until recently (Van der Mescht & Geldenhuys, 2017), the character and intensity of non-northwesterly driven mountain waves, were largely unknown in South Africa. Along the South Coast, these mountain waves take shape in westerly to southwesterly flow in the vicinity of a passing frontal system. The 16 December 2015 aircraft crash highlighted these southwesterly waves (which were previously regarded by forecasters as insignificant waves) as possibly severe (Van der Mescht & Geldenhuys, 2017).

Wind flow in a 'normal' mountainous terrain can be complicated. Making the terrain more complex, by adding a gap, and reducing the scale of the topography, creates an unstudied environment with a research problem. No observational study of blocking, gap flow and mountain waves, on such small-scale terrain, was found in literature; highlighting the urgency and extent of the research problem. This dissertation will aid in the forecasting and understanding of wind and turbulence in small-scale coastal and complex mountainous terrain. Some of the advantages of this dissertation include; improved forecasting by aviation forecasters, improved safety, expanding mountain wave research in South Africa, initiating blocking and gap flow research in South Africa, as well as improved understanding by pilots, flight schools and aeroplane builders.

1.3 AIMS AND OBJECTIVES

The first aim of this study is to design an experiment to measure blocking, gap flow and mountain wave interaction produced by southwesterly winds in small-scale terrain. The

second aim is to describe the turbulence created by the interaction of blocking, gap flow and mountain waves, over a complex, low-elevation, coastal mountain range.

In order to achieve these aims the following objectives will be applied:

- Set-up an experiment
- Analyse the synoptic conditions and observed data of events using multiple parameters (Froude, Rossby Radius, Scorer parameter, Ellrod Turbulence Index, Richardson Number and Horizontal Vorticity)
- Determine the characteristics of blocking, gap flow as well as mountain waves and compare with other studies

1.4 DISSERTATION OUTLINE

Chapter 2 includes an overview of wind flow in a mountainous terrain. A discussion of the processes involved (including, blocking, gap flow and mountain waves) and the physics behind these processes are included. This is followed by a literature review of the findings of other larger scale observational and numerical studies around the world.

In Chapter 3, data and methodologies employed to achieve the aims are discussed. This chapter creates a setting for the following chapters by, including the analysis of the study area, data collected and methods applied to obtain and analyse the data.

Experimental design is discussed in Chapter 4. A detailed account is given of the rationale of the experiment.

Chapter 5 covers all data analysis. Data analysis consists of an investigation of ‘longer-term’ data followed by a synoptic discussion of case studies on event days. This chapter incorporates the scrutiny of automatic weather station data, upper air observations and all calculations applied to the data.

Chapter 6 incorporates all discussions of data and data analysis. In this chapter, results are compared to other studies in South Africa and the rest of the world.

Chapter 7, the final chapter, comprise of the conclusions followed by this dissertations contribution to science, the study gaps identified, as well as the recommendations of this study.

CHAPTER 2 : LITERATURE REVIEW

In this chapter, literature regarding blocking, gap flow and mountain waves are discussed. The discussion begins where wind flow interacts with terrain and the outcome that ensues. This chapter considers the observations and different parameters proposed by other studies and which will be calculated in later chapters. Following this, turbulence indices and where available, severity classification methods of the relevant parameters are explored.

2.1 WIND FLOW INTERACTING WITH TERRAIN

Wind flow in a mountainous terrain can take many different patterns, three of these are; mountain waves, gap flow and blocking (Gaberšek & Durran, 2004). As wind approaches a barrier, firstly, the barrier blocks the wind, secondly, the wind takes the approach of least resistance around the barrier (gap flow) and lastly, if sufficient momentum is available, the wind overshoots the barrier creating mountain waves. In order to understand the three wind flow processes, a good understanding of stability is required.

Literature suggests that statically stable conditions are a pre-requisite for the parameters governing blocking, gap flow and mountain waves. Static stability refers to the ability of a parcel at equilibrium to become turbulent or laminar, as buoyancy affects it. A statically unstable parcel tends to remain turbulent, while statically stable refers to a parcel that wishes to remain laminar. In unstable air, a turbulent parcel becomes less turbulent with time – as static instability is eliminated, except when an external force continues to destabilize the air (American Meteorological Society, 2012). The measure of stability applied by most equations is the Brunt-Väisälä frequency.

The Brunt-Väisälä frequency is the period a parcel takes to achieve one successful oscillation after displacement. Once a parcel of air is displaced it tends to return to equilibrium (usually its original position). As the parcel attempts to correct itself, it often overshoots its equilibrium and oscillates. The frequency is an indication of the strength of the buoyancy of that specific atmospheric layer. The Brunt-Väisälä frequency is measured in s^{-1} (N – Equation 2.1). The frequency is not defined for statically unstable air and is zero in statically neutral air (American Meteorological Society, 2012). The events discussed in this dissertation are not idealised cases and did not always display statically stable conditions. In these cases, a mixture between statically stable and statically unstable layers exists. Given

the lack of parameters for an unstable atmosphere, the Brunt-Väisälä frequency formed the basis of all calculations.

$$N=\sqrt{(g/\bar{\theta})(\frac{\partial\theta}{\partial z})}; \qquad \textit{Equation 2 . 1}$$

Where; θ = potential temperature ($\theta=T(\frac{1000}{p})^{R/Cp}$, $R=287JK^{-1}kg^{-1}$, $Cp=1004JK^{-1}kg^{-1}$), g = gravitation, $\bar{\theta}$ is the layer-averaged value over the depth of the layer and $\frac{\partial\theta}{\partial z}$ is the vertical gradient of the potential temperature.

To determine whether blocking, gap flow and mountain waves exist, the Brunt-Väisälä frequency is applied in the Froude number. The Froude number demonstrates the impact of terrain on wind flow (De Foy et al., 2006). Froude values (Equation 2.2) is divided into subcritical (Fr<1) and supercritical (Fr>1) values. Subcritical upwind Froude values indicate that the dominant airflow is around the mountain barrier (Wallace & Hobbs, 2006). Barry (1981) states that a smooth disturbance forms over the barrier but no lee waves forms for Fr≪1. Values approaching zero indicate upwind blocking of flow is complete, and transitional values indicate that a downstream hydraulic jump is possible.

$$Fr=\frac{\bar{v}}{Nh_m}; \qquad \textit{Equation 2 . 2}$$

$$h_1=\frac{\bar{v}}{N}; \text{ where Fr set to 1} \qquad \text{Equation 2 . 3}$$

Where; $\bar{v}$ = surface to mountaintop averaged wind component perpendicular to the mountain, h_m = the mountain height from surface to mountaintop and h_1= Froude derived height scale

2.1.1 Blocking

Blocking (also called windward ridging, barrier flow or cold air damming) is defined as the obstruction of statically stable upslope flow on the upwind side of a mountain barrier. The colder stable air has difficulty in passing over the barrier and is rather blocked, with a deflected low-level upwind jet as a result (American Meteorological Society, 2012; Overland & Bond, 1995). Blocking is characterized by an increase in wind speed, an increase in pressure (as cold air dams against the ridge) and a direction wind shift to parallel to the ridge. The increased pressure gradient enhances the low-level jet (also called barrier jet or blocking jet) while building it outward.

A blocking jet observed in British Columbia at Vancouver Island displayed a 500m deep vertical scale and a 40 - 50km horizontal scale. A distinct transition zone, less than 10km, was observed between the synoptic wind flow and the wind flow influenced by blocking. The Vancouver Island jet observed an increase from 10 to 15ms^{-1} in the along-barrier wind speed using a RADAR equipped aircraft (Overland & Bond, 1995).

Blocking was thoroughly observed in the Sierra Nevada mountains at California, employing; radiosondes, windprofilers and microwave satellite imagery. In these studies, a blocking jet was classified on two accounts. First by Smutz (1986 cited in Neiman et al. 2010), when the along-barrier (ù) wind displayed a maximum greater than 0ms^{-1}, below the mountain peak. Neiman et al. (2010) later identified blocking when the barrier aligned wind exceeded 12ms^{-1} with a decrease of at least 2ms^{-1}, between the jet maximum and the mountaintop. Another pre-requisite of blocking was a weak cross-barrier wind component, in fact; strong blocking cases were expected to display stagnant cross-mountain components with Froude values between zero and one. The speed profile of such a blocking jet was found to be virtually constant up the upwind slope (Figure 2-1; found by Parish (1982) and substantiated again by Neiman et al. (2010)). The direction profile of the blocking jet was rotated by 10° - 12° with height, the outcome is that the cross-mountain component becomes larger with an increase in height (Figure 2-2 c & d). In the same study, another blocking jet was classified using microwave satellite imagery; this jet has a narrow and long horizontal extent; <1000km by >2000km. Another observation included the blocking jet acting as a 'dynamic-barrier', altering the localized environment and processes up to well above the barrier (Neiman et al., 2010).

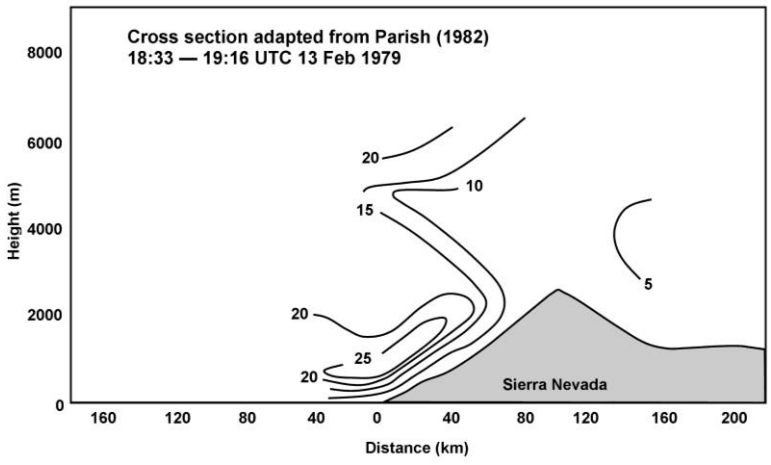

Figure 2-1: Blocking jet profile as observed by the Wyoming research aircraft on a case (13 February 1979). Neiman et al. (2010), observed a similar vertical profile. Adapted from: Parish (1982 cited in Neiman et al., 2010).

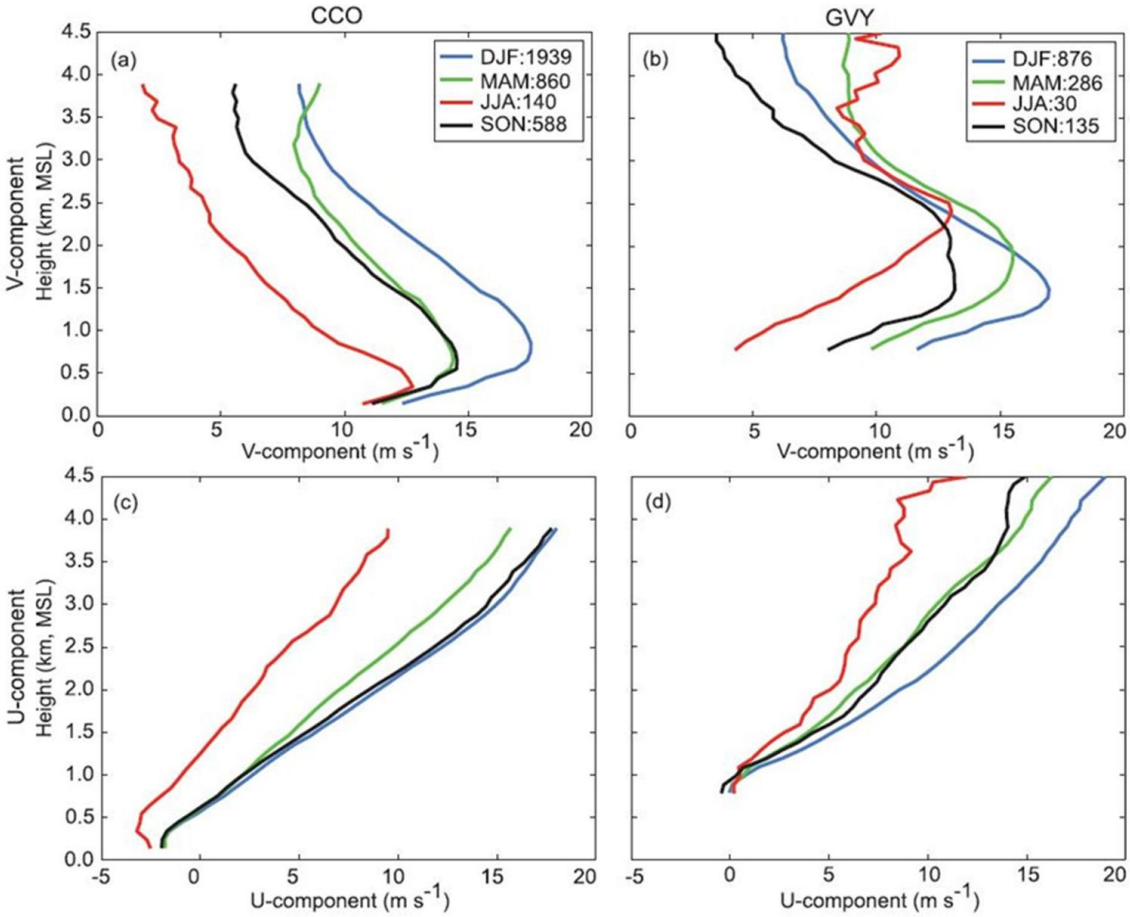

Figure 2-2: Wind profiles as observed by Neiman et al. (2010) using two windprofilers. The first, CCO, being in the valley (41m above mean sea level (amsl)), while the second, GVY, was 689m up the ridge; ridge top was taken at 3km. The V-component was the along-barrier wind and the U-component the cross-barrier component.

The Sierra Nevada blocking jet displayed a mean value of 17.5ms^{-1}. The maximum strength on average occurred between 500-1000m agl (translating to the lowest 15-35% of the mountain height), but always below the upwind peak (similar to Figure 2-1). At times, the jet became as strong as 50ms^{-1} at 1200m agl (Neiman et al., 2010).

Blocking has been observed to become so significant that it alters synoptic conditions on a small scale. During a blocking case, the synoptic mean sea level analysis was found to indicate that the isobars near the mountains be more parallel to the mountains than further off (Overland & Bond, 1995). Just as blocking influences synoptic conditions, synoptic conditions influence blocking. Pre- and post-frontal synoptic conditions were identified to lead to blocking (Overland & Bond, 1995; Chen & Smith, 1987). In the Sierra Nevada, blocking was mainly observed in pre-cold-frontal conditions. The strength of the blocking jet

portrayed a clear seasonality; being stronger in winter (as seen in Figure 2-2 a-d), simulating the climatology of extratropical cyclones. It was suggested that a pressure ridge maintains the blocking jet after the passage of the front (Neiman et al., 2010).

Parameters such as Froude, Burger, Rossby Radius and the thermal wind equation govern the characteristics of blocking. Two cases were measured by Overland & Bond (1995). The first case exhibited a good formation of a blocking jet, when Froude was less than 1 (when Equation 2.2 was calculated from surface to mountain top (F_m)). The second case displayed almost no increase in wind speed, when F_m~6. The good case observed an increase in wind speed of 5ms^{-1}, which was roughly consistent with the barrier perpendicular component. Assuming uniform wind speed and static stability, the vertical and horizontal scales of the jet were found comparable to theoretical calculations done (Overland & Bond, 1995).

To determine the different scales of the jet, Overland & Bond (1995) defined different hydrodynamic regimes. The regimes relate to the mountain Froude number (F_m) and the Burger number. The non-dimensional Burger number (Equation 2.4) indicates whether the slope is hydrodynamically steep. If $B \ll 1$ the flow is quasigeostrophic and the air flows over the mountain. If $0.1<B<1$ the influence of the mountain is semigeostrophic and the slope influences the wind, however, keeping a predominant flow over the ridge (Pierrehumbert & Wyman, 1985 cited in Overland & Bond, 1995). Where the slope is hydrodynamically steep ($B>1$), the momentum balance is seen as ageostrophic and the barrier becomes a 'wall' and blocking is in full force. Overland & Bond (1995) expects a blocking jet of maximum strength if $B>1$, F_m~1 and N is small.

$$B = h_m N / f L_m; \qquad \text{Equation 2 . 4}$$

Where; L_m is the mountain halfwidth, and f the Coriolis parameter ($2\left(7.292\times10^{-5}\right)\sin\emptyset$)

Blocking needs to be quantified if it occurs. The width of the jet (horizontal scale) is determined using the Rossby radius equation (Equation 2.5). The increase in along-barrier wind speed is calculated with the thermal wind equation (Equation 2.6), depending on which Froude condition is satisfied. The thermal wind calculated increase (ΔV) is added to the along-barrier speed to yield final jet strength (Overland & Bond, 1995). If no 'spilling' occurs over the mountain ($h_m<h_1$ – where Fr is set to one in Equation 2.2), the vertical scale of the jet is determined by the Froude derived height scale (Equation 2.3).

$$L_R = \left(\frac{Nh_m}{f}\right) F_m = \frac{\grave{v}}{f}; \text{ when } F_m < 1 \qquad \text{(condition 1) Equation 2 . 5}$$

$$L_R = L_m = \frac{Nh_m}{f}; \text{ when } F_m > 1 \qquad \text{(condition 2) Equation 2 . 5}$$

$$\Delta V = \frac{N^2 h^2}{fL} = \grave{v}; \text{ when } F_m < 1 \qquad \text{(condition 1) Equation 2 . 6}$$

$$\Delta V = h_m N; \text{ when } F_m > 1 \qquad \text{(condition 2) Equation 2 . 6}$$

Where; $\grave{v}$ = wind component perpendicular to the mountain

Blocking is not complete and the jet cannot reach maximum strength, or deformation starts to occur; if spilling does occur. Partially blocked airflow is another factor weakening a blocking jet. Spilling occurs during partially blocked conditions when the layer of blocked flow is deeper than the blocking barrier. Gaps scattered throughout a ridge is another means where blocked airflow can 'spill' to the lee-side, initiating gap flow. Overland & Bond (1995) found retardation in the blocking jet due to vertical or horizontal entrainment of less cold lower momentum air.

Parameters calculated to quantify and explain blocking includes; Froude Number, Froude derived height scale, Burger Number, Rossby Radius equation and the thermal wind equation.

2.1.2 Gap winds

Gap winds (also gap flow, gap jet, jet-effect wind or canyon wind) are classified as a low-level accelerated wind phenomenon. Momentum, thermal forcing or pressure-gradient force accelerates the wind through a gap or channel in the topography. Airflow in mountainous terrain with a gap is defined by Gaberšek & Durran (2004) according to three sub-regimes; upwind blocking-, linear- and mountain wave regimes. Where blocking and gap flow co-exist, lateral convergence and pressure gradient forces produce the maximum gap wind at the gap entrance. During a linear regime, almost no enhancement of flow is observed in the gap. Lastly, in a mountain wave regime, downward transport from mountain waves occurs, inducing strongest winds at the gap exit. Gap flow substantially influences aircraft and ship operations (University of Washington, 2014; Brennan et al., 2010).

Gap flow is frequently observed as cold post-frontal air is partially blocked by a mountain barrier (American Meteorological Society, 2012). The advection of dense, stable cold air is reluctant to ascend the barrier and prefer to advance through the gaps and valleys (Bradbury, 1992a). The accumulation of wind on the blocking side forms a localized high

pressure driving gap flow. The high pressure increases the pressure gradient (and pressure gradient force) between the upwind and lee side of the mountain. As the pressure gradient force increases the strength of the gap jet (the strongest core of wind emanating from the gap) increases and the jet extends further downstream (Colle & Mass, 2000). Similarly, the temperature gradient influences gap flow.

The passage of a cold front along the South Coast of South Africa enhances the pressure- and temperature gradient. The warm pre-frontal sector (with lower pressures) is located over the interior, while the coastal temperatures drop and the pressure rise due to post-frontal air. However, weak synoptic conditions also frequently result in gap flow. Whenever different air masses exist on either side of the gap, flow is triggered (Gaberšek & Durran, 2004). Over the Mexico basin, gap jets are mainly thermally forced. Temperature gradients as determined by radiosondes at different heights were found to correlate with different jet strengths (De Foy et al., 2006).

Globally, many gap flow studies were conducted (Table 2-1), however, none was found in South Africa. One of the earliest documented gap flow studies was done by Hurd (1929 cited in Pan & Smith, 1999) in the Tehuantepec Region Mexico. Early studies (such as Reed (1931) through to Jackson & Steyn (1994b)) comprised of weather station and radiosonde observations. Recent studies included the use of conventional weather stations combined with modernised technology; an aircraft tail Doppler RADAR (Colle & Mass, 2000), satellite-borne synthetic aperture RADAR (Pan & Smith, 1999), QuikSCAT scatterometer (Brennan et al., 2010), LIDAR and dropsondes (Marić & Durran, 2009). Recently modern studies consist of computerized studies (Gaberšek & Durran (2004) as well Zängl (2002)). The smallest-scale study found in literature was St. Vincent Island in the Caribbean, with an upper gap width of 5km.

Gap flow is measured, calculated, and quantified using various different techniques in numerous studies. Multiple methods exist to calculate the gap jet speed. Where the gap top is open (no ‘lid’ to restrict upward flow) the Venturi effect (conservation of energy as flow passes a constriction in topography; or parcel pressure decrease and increase in speed as it flows through the ‘gap’ (American Meteorological Society, 2012)) is not appropriate to quantify the jet. The Bernoulli equation is a more accurate method to explain wind flow in a restricted environment. The Bernoulli equation for incompressible fluids, (Equation 2.7) was found to overestimate the jet strength greatly. Gaberšek & Durran (2004) found the Bernoulli equation for compressible fluids (Equation 2.8) to be more accurate in estimating jet strength. The Bernoulli equation for compressible fluids assumes; acceleration takes place only if the temperature at the gap exit is lower than the temperature at the entrance.

Table 2 - 1: Previous gap flow studies, - indicates no data were found. Note the environmental wind is stronger than the gap jet in the Kareedouw gap (this dissertation); this was as a result of the blocking deflected jet, however, more on this in Section 6.2.

Name, region	Width (km)	Length (km)	Depth (m)	Environment wind/max jet (ms^{-1})	Reference
Chivela Pass, Mexico	40	220	±2000	-/33+	Brennan et al. (2010); University of Washington (2014)
Bora, Croatia	30	-	-	-	Smith (1987) cited in Pan & Smith (1999)
Hawaii, USA	10	-	-	-	Smith & Grubišić (1993)
St. Vincent, Caribbean	5	±6	600	-	Smith et al. (1997)
Wyoming Corridor, USA	50	-	-	-	Marwitz & Dawson (1984) cited in Pan & Smith (1999)
Mistral, France	100	-	-	-	Pettre (1982); Jansa (1987); McAneny et al. (1988); Kaufmann & Weber (1996)
Ebro Valley, France/Spain	50	-	-	-	Masson & Bougeault (1996) cited in Pan & Smith (1999)
Taku, Alaska	20	-	-	-	Colman & Dierking (1992) cited in Pan & Smith (1999)
Stampede Pass, Cascades	20	-	-	-	Reed (1981); Colle & Mass (1998) cited in Pan & Smith (1999)
Fraser River, British Columbia	30	-	-	-	Mass et al. (1995) cited in Pan & Smith (1999)
Shikoku Island, Japan	30	-	-	-	Saito (1992) cited in Pan & Smith (1999)
Juan de Fuca, British Columbia	20	140	1000	10/25	Reed (1931); Overland (1984); Colle & Mass (1996); Colle & Mass (2000)
Strait of Gibraltar	20	-	-	-	Scorer (1952) cited in Pan & Smith (1999)
Howe Sound, British Columbia	10	-	-	-	Finnigan et al. (1994); Jackson and Steyn (1994) cited in Pan & Smith (1999)
Kamishak Bay, Alaska	30	-	-	-	Macklin et al. (1990); Fett (1993) cited in Pan & Smith (1999)
Shelikof Strait, Alaska	50	200	1300	15/-	Macklin et al. (1984); Lackmann & Overland (1989) cited in Pan & Smith (1999)
Western Chats, India	30	-	-	-	Ramachandran et al. (1980) cited in Pan and Smith (1999)
Wide Bay, Alaska	80	-	-	-	Bond & Macklin (1992) cited in Pan & Smith (1999)
Unimak, Alaska	15/40	-	-	-	Pan & Smith (1999)
Wipp Valley, Austria	15	50	1400	10/21	Marić & Durran (2009)
Computerized Study	20	50	1400	10/22	Gaberšek & Durran (2004)
Hood Canal, Olympic Mountains	-	-	-	-/50	Overland (1984)
Kareedouw gap, South Africa	1.5	3	300	15/12.5	This study

$$\frac{\bar{v}^2_{entrance}}{2} = \frac{\bar{v}^2_{exit}}{2} + \frac{p_{entrance} - p_{exit}}{\rho}; \qquad \text{Equation 2 . 7}$$

$$\frac{\bar{v}^2_{entrance}}{2} = \frac{\bar{v}^2_{exit}}{2} + c_p(T_{entrance} - T_{exit}); \qquad \text{Equation 2 . 8}$$

Where; p= pressure, ρ= density, c_p *= specific heat for dry air at constant pressure (1004JK^{-1}kg^{-1}) and T = temperature*

A computerized gap flow model found that a gap induced wake penetrated to over 100km downstream (Gaberšek & Durran, 2004). Wakes are defined as areas characterised by a different wind than the environment due to the influence of topography. Colle & Mass (2000) found that the jet wake diverges at the gap exit, at times taking shape as an expansion fan. At the gap exit, the rapid jet wind overhead and the slow environmental wind creates instability in the flow. The instability takes shape of 'wavelike' perturbations (gravity waves) similar to internal waves in water, or Kelvin-Helmholtz waves. Where supercritical Froude values (Equation 2.2) exist at the gap exit, internal waves form. The gap jet diverges and inhibits internal waves from moving upstream; ultimately producing an expansion fan. Colle & Mass (2000) state that as supercritical flow accelerates, becoming rapidly shallower, the flow frequently adjusts with a hydraulic jump as flow becomes subcritical. An expansion fan exhibits characteristics such as divergence, subsidence, and acceleration in the gap exit region (Winant et al., 1988 cited in Colle & Mass, 2000). Colle & Mass (2000) observed an expansion fan feature but attributed it to descending lee air from the lee slope interacting with the diverging gap jet.

The Froude number and the Bernoulli equation (for an incompressible and compressible fluid) were the parameters utilized to evaluate gap flow in this dissertation.

2.1.3 Mountain waves

Mountain waves compliment gap flow in order to reach a maximum gap jet (Gaberšek & Durran, 2004). Mountain waves can take the form of Lenticular cloud (if sufficient moisture available) or remain in clear air; categorized as clear air turbulence (CAT). A mountain wave (Figure 2-3) is an atmospheric gravity wave that takes shape in the lee of a mountain barrier; as statically stable air passes over a mountain. As the air is blocked and forced to rise by the barrier, a cooling in temperature takes place with a compression of air. The region of maximum compression occurs in the area of transition, above the upwind- and lee side of the mountain; the cap cloud region (Figure 2-3). In the cap

cloud region the compressional effect dominates the frictional effect (due to contact with the surface); with the result of stronger winds in the first 100m above the peak (Barry, 1981). As the wind overshoots the peak, the airflow is no longer forced upward by topography and the wave is reflected down due to stronger winds aloft or by the negative buoyancy effect. Flow is only bent down by the negative buoyancy effect if the stability is defined as statically stable (Bradbury, 1992a).

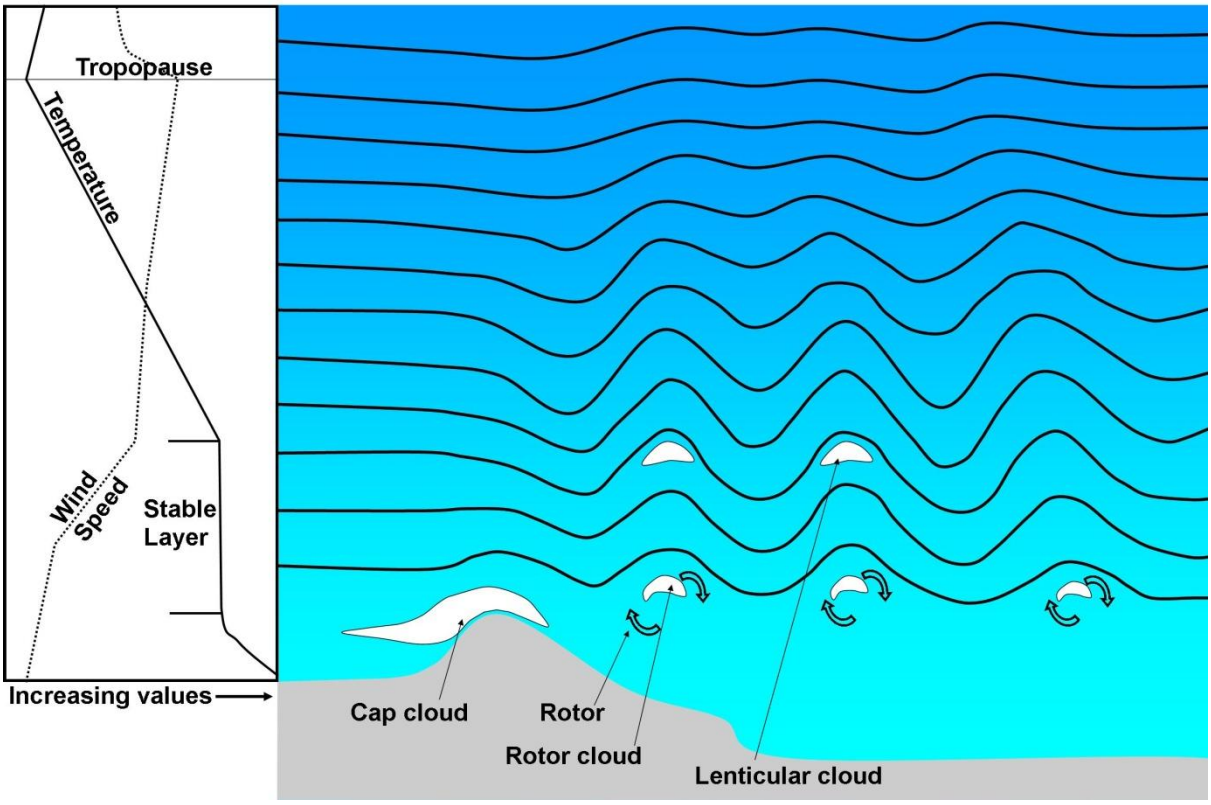

Figure 2-3: Diagram of a mountain wave system with gravity waves on the lee-side. An idealised temperature and wind speed profile are indicated on the left. Adapted from: The COMET Program (2017) and Hertenstein & Kuettner (2005).

The airflow falls with the lee side topography in a downdraft. The air parcel continues to accelerate downwards, overshooting the normal environmental temperature and pressure conditions due to momentum. As this happens, half the mountain wave wavelength is complete. The parcel continues in a downward motion until the buoyancy counteracts the downdraft into an updraft - forming the first wavelength of the wave. Flow does not necessarily need to be deflected upward for mountain wave formation to take place. Cold stable flow over a barrier initiates downslope winds (Figure 2-4) on the lee side correcting with a wave or hydraulic jump (Feltz et al., 2008).

Topography is a pre-requisite for mountain wave development. Ideal topographical features include; a long unbroken ridge with a significant height and a Witch-of-Agnesi shape. Idealised mountains are rare in nature and waves take form over any number of shapes; even isolated peaks initiate waves (Bradbury, 1992b).

Flow across a mountain barrier takes multiple patterns (Figure 2-4) depending on the environmental conditions. Subcritical conditions (Fr<1) are characterized by a stable layer some height above the mountain barrier. In wind flow across the ridge, the stable layer drops very slightly over the barrier; simulating a type of Venturi effect. Under supercritical conditions (F>1) wind flow follows the topography to produce a standing wave. Transitional flow approaches horizontally but then follows the lee ridge; forming a very strong downdraft. Downwind of the lee slope, the first of a series of lee waves form (Bradbury, 1991).

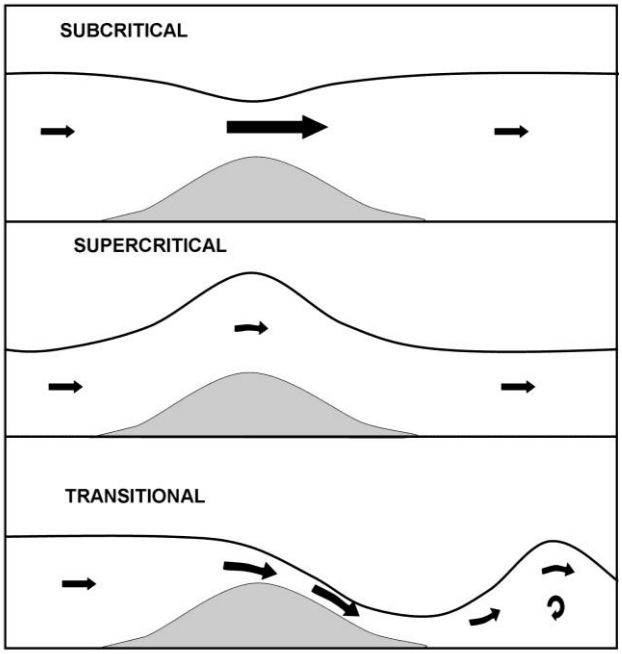

Figure 2-4: Different wind flows over a mountain barrier for subcritical, supercritical and transitional Froude flow. Adapted from: Bradbury, 1991.

Lee waves will remain stationary as long as upwind conditions remain constant, as conditions change a wave can start drifting. Horizontal moving waves can move upwind (when Fr<1) or downwind (Drobinski et al., 2001). Upwind moving waves are slowed by the incoming wind, forming stationary waves (Bradbury, 1992a). Stationary waves (first type mountain wave) on satellite imagery display bars running upwind over the mountain itself with a few bars losing intensity downwind (See Figure 5-9 at 15:15).

Trapped lee waves are the second type of mountain wave. A wave taking shape over a barrier and reflected in phase (by an inversion or strong winds aloft), a resonating system

forms a wave 'train' (Bradbury, 1992a; Caccia et al., 1997). Some studies observed wave trains of up to 300km (Feltz et al., 2008), however, due to leakage of energy, they seldom form more than eight downstream waves (Nance & Durran, 1997). The weaker the stable layer or jet responsible for the reflection, the more energy leaks out of the system; with every following wave a smaller amplitude and shorter wavelength (Bradbury, 1992b). During trapped waves, a single vertical propagating wave is observed over the ridge (Durran, 2013). The third wave type develops if a wave is untrapped and not reflected; forming vertical propagating waves (Bradbury, 1992a).

Synoptic conditions leading to mountain waves are quite variable. The ICAO (International Civil Aviation Organization) noted that a passing cold front frequently triggers mountain waves over north-south orientated mountains (International Civil Aviation Organization, 2005). Then Feltz et al. (2008) observed the disintegration of a trapped wave system during the passing of a cold front. In South Africa, severe mountain waves often occur during northwesterly pre-frontal flow (Van der Mescht, 2012).

According to Reichman (1978), Van der Mescht (2012), Barry (1981) and International Civil Aviation Organization (2005); optimal conditions for the formation of waves are:

- Statically stable airmass in the vicinity of the peak
- Wind speed at ridge crest ≥ 7ms^{-1}
- Wind speed increasing with altitude
- Wind direction perpendicular to the barrier (within 30°)
- Constant wind direction with height

According to ICAO, mountain waves can be forecast but it is "*often very difficult to forecast the actual wind speeds and wind shear*" associated with this (International Civil Aviation Organization, 2005). Forecasting mountain waves, South African aviation weather forecasters simplistically only apply criteria 1 to 4. Not forecasted are the structure and movement of waves, while the severity is left to forecaster interpretation. However, Leeb-du-Toit (2006 cited in Van der Mescht, 2012) estimated the minimum required speed to result in mountain waves in South African conditions to be a minimum of 8ms^{-1}.

The basic structure and movement of mountain waves are dependent on atmospheric variables as well as the size and shape of the mountain barrier. The vertical profiles of the wind direction, speed, moisture, temperature and stability influences the amplitude and wavelength of a wave (Durran, 2013). Atmospheric stability is defined, in almost all studies, to be of utmost importance during mountain wave cases. The more (less)

stable the airmass, the more (less) intense mountain waves are expected. Some sources, such as Bradbury (1992), state: waves can be found even when the air is "*noticeably unstable.*" Where no stable layer is present at the mountaintop, each mountain, ridge or peak produces its own wave with different wavelengths. This produces erratically moving waves (Bradbury, 1991). Optimal stability conditions are low stability conditions that flank a more stable layer in the middle (Leeb-du Toit, 2006 cited in Van der Mescht, 2012).

Except for stability, wind speed is another determining factor for wavelength. A parcel proceeding at a slow (fast) speed over a barrier evolves into a short (long) wavelength wave. Wind direction at mountain peak is also linked to wave propagation. A wave running at an angle to the topography infers a mountaintop wind direction not fully perpendicular to the ridge, but at the same angle (Feltz et al., 2008).

The Froude and Scorer parameters represent all criteria responsible for mountain wave development (topography, stability, wind speed and direction). The Froude number (Equation 2.2) determines whether wave development takes place while the Scorer parameter dictates the vertical extent of the wave (Cronje & Van der Mescht, 2013). The Scorer parameter (Equation 2.9) represents the thermodynamic structure of the atmosphere. The parameter consists of barrier-orientated winds as well as the Brunt-Väisälä frequency and states; the frequency of mountain waves cannot exceed the local Brunt-Väisälä frequency (American Meteorological Society, 2012). The parameter derived from an upwind sounding or model data provides an estimate of the vertical extent of a wave. A uniform or increasing with height Scorer parameter produces a mountain wave that propagates upward and downwind. If the Scorer parameter decreases with height, the wave energy is deflected and trapped lee waves emerge (Caccia et al., 1997).

$$l^2 = \frac{N^2}{\bar{v}^2} - \frac{1}{\bar{v}}\frac{\partial^2 \bar{v}}{\partial z^2}, \qquad \textit{Equation 2 . 9}$$

Where; l = Scorer parameter

For trapped waves to form, the following condition must hold: $l_L^2 - l_U^2 > \frac{\pi^2}{4H^2}$; where l_L and l_U is the Scorer lower and Scorer upper layers, while H is the depth of the lower layer. Where the two layers differ, exceeding the above condition; trapped waves form. Thus, the horizontal wave number (k) will satisfy $l_L < k < l_U$ (where $k = \frac{2\pi}{\text{wavelength}}$) for resonant lee waves to form (Durran, 2013).

In this dissertation parameters utilized to evaluate mountain waves were the Froude and Scorer parameters.

2.2 TURBULENCE

All three the wind flow patterns (blocking, gap flow or mountain waves) in isolation, or in a combination, produce wind shear relating to severe turbulence. Turbulence is defined as; “Random and continuously changing air motions that are superposed on the mean motion of the air” (International Civil Aviation Organization, 2007). A turbulent region is experienced differently in different aircrafts and is contributed to the differing weight, wingspan and the aircraft cruise speed. For example, in mountain waves, the area of maximum energy is maximum lift for a glider plane (Bradbury, 1992a), but an aircraft travelling at a faster speed, penetrating this area, experiences increased turbulence. Blocking and gap flow predominantly produces turbulence caused by areas of increased wind in proximity to slower winds. This may be coupled with major wind direction changes but is easily avoided when not flying low level.

Mountain waves differ in that they produce turbulence throughout the atmosphere and predominantly as a result of vertical motions. The Australian Bureau of Safety recommends that an aircraft needs to adopt a manoeuvring speed as well as keep clearance of at least the height of the barrier in order to keep safe in mountain wave turbulence (Australian Transport Safety Bureau, 2000).

In South Africa, research concerning mountain waves and their associated turbulence has been largely neglected. In 2001, De Villiers & Van Heerden found mountain waves extending up to 7600m amsl over the Drakensberg in 25ms^{-1} wind speeds and low stability conditions. In 2013, Van der Mescht & Eloff defined a methodology in measuring mountain waves in the Hexriver Mountains. Cronje & Van der Mescht (2013) followed this study by investigating limiting conditions in mountain wave rotor formation. Both of the last named studies were conducted during northwesterly pre-frontal conditions. Until the study of Van der Mescht & Geldenhuys (2017), the character and intensity of mountain waves, from non-northwesterly pre-frontal conditions, were largely unknown in South Africa.

The intensity of mountain waves is classified according to three attributes (Table 2-2); wavelength, amplitude and vertical velocity (Grubišić & Lewis, 2004). A greater amount of energy occurs with large amplitude waves (Bradbury, 1992a); which usually entails the first wave downstream of the peak (Suarez & Stauffer, n.d.). The area of maximum vertical velocity is *roughly in the middle of the ridge and trough* (Feltz et al., 2008). The vertical rate of flow creates a severe hazard, especially for aircraft with limited performance (most light aircraft) (CAA, n.d.b). Grubišić & Billings (2007) measured severe mountain waves in the lee

of Sierra Nevada Mountains with a downdraft speed of $10ms^{-1}$. The Sierra Nevada Mountains has an average climb of 3000m over 10km (Grubišić & Billings, 2007). Another case of severe waves, as classified by pilots in the Rockies during a non-linear wave system, exhibited a $4ms^{-1}$ vertical velocity (Feltz et al., 2008). Van der Mescht & Eloff (2013) classified waves severe according to the strength of the wave-induced rotors as well as the updraft and downdrafts (6.1 and $7.2ms^{-1}$ respectively). The Australian Government and the International Civil Aviation Organization classified mountain waves as severe when the downdraft exceeds $3ms^{-1}$ and moderate when values reach between 1.75 – $3ms^{-1}$ (Australian Transport Safety Bureau, 2000; International Civil Aviation Organization, 2007). No internationally used criteria exists for severe mountain waves, but the phenomena pose a significant risk to aviation.

Table 2 - 2: Intensities of Mountain Waves. Adapted from Grubišić & Lewis, 2004.

Intensity of mountain waves	**Strong**	**Moderate**	**Weak**
Wavelength (m)	13-32	8-13	4-8
Altitude variation (m)	1200-2400	600-1200	150-600
Vertical velocities (ms^{-1})	9-18	4.5-9	1.5-4.5

Mountain wave turbulence is induced by vertical shear and is a product of oscillating air currents (Uhlenbrock et al., 2006). The three main sources of turbulence in a mountain wave system includes; breaking waves, interference, and rotors. During these three processes, airflow does not remain laminar but becomes turbulent in nature (American Meteorological Society, 2012; Stiperski & Grubišić, 2010). Breaking waves form when a wave builds up and finally topples over to diminish. Interference takes shape as multiple waves interact to form a combination wave with different characteristics (American Meteorological Society, 2012). A rotor (roll cloud in Figure 2-3) is a circulation of flow below the peak of the wave, around a horizontal axis parallel to the mountain range (American Meteorological Society, 2012). In the experiment conducted, observations (using satellite imagery) of interference waves were limited. Literature suggests that breaking waves occur more frequently in large amplitude waves where waves can tilt upwind and topple over; small amplitude waves remain sinusoidal (Bradbury, 1992a). For the above reasons interference waves and breaking waves were not the focus of this dissertation.

Rotors are a narrow vortex of rotating winds. Rotor vortices, produced by mountain waves, propagate at the speed of its corresponding wave (Suarez & Stauffer, n.d.). The

transient nature of rotor circulations (extreme speed and direction changes) is associated with strong wind shear and poses a significant aviation risk (Reichman, 1978). In the Hexriver Mountains, downdrafts and rotors were the main parameters classifying the severity of mountain waves. Reversed flow, constant potential temperature, vertical wind shear, vorticity and the Richardson number are all used to identify rotors and their associated strength (Van der Mescht & Eloff, 2013). Rotor induced reversed flow is indicated by a constant potential temperature at ridge height. Multiple studies implemented constant potential temperature to indicate areas of constant wind (Overland & Bond, 1995; Van der Mescht, 2012; Feltz et al., 2008). The Richardson number is an indication of whether turbulence exists (American Meteorological Society, 2012). The Terrain-Induced Rotor Experiment (T-REX) classified Richardson values below 0.25 as critical. Critical values demarcate, convective overturning and turbulence are generated (Doyle et al., 2009). Rotors are classified severe where the Richardson number (Equation 2.10) reaches a critical limit (0.25) and where absolute vorticity values are 'higher' (Van der Mescht & Eloff, 2013). Vorticity (Equation 2.11) during mountain wave events are aligned parallel to the ridge. Higher absolute vorticity values indicate stronger rotation in a rotor. In the Southern Hemisphere (opposite to the Northern Hemisphere), positive vorticity values indicate anti-clockwise rotation, while negative values indicate clockwise rotation (Hertenstein & Kuettner, 2005).

$$Ri=\frac{(g/\theta)(\partial\theta/\partial z)}{(\partial u/\partial z)^2+(\partial v/\partial z)^2}; \qquad \text{Equation 2 . 10}$$

$$\eta=\nabla\times U; \qquad \text{Equation 2 . 11}$$

Where; η=Vorticity, ∇=Nabla operator and U=is the total wind in i, j and k directions

"*No hard and fast rules*" are available to determine the severity of turbulence (De Villiers & Van Heerden, 2001). However, multiple rules and parameters exist in order to attempt to predict the severity of turbulence. It is mentioned that the presence of directional shear combined with horizontal shear has a compounding effect on the intensity of turbulence. The South African Weather Bureau[1] implemented the dimensionless Ellrod Turbulence Index (ETI – Equation 2.12) (Ellrod & Knapp, 1992) to aid in forecasting clear air turbulence above ±7000m. The ETI highlights turbulence generated by multiple systems

[1] Now the South African Weather Service

including, mountain waves. De Villiers & Van Heerden (2001) noted that the index does not predict all turbulent cases and the associated severity successfully.

$$ETI = DEF \times VWS$$

$$DEF = \left(DST^2 + DSH^2\right)^{1/2}$$

$$DEF = \left[\left(\frac{\partial u}{\partial x} - \frac{\partial v}{\partial y}\right)^2 + \left(\frac{\partial v}{\partial x} - \frac{\partial u}{\partial y}\right)^2\right]^{1/2}$$

$$ETI = \left[\left(\frac{\partial u}{\partial x} - \frac{\partial v}{\partial y}\right)^2 + \left(\frac{\partial v}{\partial x} - \frac{\partial u}{\partial y}\right)^2\right]^{1/2} \times \frac{\partial u}{\partial z}; \qquad \text{Equation 2 . 12}$$

Where; DEF=deformation, VWS=vertical wind shear, DST=horizontal stretching deformation and DSH=shearing deformation

A reported weakness of turbulence indices is that it does not consider air density. Turbulence is merely a measure of differences in airflow over the aircraft wing and does not consider density. For example, the effect of a $10ms^{-1}$ wind change with height is not the same at 1000m, in dense air, and at 10000m, in less dense air. In less dense air, the net change in airflow over the aircraft wing is less and less turbulence is experienced.

The Richardson number and the Vorticity equations were parameters utilised in this dissertation to highlight turbulence induced by mountain wave rotors. The ETI was tested in this dissertation, in the blocking, gap flow and mountain wave regimes, to determine the usability of the index on the forecasting desk.

2.3 SUMMARY

This chapter discussed the three main wind flow patterns in mountainous terrain, namely; blocking, gap flow and mountain waves. The processes responsible for the formation and the characteristics of the patterns were highlighted. Observations conducted by other studies and the parameters that were found to govern the flow and its characteristics were detailed. This section was concluded with a discussion on turbulence parameters.

CHAPTER 3 : SETTING

In this chapter a brief climatology of the Cape South Coast (where the study site is located) is discussed, followed by an overview of the study site and topographical features. A review of the data follows with the associated weaknesses and strengths of the different data types. This flows into the methodology applied to the data in order to achieve the aims. Experimental design formed part of the aims and is not discussed in the methodology, but is outlined in Chapter 4.

3.1 CLIMATOLOGY

The Cape South Coast is located in the westerlies latitude region and experiences frequent frontal weather. According to Carter (2005), the weather systems influencing South African weather is broadly summarized by a sequence; influencing the country every so often. The sequence lasts roughly six days and starts with the country being dominated by subtropical high pressures. By day three the low-pressure centre of the cold front, located in the westerly belt, approaches South Africa. Day four and the cold front exits the continent with the Atlantic high-pressure system commencing to ridge from west to east. By day five and six the Atlantic high slips eastwards, south of the continent, towards the Indian high-pressure circulation. End of day six, the ridging high pressure merges with the Indian high with no effect on South Africa; returning to day one of the sequence (Preston-Whyte & P.D, 1988 cited in Carter, 2005).

Along the South African coastline, the passing of a cold front is preceded by a coastal low. A coastal low is a shallow system turning winds in passing from offshore directions to onshore southwesterlies. A few hours after the passage of the coastal low the cold front approaches the area. On average, in a 10-year climatology, five coastal lows influence the coastline per month (Carter, 2005), relating to the passage of five cold fronts per month. Taking coastal lows, cold fronts and highs slipping south of the coast into consideration, an approximate westerly and easterly wind direction (zonal wind) are expected.

3.2 STUDY AREA

The study area is known as the Kareedouw Pass (Figure 3-1 & Figure 3-2). The pass (34° 01' 49.37" S and 24° 27' 51.76" E), situated between the Tsitsikamma-Kareedouw ridge (Figure 3-1 and Figure 3-2), is located in the Cape Fold Mountains along the Cape South Coast. The study ridge orientation is 290 - 110° (Figure 3-3) and peak heights vary from 530m to 820m amsl. The upwind and lee surface height varies between 220m to 350m amsl. A few gaps are scattered along the ridge that measures 150 to 350m deep and 1 to 2km wide; when measured at the top of the gap.

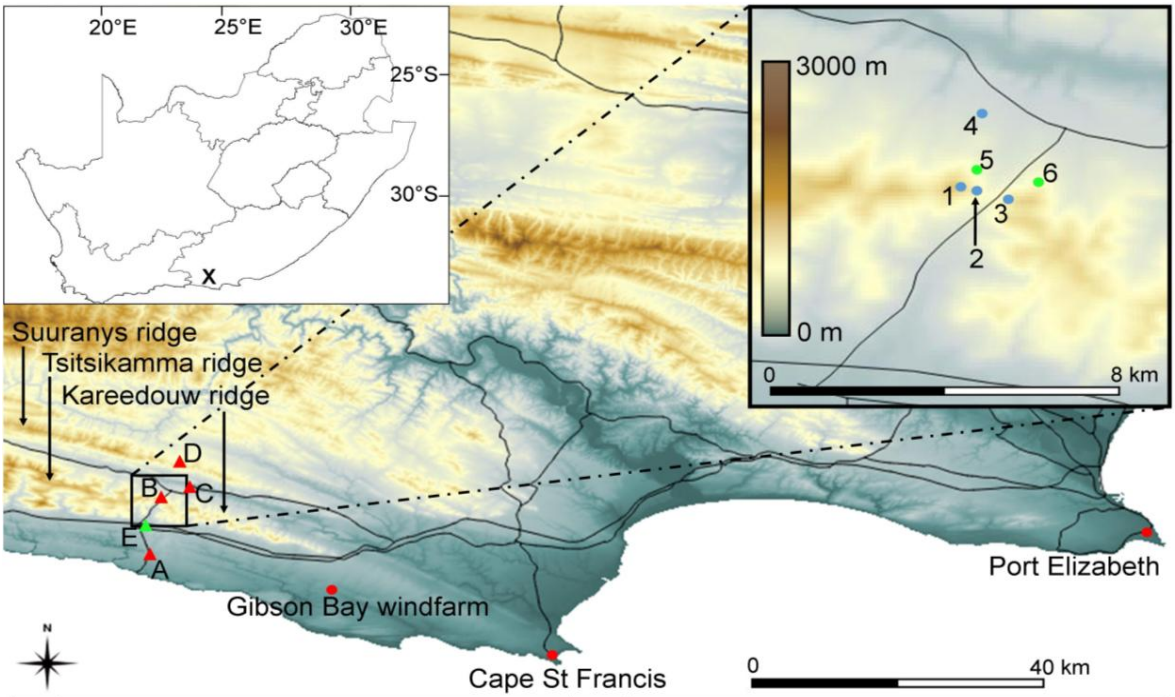

1	Africa Peak AWS (819m amsl)	A	Upwind/Scorer radiosonde
2	St1_baro AWS (540m amsl)	B	Gap radiosonde
3	Camo AWS (520m amsl)	C	Midvalley radiosonde
4	Midvalley AWS (315m amsl)	D	Suuranys radiosonde
5	St1_baro AWS old position (500m amsl)	E	Old upwind/Scorer radiosonde
6	Camo AWS old position (490m amsl)		

Figure 3-1: Topography of the study site and surrounding terrain. Green dots and triangles indicate initial positions which was later moved to new locations. Radiosonde release locations include letters A through to E. The permanent AWS network consists of Gibson Bay windfarm, Cape St Francis, and Port Elizabeth (indicated on larger window), while in the smaller window the semi-permanent stations are named in the table with their respective height above sea level.

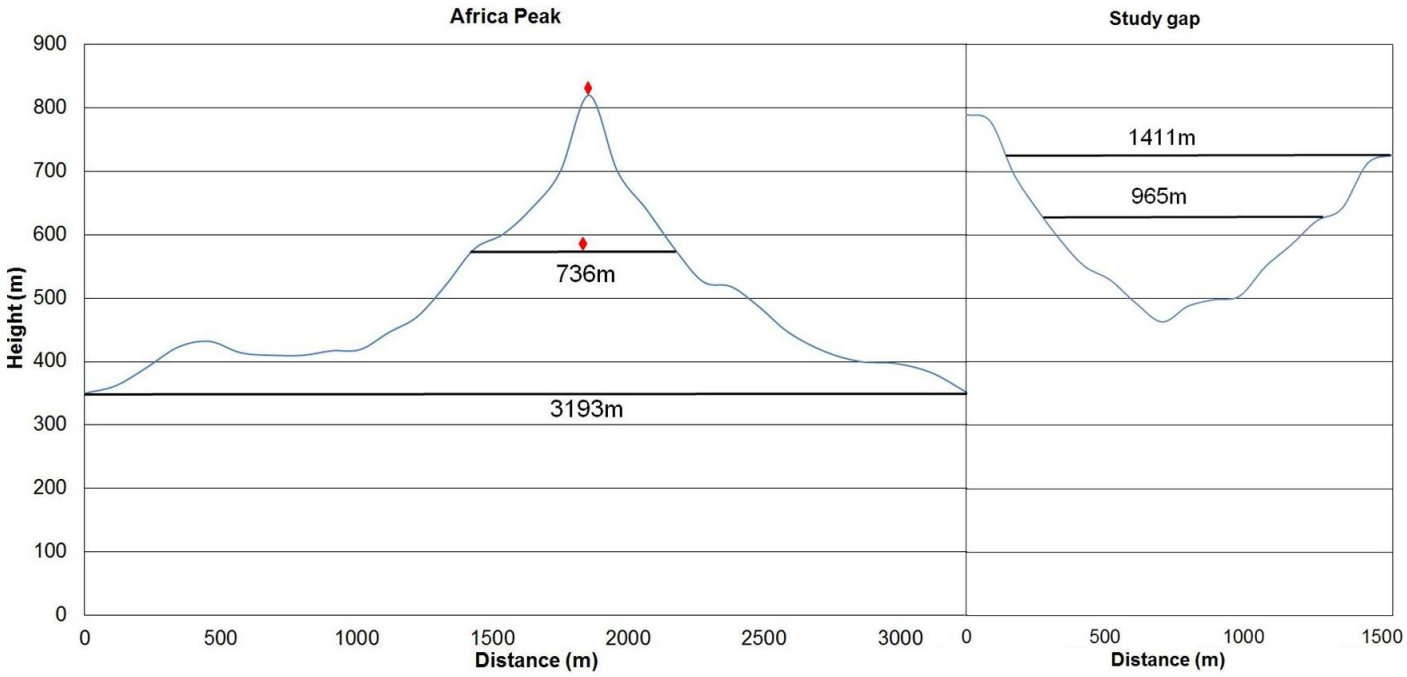

Figure 3-2: Left: Cross-section of Africa Peak (from South to North), forming the western flank of the study gap. The observable mountain height measures 469m. Red diamonds indicate Africa Peak AWS (top – station 1 in Figure 3-1) and St1_baro AWS (bottom – station 2 in Figure 3-1). Lines indicate the foot and the halfwidth of the mountain. Right: Cross-section of the study gap from west to east. Lines indicate the gap width at its widest point and the half gap width.

The study gap is flanked by Africa Peak to the west and an unnamed peak to the east (819m and 744m amsl respectively as in Figure 3-2). The gap height; deepest point of the gap, measured at 460m amsl, making the gap between 280 and 350m deep. All calculations applied the gap depth from 460 to 819m. The gap width of 1400m was determined at the fixed altitude of 744m amsl. The observable mountain height of 469m was applied in all calculations with a mountain halfwidth averaged at 861m. The eastern peak is broader and lower in elevation in comparison to Africa Peak and rises by 394m to the peak with a mountain halfwidth of 986m.

3.3 DATA

Data obtained during this study were on event and longer-term basis. In this dissertation, an event refers to a time period when a field visit with radiosondes was conducted. The duration of all events was classified from the time of the first radiosonde up to the termination of the last radiosonde. Event analysis consists largely of radiosonde data,

while longer-term analysis consists of Automatic Weather Stations (AWSs) data, represented in period by Table 3-1. Details on the AWS and radiosonde sites are provided in Chapter 4 – Experimental design.

Table 3-1: Availability periods of all temporary AWSs. The table is a representation of the periods used in analysis throughout the rest of the study.

Station name	**Availability period (number of days available/total days in field)**	**Comments**
Africa Peak AWS	19/01/2017-13/12/2017 (320/321)	Wind speed regarded as under-estimation throughout the period (discussed in Section 3.3.3).
Camo AWS Old position	10/02/2017-24/05/2017 (103.9/104 days)	Data was evaluated as unfavourable and the station was relocated to obtain better exposure
St1_baro AWS Old position	01/04/2017-11/05/2017 (40/40 days)	
St1_baro AWS new position	25/05/2017-28/02/2018 (279/280 days)	
Camo AWS new position	25/05/2017-28/02/2018 (280/280 days)	
Midvalley AWS	16/11/2017-13/12/2017 & 04/02/2018-28/02/2018 (51/52 days)	
Cape St Francis & Port Elizabeth AWS	19/01/2017-28/02/2018 Cape St Francis – (387.3/406 days) Port Elizabeth – (402.15/406 days)	
Windfarm AWSs	19/01/2017-31/12/2017 (347/347 days)	

3.3.1 Surface data

Surface data comprised of 11 months of continuous 10min AWS data. The AWS network consisted of; four semi-permanent AWSs and three permanent AWSs (Figure 3-1). The permanent AWSs are a fixed structure used by the South African Weather Service and Council for Scientific and Industrial Research (CSIR) on a permanent basis. The semi-permanent stations were erected specifically for this research. The semi-permanent stations included Africa Peak, St1_baro, Camo and Midvalley AWS (numbered 1-4 in Figure 3-1).

The permanent AWSs included; the South African Weather Service owned Cape St Francis and Port Elizabeth AWSs and lastly, the CSIR owned Gibson Bay windfarm AWS. All stations measured wind direction, wind speed and temperature. All permanent stations as well as Africa Peak, St1_baro, and Midvalley AWS also reported pressure.

Data were collected with a variety of sensors and types of AWSs. Africa Peak, Camo, Midvalley, Port Elizabeth and Cape St Francis AWSs consisted of Campbell Scientific loggers, mounted with RM Young wind sensors. Midvalley AWS was mounted with a Davis wind sensor. The St1_baro AWS consisted of a climatological designed MC Systems station; which has a reported weakness for measuring variability on a short timescale. The type of AWS at the windfarm was unknown, but the nature of its application requires calibrated and accurate data. The windfarm comprised of an extensive network and wind measurements were taken at 10m, 20m and 62m. The data owners of the windfarm (CSIR) as well as the Cape St Francis and Port Elizabeth AWS (South African Weather Service), confirmed the data accurate.

All permanent stations passed calibration and wind exposure tests (with exception of the windfarm which was not inspected). All semi-permanent weather stations were fully calibrated and tested before deployment in the field. The instrumentation bias of all sensors were comparable (Table 3-2), which facilitated easy comparison. Availability of AWS data varied due to all stations not being deployed at the same time. Semi-permanent stations were left in the field as long as possible to maximise data span (Table 3-1). To make analysis comparable, a period similar to the semi-permanent stations were applied to all permanent AWS.

Table 3-2: Automatic weather station instrumentation bias and specifications. Source: MC Systems (2010), Campbell Scientific (2018) and RM Young (2018).

Sensor, Brand	**Accuracy**	
Thermometer, Vaisala	±0.6°C	
Thermometer, MC Systems	±0.2°C	
Barometer, RM Young	0.3hPa	
Barometer, MC Systems	0.2hPa	
Wind anemometer, RM Young	Direction: ±3°	Speed: 0.3m.s^{-1} or 1%
Wind anemometer, MC Systems	Direction: ±5°	Speed: 2%
Wind anemometer, Davis	Direction: ±3°	Speed: 1m.s^{-1} or 5%

In this study, the Port Elizabeth AWS was furthest removed from topography and thereby, deemed least influenced by it. As data from this AWS were regarded as least influenced by the topography (and blocking terrain), the data represented environmental conditions. This proved useful; to have a dataset to which data from other AWSs can be compared to.

3.3.2 Upper air data

Upper air data were collected using InterMet Africa 0.2kg radiosondes. Radiosondes transponded temperature, relative humidity, height, latitude and longitude data every 1 second. The program receiving the data (D-Met) calculated the wind direction, speed and pressure. Pilot balloons were inflated with Hydrogen gas (as opposed to Helium), sponsored by Air Liquide. Given the price difference and the environmental impacts in generating helium, hydrogen seemed the sensible choice. All South African Weather Service balloons and all previous South African mountain wave studies utilised Hydrogen; making the study comparable to other studies (Van der Mescht (2012) and Cronje & Van der Mescht (2013)). The balloon was inflated to lift a 0.5kg weight and a radiosonde was attached via a dereeler. The radiosonde data were transponded, at the site, using an InterMet Africa portable receiving station connected to a laptop. Radiosonde biases displayed a good overall accuracy (Table 3-3) and facilitated easy quality control.

Table 3-3: InterMet Africa radiosonde instrumentation bias and specifications. Source: InterMet Africa Systems, 2016.

Sensor	**Range**	**Accuracy**	**Resolution**	**Response time**
Temperature	-95 to +50°C	±0.2°C	<0.01°C	2s @ 1000hPa
Humidity	0 to 100%	5%	0.1%	2s @ 25°C 60s @ -35°C
GPS		10m – horizontal 15m – vertical		1Hz
Wind speed		$1 m.s^{-1}$		1Hz

3.3.3 Data quality control

In all field studies, data need to be intensely quality controlled as human error and faulty equipment influences measurements. Throughout the study, suspicious data were discarded and not used in the analysis. There were two instances where suspicious data

were included in the data set, after some manual manipulation. The radiosondes used in the study did not have a barometer but calculated the pressure values by applying the Hypsometric equation (Equation 3.1). Applying this equation required an accurate initial pressure value. This was unknown at the time of the first event and an approximate pressure value was entered, rendering pressure data unusable. To circumvent this, the pressure of St1_baro were utilised to determine a more accurate initial pressure. Applying this new value, the pressure was manually calculated for all levels by implementing Equation 3.1.

$$h=z_2-z_1=\frac{R\overline{T}}{g}ln\frac{p_1}{p_2}$$

$$p_2=\frac{p_1}{e^{g(z_2-z_1)/RT_v}}; \qquad \textit{Equation 3 . 1}$$

Where; h = height difference, T_v= Virtual Temperature

The second exception concerned the Africa Peak AWS. The anemometer on Africa Peak produced faulty wind speed and direction for an extensive period. Omitting the data would have resulted in too large a gap in the data and the decision made was to correct the data and to use this with caution. The wind direction became faulty due to a screw rattling free and with the direction reference box unsecured, the direction measurement became faulty. The anemometer wire caught on other equipment, settling the reference box on 40°; instead of the required 180°. Photos three months prior to the discovery of the fault, revealed the box in the same position as it was discovered; suggesting it remained stationary for the period. To determine the date the sensor became inaccurate, Port Elizabeth southwesterly winds exceeding 7ms^{-1} were compared to Africa Peak data. All untrusted data were corrected by 140°, after which the two graphs compared reasonably well with one another.

The Africa Peak wind speed sensor was more complicated to correct. The propeller gear protrusions came out of its hollow; abrading them due to friction yielding a reduced wind speed measurement. An attempt to devise a correction formula was launched; with a station erected next to the faulty one. Upon retrieval of the second station, it became evident that the wind blew the secondary anemometer to pieces – rendering measurements unusable. Inspection of the original Africa Peak station, revealed the station out of order and all attempts at fixing the station were abandoned. The Africa Peak direction data were thus used with caution and the speed as an under-representation.

3.4 METHODS

This section describes the methodology applied to all data; to achieve an output to interpret. The bulk of the data analysis was conducted in Excel with some minor parts being conducted with Python and Grads. The program, D-Met, produced the skew-T plots and WRPlot the windroses. Radiosonde flight paths were depicted on Google Earth using HTML coding in WordPad and all topographic analysis were administered using Q-GIS. Satellite imagery was compiled and analysed in SUMO. In analysis, all times mentioned and applied were in South African standard time; GMT +2. All heights mentioned in the study were in amsl, unless otherwise stated.

Data analysis formed two parts: surface data and event analysis. Provided the consistency and continuity of AWS data, it formed the basis of the surface analysis.

3.4.1 Surface data analysis

Windroses, produced from AWS data, provided an overview of wind in complex terrain. To isolate blocking, gap flow and mountain wave cases, another set of windroses were drawn when environmental (Port Elizabeth) winds were southwesterly. To disregard light and variable winds, without losing critical data, the Port Elizabeth required wind speed was set at the pre-requisite speed for mountain waves to develop; $7ms^{-1}$.

Nocturnal, pressure- and temperature-gradient effects were investigated with windroses. The effect of the anticipated nocturnal low-level inversion, on gap flow, was determined by drawing windroses for nocturnal hours (18:00-05:50) and day hours (06:00-17:50). The brief analysis did not take inversion height, strength and synoptic systems into consideration. To reduce the effect of synoptic winds and to isolate the effect of the inversion and gap, the data were normalised with the environmental wind; to produce a normalised windrose. This was done as follows; the Camo wind speed was subtracted by the Port Elizabeth wind speed to produce normalised winds. The normalised winds were offset by $20ms^{-1}$, to ensure no negative wind speeds exist. To produce the true normalised windrose, the windrose legend was adjusted by the $20ms^{-1}$.

The across mountain pressure- and temperature-gradients were determined by subtracting the windfarm AWS from the Midvalley AWS data. The across-barrier gradients were classified and sorted to link to gap wind directions and wind speeds. Temperature classes included; 10<class 1<5°C, 5≤class 2<0°C, 0≤class 3<-5°C and -5≤class 4<-10°C.

The pressure gradient was calculated from the sea level pressure; which was calculated by assuming a column temperature equal to the station pressure. Pressure classes included; -4.5<class 1<-3hPa, -3≤class 2<-2hPa, -2≤class 3<-1hPa and -1≤class 4<+0.5hPa. The different classes were used to draw windroses of the corresponding gap winds (Camo station). The Camo station was used, as opposed to the St1_Baro, given that it provided more favourable wind measurements for comparison. The St1_Baro provided slower wind speeds and also consisted of a different brand sensor to the Camo, Africa Peak, Cape St Francis and the environmental wind (Port Elizabeth) stations – making the data not readily comparable.

In the final surface analysis, wind speed variability was analysed at all RM Young sensors and the windfarm. Wind speed variability not only provides indications of turbulence, but is also of importance to other applications, for example; wind energy, agriculture, etc. Speed variability from the maximum gust and for average winds were determined for all speeds exceeding 7ms^{-1}, by calculating the standard deviation and variance (Equation 3.2 & 3-3).

$$\sigma = \sqrt{\frac{\sum (U_{max} - \bar{U})^2}{n-1}}; \qquad \textit{Equation 3 . 2}$$

$$\sigma^2 = \frac{\sum (U_{max} - \bar{U})^2}{n-1}; \qquad \textit{Equation 3 . 3}$$

The different data types were analysed individually and in combination (e.g. AWS versus radiosonde data). Conclusions made during AWS analysis were tested on the other data types (e.g. radiosonde and satellite data).

3.4.2 Event analysis

Radiosonde data formed the basis of event analysis, but all available data were employed for full analysis. Events were identified and forecast when winds favoured blocking, gap flow and mountain wave formation. Literature suggests that more intense gap jets form (especially at the exit) when mountain waves are present (Gaberšek & Durran, 2004). With this knowledge, emphasis was placed on mountain waves being present throughout all events.

Winds favouring blocking, gap flow and mountain waves include southerly to southwesterly directions; exceeding 7ms^{-1} (see Chapter 2). The southwesterly to southerly directions refer to winds associated with frontal effects impinging on the topography (Figure

3-3), while the speed refers to the mountain wave formation criteria. To simplify the discussion of this study all winds between 180° and 270° were collectively referred to as, southwesterly winds. Environmental southerly winds exceeding 7ms^{-1} were found rare, resulting in all events consisting of flows between 230° and 270° (to avoid discussing results pre-emptively, see discussion on Port Elizabeth windrose of Figure 5-2). Visible waves afforded the opportunity of easy decision making in the field; whether to continue with radiosonde ascents or to terminate the event. Decision making consisted of visualising waves from the ground and by high-resolution visual satellite imagery. Other Eumetsat channels were less helpful in analysis, as the resolution proved inadequate to observe the waves. All events were analysed with a full synoptic analysis from the surface to 500hPa. Mountain waves were the highest propagating turbulence generating mechanism, and data above that were considered of lesser importance.

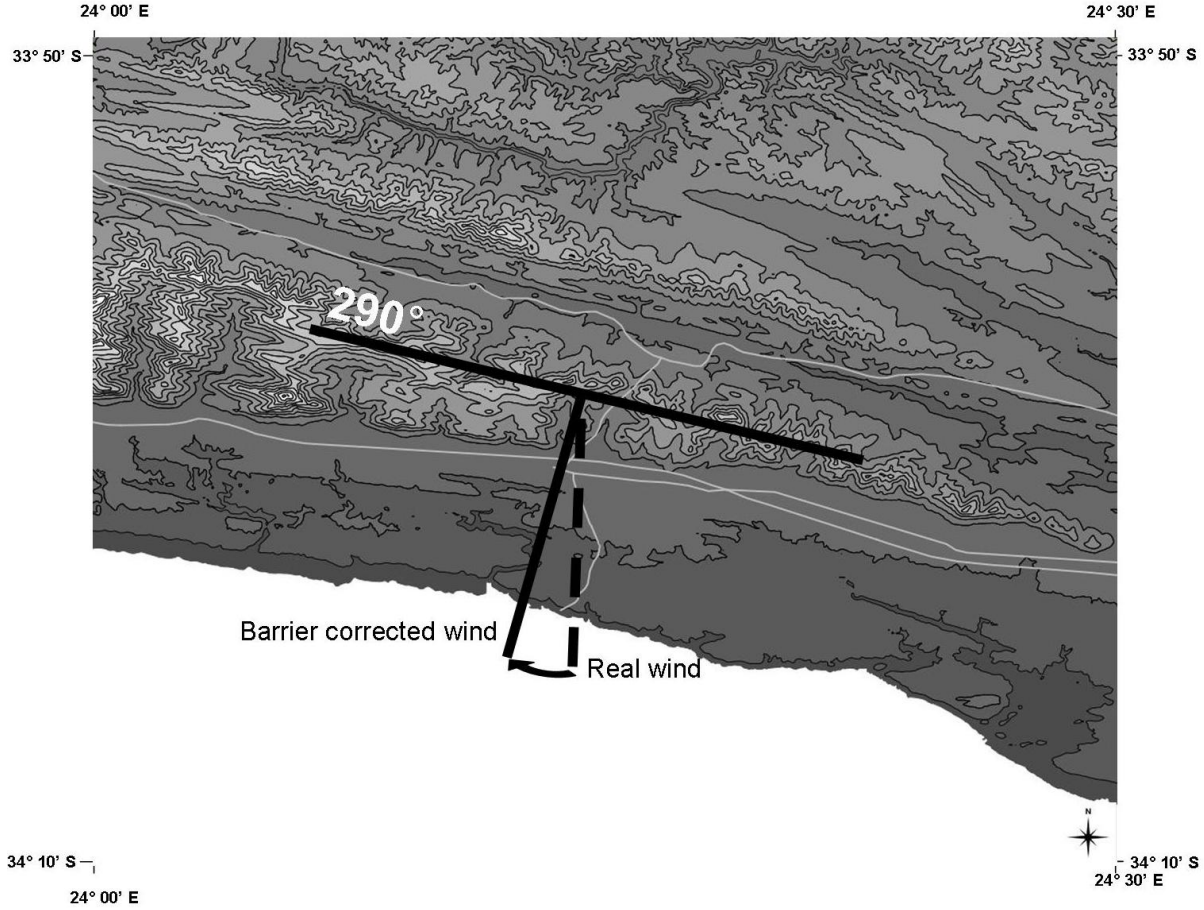

Figure 3-3: Ridge orientation depicting a real v wind component (dashed line) and the barrier perpendicular v̀-wind used for calculating parameters. The ù wind component was calculated similarly.

All parameters dealing with event analysis applied a wind respective to the barrier, rather than total winds. A barrier-orientated wind field was created where along-barrier winds (ù) and cross-barrier winds (ѵ), were represented by; $ù = \frac{u}{\cos 20°}$ and $ѵ = \frac{v}{\cos 20°}$ (as in Figure 3-3). The rotated wind plane facilitated easy blocking, gap flow and mountain wave analysis.

3.4.2.1 Blocking investigation

The upwind radiosonde barrier respective components (ù and ѵ) allowed comparison with other blocking studies. Graphs of the barrier respective winds were compared to Parish (1982) and Neiman et al. (2010). The profiles implemented were to substantiate parameters to indicate whether blocking occurred and to determine the region of maximum blocking.

The first step to identifying and classifying wind flow regimes began with calculating the Froude and Burger parameters (see section 2.1). Both parameters were calculated from the upwind radiosonde; which was released in the blocking affected area. Ideally, the parameters should be calculated from data upwind of this area, however; this was not practical as the blocking region extended to over the ocean. For comparison and calculation purposes, incoming or upwind flow was assumed unchanged throughout the event. The Froude number (Equation 2.2), calculated from the upwind radiosonde, indicated whether blocking (Fr<1) or mountain waves (transitional Fr values) could exist. The Burger number (Equation 2.4) indicated whether flow was quasigeostrophic, semigeostrophic or if the slope acted as a hydrodynamic wall; blocking all flow. Depending on which Froude condition was satisfied, the Rossby radius equation (Equation 2.5) presented the expected jet width while the thermal wind equation (Equation 2.6) the expected speed increase.

The blocking jet width and speed increase was compared with observations of scatterometer satellite imagery; depending on availability at that time. The vertical extent of the blocked flow was determined with the Froude derived height scale and tested on the barrier respective components. Whenever blocked flow occurred above gap height, gap flow formed through air spilling down the gap.

3.4.2.2 Gap flow investigation

Wind flow in the gap was expected during both blocking and mountain wave regimes. Observations from radiosonde and AWS data displayed gap jet strength and its associated directional shear. Radiosonde temperatures and pressures, averaged over the gap depth, were applied to the Bernoulli Equation (Equation 2.7 and 2.8). For this jet strength at the exit projection, the upwind radiosonde was assumed representative of gap entrance conditions and the Gap radiosonde (location B in Figure 3-1) of gap exit conditions. Aside from the

speed and directional changes of the gap jet, downdrafts and a hydraulic jump at gap exit were other turbulence generating features investigated.

Repetitive variations of updraft to downdrafts and velocity disruptions indicate a hydraulic jump (Saito, 1992). Supercritical to subcritical changes in Froude values, calculated from the Gap radiosonde, acted as an indication that a hydraulic jump was possible (Colle & Mass, 2000). Froude changeover values combined with observed divergence (subjectively observed on radiosonde flight paths emanating from the gap), updrafts and downdrafts, were used to determine whether a hydraulic jump or an expansion fan was present. The result was tested on a potential temperature interpolated graph, to infer wind flow.

Potential temperature has been employed by numerous studies to infer and depict wind flow (Overland & Bond, 1995; Van der Mescht, 2012; Feltz et al., 2008). The first step to compile the graph was to plot all radiosonde altitude values versus distance from release point. This produced an ascent profile, which was overlaid with topography, over which the radiosonde drifted. On the ascent line, potential temperature was plotted by hand, at the respective height and distance observed. The final step was to infer the wind flow by hand; by linking all similar potential temperature values. To ease the process, vertical velocities at the respective position provided key insights whether to draw updraft or downdrafts. To distinguish between a true expansion fan and a simulated expansion fan; from downslope mountain wave induced lee winds, Africa Peak AWS potential temperature was added to the plot. If the radiosonde observed, below peak height, potential temperature values similar to the peak, a downdraft down the lee slope was indicated.

3.4.2.3 Mountain wave investigation

Mountain wave detection in radiosonde data encompassed a close inspection of radiosonde ascent rate. Frequently the wave was not strong enough to induce the radiosonde to lose height, and in these cases, a reduced ascent rate was used to infer a mountain wave top. The mountain wave top and the type of mountain wave were identified using the Scorer parameter and its associated wavenumber criteria. To reduce noise in the Scorer graphs, the parameter (Equation 2.9) was calculated every 250m and averaged over 500m. The Brunt-Väisälä frequency was calculated for every data point, but similarly averaged over 500m to produce stability graphs. To determine wave characteristics, satellite imagery and lee radiosondes were analysed in conjunction with the Scorer parameter.

Wavelength, amplitude, updraft and downdraft speed were all features providing insight into the severity of waves. Wavelength was measured on satellite imagery,

cumulative normalised ascent graphs or inferred from potential temperature plots. A radiosonde penetrating the wave, provides insight into the amplitude of the mountain wave. Lastly, vertical velocities were observed on radiosonde data to compare mountain wave severity to the literature.

Arguably, the most severe feature of mountain waves are rotors. Rotors were observed in raw radiosonde data or in calculated vorticity, potential temperature and Richardson values. Vorticity was calculated for all lee side ascents to determine areas of rotation perpendicular to the barrier – highlighting rotors. Vorticity perpendicular to the mountain ridge was derived from Equation 2.11 and yielded; $(\partial w/\partial y)-(\partial \dot{v}/\partial z)$. Possible rotors were inspected for constant values potential temperature values and increased updraft and downdrafts in vicinity of ridge height. The highlighted rotors were examined for critical Richardson values (Equation 2.10); to determine severe rotors and thus severe turbulence.

3.4.3 Turbulence in general

All radiosonde ascents were inspected with turbulence indicating parameters, namely; Richardson number, ETI, vorticity, updraft/downdrafts as well as wind direction and speed changes. All parameters, except vertical velocity, facilitated easy interpretation on graphs by highlighting extreme values. Turbulent areas produced such variations in vertical velocity, that noise in the data made interpretation difficult.

The normalised ascent rate, provided the radiosonde updraft and downdraft speed; i.e. the vertical velocity. The normalised ascent rate was calculated by the average balloon ascent rate subtracted from the actual ascent rate. The collective ascent rates throughout the ascent produced the average ascent rate (Van der Mesht & Eloff, 2013; Grubišić & Billings, 2007). Theoretically, the normalised ascent rate is zero until an updraft; a positive answer, or a downdraft; a negative answer is encountered. Different to Van der Mesht & Eloff (2013) as well as Grubišić & Billings (2007), visualising the normalised ascent rate was a problem as noise in turbulent regions made readings difficult to interpret (600 to 800m in Figure 3-4 left). A solution was provided by the cumulative normalised ascent rate. Adding the normalised ascent rates did not only provide a visually more pleasing display, but highlighted all the updrafts, downdrafts as well as the turbulent disruption of laminar flow (disruption of a smooth graph between 600 and 800m).

On the normalised ascent rate graph, negative values depict a downdraft. On the cumulative normalised ascent rate, all leftward slants indicate downdrafts and all rightward slants indicate updrafts. The steeper the slant of the graph the more intense vertical velocities were measured. A long steady slant was indicative of a near-normal ascent rate, or a long, steady and smooth updraft. The physical values of the cumulative normalised ascent rate were of little interest. Plotting multiple parameters (for example barrier corrected winds, Froude and potential temperature) when no quantative vertical velocity values were required, made the cumulative normalised ascent rate an easy graph to correlate with.

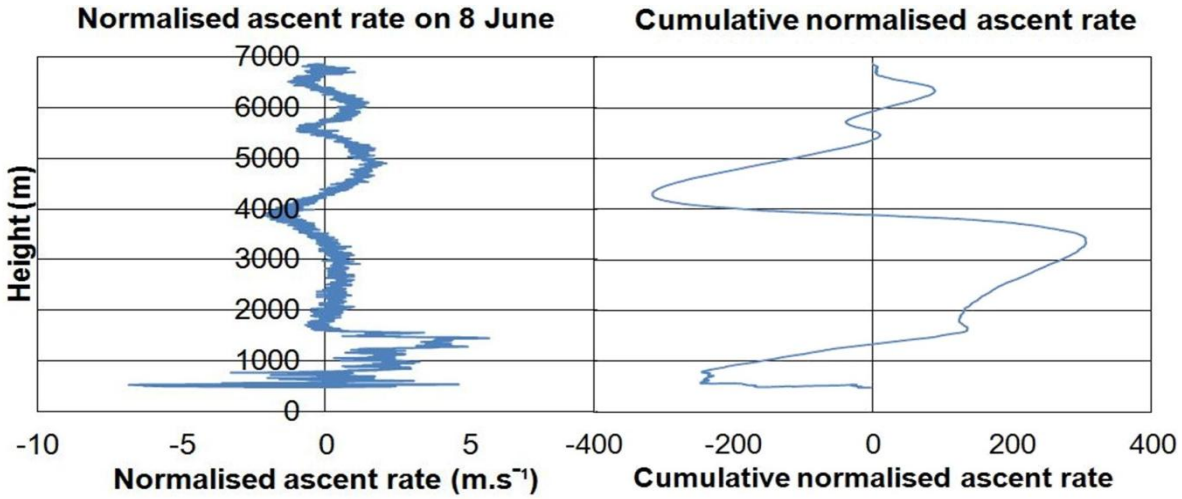

Figure 3-4: Normalised ascent rate (left) versus cumulative normalised ascent rate (right) in order to reduce noise in the data.

Another variant of the cumulative normalised ascent rate graph was obtained where cumulative normalised ascent rates were plotted versus distance; this made a useful overlay on radiosonde altitude versus distance graphs (for example, dash-dot line Figure 5-14). In the bottom inset within this figure, the downward sloping dash-dot line indicates a downdraft and is in good correlation to where the radiosonde altitude flattens; indicating a reduced ascent rate caused by a downdraft.

All areas highlighted as turbulent, were analysed in order to determine the intensity and possibly the origin thereof. All turbulence-indicating observations were compared to other studies to correlate severity of the features in this environment. Lastly, a theoretical case was prepared, using longer-term and event data; to simulate what an aircraft would experience during such cases.

3.5 SUMMARY

This chapter started with the discussion of the importance of small-scale topographical features. Different types of data and how they were measured were then detailed, followed by the methodology used to analyse and interpret the data, in order to quantify blocking, gap flow and mountain waves. This chapter should be going hand-in-hand with Chapter 4, which should not be viewed in isolation.

CHAPTER 4: EXPERIMENT DESIGN

The study's first aim was to design an experiment to measure blocking, gap flow and mountain wave interaction. In this chapter, a detailed account is provided of the rationale, successes and failures contributing to the design of the experiment. This is followed by a brief discussion on experiments not conducted as part of this dissertation, but which have potential for future studies. Provided that the experiment was adapted in time as certain results were obtained and realised, some pre-liminary results may appear in this section. However, excluding these pre-liminary results from this section, would result in the reader not understanding the rationale.

Funding often severely limits field studies. In these cases, exceptional planning is required to allow for optimal results with limited equipment and supplies. Lack of funding limited this study to conventional equipment, namely; AWSs and radiosondes. To design a successful experiment, it is required to understand the strengths and weaknesses of the available equipment.

A weakness of AWSs is that it is a surface measurement and no vertical measurement is taken. The vertical structure of the atmosphere is obtained from radiosondes, which are more economically viable replacements for SODAR, LIDAR and RADAR. A weakness of radiosondes is that only a once-off point measurement is made at the respective height, making it difficult to track phenomena. Depending on the complexity of the experiment, careful consideration of surface and upper air measurements are required. In this dissertation, surface station data are used to investigate features over a longer time-scale, and predominantly applied in the gap flow analysis. Radiosondes were released on an event basis and the data obtained predominantly used in the mountain wave and blocking analysis.

4.1 AWS NETWORK DESIGN

The design of the automatic weather station network was preceded by in-depth topographic chart analysis and multiple site visits. The ideal placement of the AWSs was decided on after considering the literature of field experiments, experts on field studies, topographical features and meteorological footprints (Figure 4-1). Factors hampering the placement of the instruments, included; permission from landowners, accessibility as well as financial and security considerations. To maximise data coverage, an existing permanent

AWS network (from the South African Weather Service and CSIR) was used to supplement data (Figure 3-1).

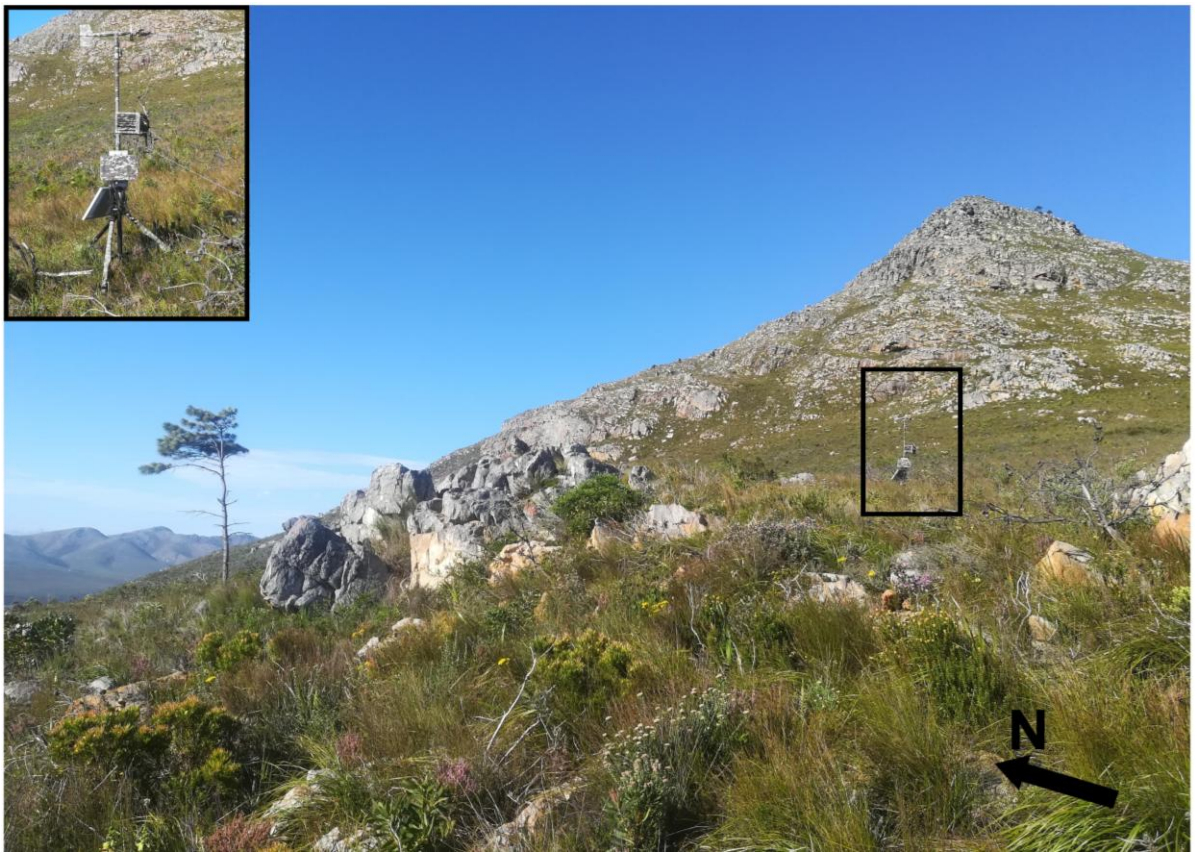

Figure 4-1: Meteorological footprints which indicate wind flow funnelling through the gap. Note how all the branches point from South to North (North arrow in the bottom right corner). This made a sensible location for gap flow measurements and Camo station (station 3 in Figure 4-2) is observed in the block and the inset.

To study gap flow, incident measurements at the entrance, measurements in the gap and at the exit of the gap were required. Upwind AWS sites were important to determine gap-incident conditions. The permanent network in the area included three upwind and no downwind AWSs. As three permanent AWSs included (Figure 3-1 – repeated below as Figure 4-2, due to the large number of referrals in this chapter); Cape St Francis, Port Elizabeth and the windfarm a good upwind network existed and attention was therefore turned to the ridge itself. One AWS on the ridge were to provide insight into mountain waves and data for comparison with gap data. The AWS was placed on Africa Peak (1 in Figure 3-1 & 4-2), the highest peak flanking the gap.

The placement of AWSs to measure gap flow on the lee side had to be decided on. Initially, the gap jet was to be measured by radiosondes and focus was placed on measuring

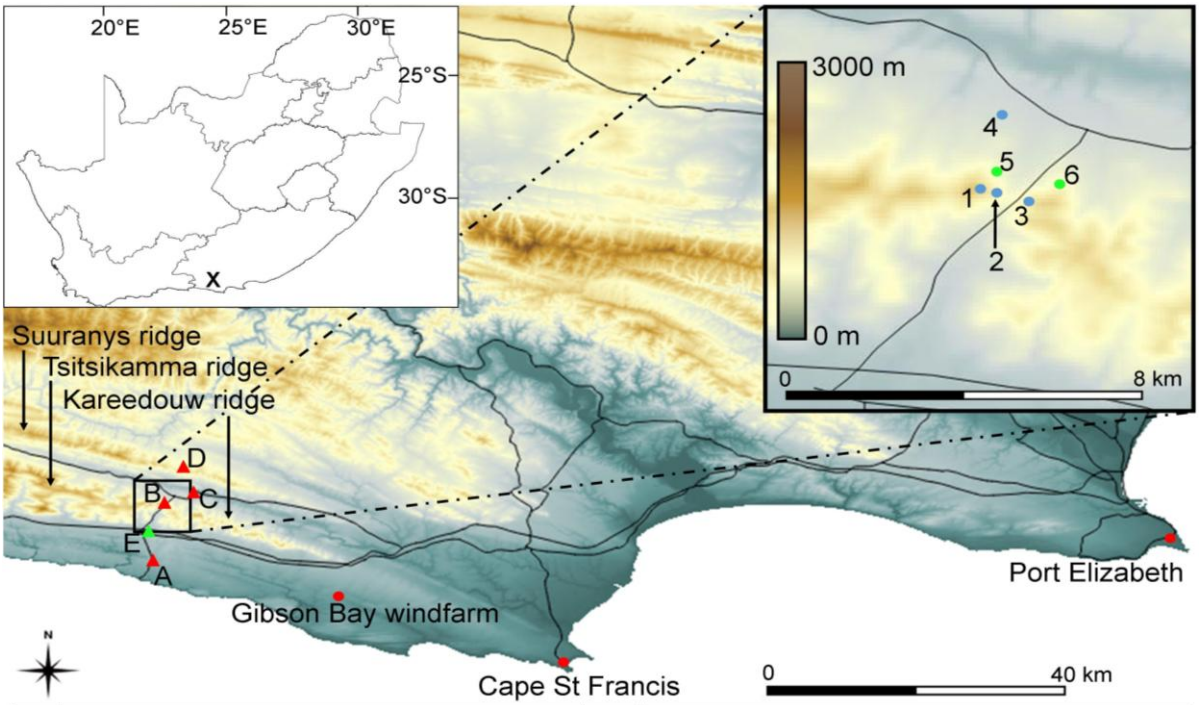

1	Africa Peak AWS (819m amsl)	A	Upwind/Scorer radiosonde
2	St1_baro AWS (540m amsl)	B	Gap radiosonde
3	Camo AWS (520m amsl)	C	Midvalley radiosonde
4	Midvalley AWS (315m amsl)	D	Suuranys radiosonde
5	St1_baro AWS old position (500m amsl)	E	Old upwind/Scorer radiosonde
6	Camo AWS old position (490m amsl)		

Figure 4-2: *Topography of the study site and surrounding terrain. Green dots and triangles indicate initial positions which were later moved to new locations. Radiosonde release locations include letters A through to E. The permanent AWS network consists of Gibson Bay windfarm, Cape St Francis, and Port Elizabeth (indicated on larger window); while in the smaller window the semi-permanent stations are named in the table.*

Figure 4-3: Africa Peak weather station (1 in Figure 4-2). Photo is taken toward the west with the lee slope visible to the right of the photo.

the gap outflow. The initial plan was later altered to place the AWSs in the gap itself, rather than in the outflow. Initially the AWSs were placed in the gap exit in order to measure divergence of flow in the exit region. The two AWSs (St1_baro old and Camo old – 5 and 6 in Figure 4-2) were erected downwind of the exit region; on the right and left flank of the gap. Unfavourable results of the wind measured by the AWSs resulted in the moving of the stations a month after deployment. Initial measurements combined with site visits suggested below average wind speeds and the possibility that eddies was measured rather than gap flow divergence. The left flank direction sensor, spinning in all directions, was seemingly indicating a probable eddy (which was a good find but produced below average wind speeds). The initial plan to measure gap divergence was therefore abandoned and the two AWSs moved to the gap, where the wind in the centre of the gap was measured (St1_baro and Camo – 2 and 3 in Figure 4-2). The AWSs were placed an equal distance from the gap centreline and at similar heights; approximately the bottom third of the mountain. This allowed insight into the right versus left flank of the gap jet. There were consequently two additional stations in the gap itself.

On the lee side of the gap, measurements came from the Midvalley AWS (4 in Figure 4-2). Theory suggests pressure and temperature gradients form an important part to explain gap flow and are a pre-requisite for calculations (Gaberšek & Durran, 2004). The Midvalley AWS was used as the lee observation, while the windfarm provided measurements of the upwind regime. Gradients from these two stations provided the opportunity to explain the pre-existing gap conditions. The Midvalley AWS was positioned far from the gap and uninfluenced by the gap flow.

4.2 UPPER AIR OBSERVATION DESIGN

In determining the location of upper air measurements, it was essential that they complement the measurements done by the AWSs. The launching of radiosondes required accessibility by road as the gas canister, used to inflate the balloons, needed to be transported safely. Another factor to consider was the reception quality of the equipment. Reduced reception was attributed to topographical features blocking line-of-sight to the antenna. There were only a limited number of radiosondes available in this project and it was therefore essential to optimize their use during every field experiment. There were two main considerations in the design of the upper air experinement: geographical location and ascent

rate. Decisions also had to be taken on the days of the experiement, determined by how the weather system evolved and what was observed.

4.2.1 Geographical location

A mountain wave study usually consists of one upwind Scorer radiosonde and some lee radiosondes (Van der Mescht, 2012). The upwind radiosonde, determines the incident conditions and the lee radiosondes measure the wave features. In this experiment the upwind radiosonde was used for determining upwind conditions and for measuring blocking. The upwind location was initially selected for easy accessibility (E in Figure 4-2; 5km from the ridge). However, during the first field event, the upwind radiosonde rapidly passed over the ridge rendering it unrepresentative. It was therefore decided to adjust the release location an additional 4km upwind (A in Figure 4-2). There were also three lee radiosondes released per event.

In order to identify the location of the lee radiosondes, smaller experiments were conducted first. Ten preliminary lee radiosonde locations were identified, based on where literature suggested prominent wave features would be located (Feltz et al., 2008; Van der Mescht, 2012 and Durran, 2013). On days when turbulence was likely, hydrogen filled party balloons were released at the 10 locations and visually observed for signs of turbulence. Several observers with binoculars followed the assent of the balloons and locations with the most updrafts, downdrafts and balloon shaking were noted. Three radiosonde release sites were consequently identified and indicated as Gap (B), Midvalley (C) and Suuranys (D) in Figure 4-2.The Gap radiosonde (B in Figure 4-2) were used to measure gap flow and to test if mountain waves existed over the valley. The party-balloon experiment indicated significant downdrafts at the gap exit – confirming this release location was of importance. The Midvalley release location (C in Figure 4-2) was selected between the Kareedouw and Suuranys ridge. Close to 50% of the party balloons released from this location shook heavily in ascent, indicating turbulance. This location also provided the opportunity to measure flow down the Langkloof valley – which according to the local residents was significant. More importantly, the radiosonde was expected to drift through the valley rotor or downstream and be able to measure the primary mountain wave over the Suuranys ridge (Figure 4-4). The rate of ascent of the balloon released from this location would indicate the presence of a mountain wave or rotor.

The last release location was situated on top of the Suuranys ridge (D in Figure 4-2). The party-balloon experiment demarcated a significant downdraft followed by vigorous

turbulence in its ascent. Apart from the turbulence, this location could also possibly identify downstream mountain waves.

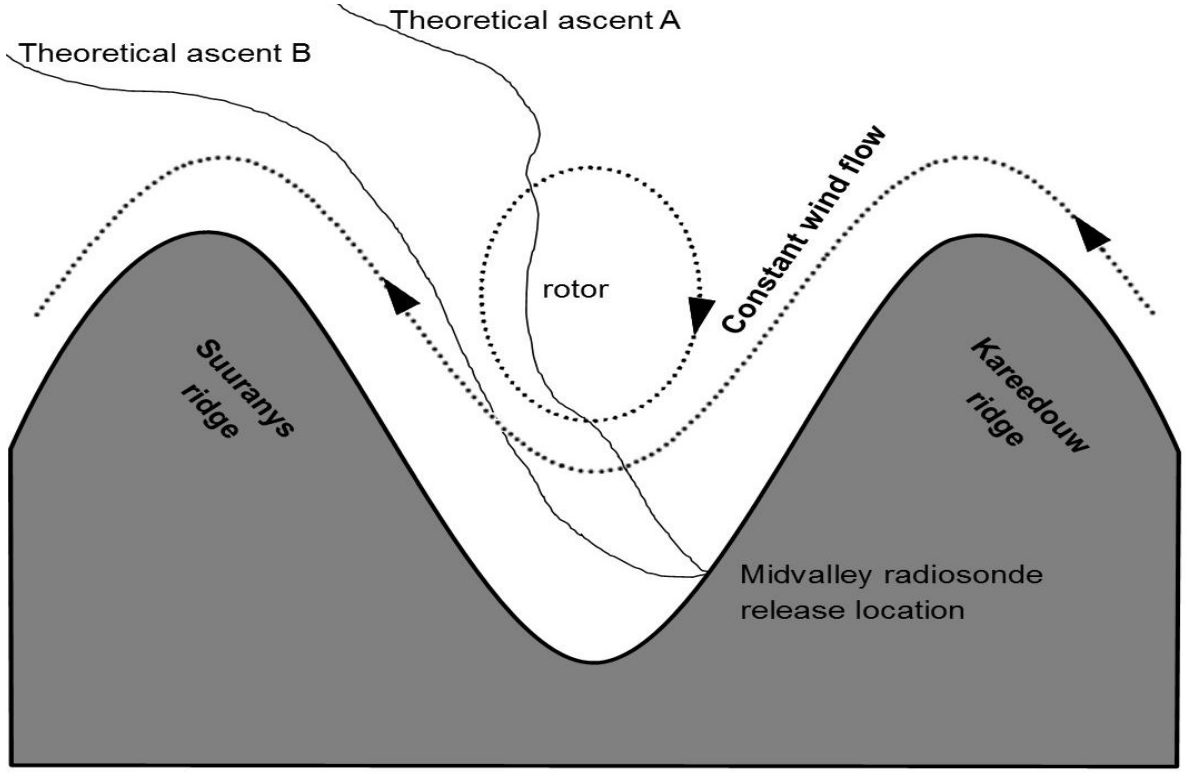

Figure 4-4: Anticipated theoretical isolines (dotted line) in the valley, explaining the rationality of the Midvalley release location (C in Figure 4-2). The thin lines depict two theoretical radiosonde ascents; ascent A – faster ascent rate, penetrating the theoretical valley rotor and ascent B – slower ascent rate, following winds in an updraft forced by the Suuranys ridge.

4.2.2 Ascent rate

In order to keep data comparable, it is important that the balloon has a constant ascent rate. A rapid ascending balloon provides fewer data points and passes an area of interest too rapidly. A slow ascent rate results in the balloon drifting too far downwind, ascending slowly, and thereby taking too long to reach the desired height. However, a radiosonde ascending slowly spends more time in the updraft and more easily follow it into a downdraft or rotor. In this experiment, one slow ascending balloon was used at the gap exit, in order to measure the downdraft and possibly the transition into a hydraulic jump correction or an expansion fan. With exception of this one balloon, it was decided to use a constant ascent rate of $3ms^{-1}$. This was achieved by selecting a weight the balloon had to lift upon

inflation. All balloons throughout the study lifted the same 0.5kg weight, keeping the ascent rate relatively constant. It was endeavoured to release four balloons per event (estimated to last approximately 6hrs). Considering travelling and set-up time, this allowed 1.5hrs per ascent. Ascents needed to be rapid enough to reach the required altitude (evaluated to be between 5 and 6km agl) and slow enough to provide quality data. Opting for a 0.5kg weight, the study was also made comparable to other South African studies.

4.2.3 Decision taking on the event day

On event days, decisions regarding the release of radiosondes and release times were based on multiple factors. Before every event, the forecast was scrutinized using South African Weather Service operational NWP products. Wind direction, wind speed and stability parameters (Section 2.1.3), formed the basis of the forecasting. The main factors which were considered were wind speed exceeding $7ms^{-1}$, wind speed increasing with height and a constant wind direction with height. The forecasts were based amongst others to expecting the direction to be 40-50° from perpendicular. There were times that the NWP wind speed forecast was less than $7ms^{-1}$ but mountain waves were nevertheless observed. For pre-frontal events, the timing, position and angle of the front, in relation to the coast were considered. In this study a frontal tail, almost parallel to the coast, generally produced mountain waves – even when model winds and stability were indicating that conditions were unfavourable. This is significant as the mountain barrier stretch from west to east and cold frontal winds (west to south westerly) are more parallel to the barrier; than what it is perpendicular.

A nowcasting approach was adopted while in the field. Nowcasting relied on observations obtained from the earlier assents done on the day, observing clouds from the ground and analysing real time high-resolution visual satellite imagery. Satellite images played an important role as they were assessed before all radiosonde releases. Mountain waves and their evolution over the study site and to the west were considered. Mountain waves to the west indicated that favourable conditions were still approaching. Where no waves existed to the west and waves in the study site altered from stationary to moving or a drop in amplitude occurred, the next ascent was put on hold. Compared to blocking and gap flow, mountain waves were shortest lived and on average lasted 3-5 hours. At times, this timeframe proved too short to complete data collection and the event experiment was ended pre-maturely.

4.3 OTHER EXPERIMENTS

This section will detail other experiments and equipment that could be used in a field experiment, to identify the turbulent features. Some of these were tested for inclusion in this dissertation but was found to be unfeasible. They are included here in order to provide guidance to future experiments of this nature. Experimentation with tethersondes, parasail's, simultaneous ascents, dropsondes, smoke bombs and dronesondes are discussed.

4.3.1 Tethersondes

A tethersonde is a radiosonde attached to a balloon which is fixed to the earth surface by means of a line. Tethersondes failed miserably as the balloon ascended only to descend again downwind. The experiment consisted of fishing line, 1km in length, attached to a balloon; which ascended downwind as the line unwound. After the fishing line finished unwinding, the balloon slowly descended to the surface. In experimentation, the balloon slowly descended up to the same height as the fixed point on the earth surface. The origin of the problem was the horizontal force (force of the wind – Figure 4-5) being stronger than the resultant upward force. The fixed line causes the balloon to move within a semi-circle, of which the radius was determined by the line. The upward buoyancy force initiated by the gas (50.3 Newton (Nw)) neutralise the force of gravity (6.6Nw – gravity acting on the radiosonde, balloon and gas combined) and produces a resultant upward force of 43.7Nw. The 48.1Nw force exerted by a wind speed of $5ms^{-1}$ override the resultant upward force. In order for the balloon to drift in a horizontal direction with the wind, it must follow the semi-circle in a downward direction. Tethersondes will only be useful if the resultant upward force is stronger than the horizontal force enacted by the wind.

To calculate the required wind strength for a balloon to ascend, the horizontal and vertical forces can be calculated. The horizontal force (force of wind – F_w) is calculated by Equation 4.1 and the vertical resultant force by Equation 4.2. These equations assume a constant balloon radius (1m), cross-sectional area ($3.14m^2$) and volume ($4.19m^3$). The mass of the radiosonde and balloon amounted to; 0.2 and 0.1kg respectively. In order to simplify the equation, the weight of the fishing line was not considered. By substituting the resultant vertical force into the horizontal force equation, the required wind speed to balance the system is calculated. The wind speed of $4.8ms^{-1}$ balances the forces, with the line at a 45°

angle to the surface. A stronger wind will affect the balloon to slowly descend, while a weaker wind cause it to slowly ascend; all in a semi-circle.

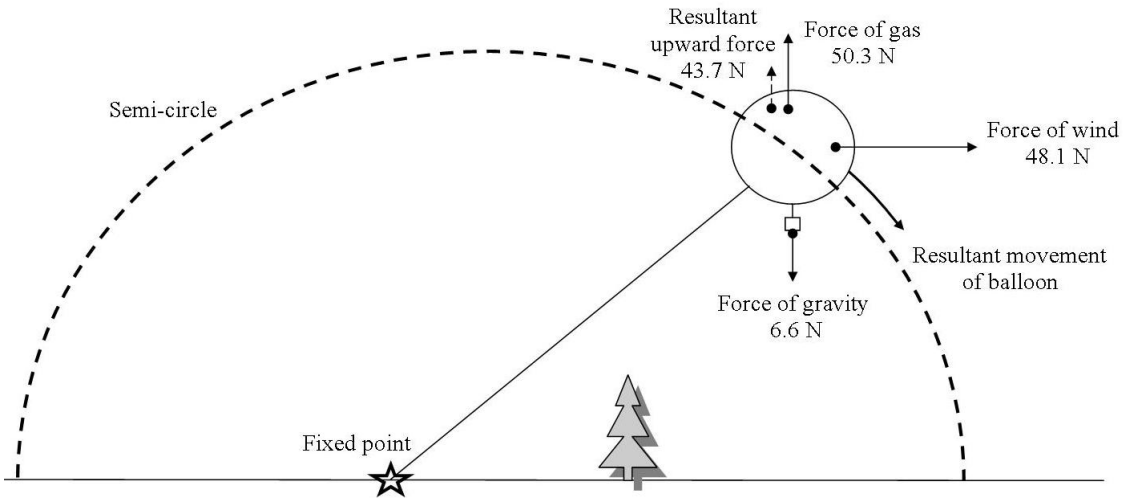

Figure 4-5: Forces acting on the balloon in the tethersonde experiment. Forces are not drawn to scale.

$$F_w = PA$$

$$= \frac{1}{2}\rho_{air} V^2 A; \qquad \text{Equation 4 . 1}$$

Where; A = cross-sectional area and ρ_{air}= density of air at 1.225kgm^{-3}

$$\text{Resultant vertical Force} = F_{up} - F_{down}$$

$$= F_{gas} - F_{gravity}$$

$$= (\rho_{air} gVol) - (F_{\text{gravity on radiosonde and balloon}} + F_{\text{gravity on gas}})$$

$$= (\rho_{air} gVol) - (m_{radiosonde+balloon} g + \rho_{gas} gVol) ; \qquad \text{Equation 4 . 2}$$

Where; Vol= Volume, $\rho_{hydrogen}$= 0.0899 and ρ_{helium}= 0.179 kgm^{-3}

In strong winds, tethersondes are a good way of recycling a radiosonde – if sufficient patience is employed to untangle and retrieve 1km of fishing line. It could be expected that the temperature, pressure and height measured by the tethersonde, would have been accurate but the wind direction and speed would have been unusable.

4.3.2 Parasails

A parasail is a specialised parachute, pulled along by a moving vehicle to keep it in the air. Parasail's exhibited some potential after brief testing. In this study, it was logistically

pointless to spend time and resources on a car driving up and down in order to keep the parasail in the air.

4.3.3 Simultaneous ascents/different buoyancy balloons

It was considered to deploy balloons simultaneous from different locations or to deploy balloons with differing buoyancies from the same location. Two balloons, from the same location with differing buoyancies will ascent differently (similar to the two ascents in Figure 4-4). Such an experiment would have yielded a 3-Dimensional look at a narrow band in the atmosphere. Software problems and limited number of radiosondes inhibited further experimentation.

4.3.4 Dropsondes

A dropsonde is a radiosonde attached to a parachute, dropped by an aircraft or from a mountain. Dropsondes are commercially available but the budget for this research did not allow for their use and low cost options were explored. These were initially considered feasible in this experiment but were eventually not used. It was found that the force of the wind was greater than the downward force resulting in the parachute being pushed closed by the wind and the equipment dropping to the surface. Three possible solutions were considered; only use dropsondes when wind speeds were lower, to make the descent of the parachute swifter or to keep the parachute open by stilts.

To obtain sensible wind data from a dropsonde, it is necessary for the downward and horizontal motion to simulate that of an ascending balloon – but downwards. To achieve this, the cross-sectional area of the parachute needs to correlate to that of a balloon at similar heights – only then would the wind force on both be the same (Equation 4.1). However, if a downdraft or strong gust occurs, the parachute will most likely close with the equipment dropping to the ground.

As part of the research for this dissertation an experiment was conducted by ejecting a parachute from an ascending balloon. The mechanism contained a balloon attached to a sparkler (a 15cm long sparkling stick when set alight) with a thin rope, followed by the parachute and finally the radiosonde (Figure 4-6). The sparkler was timed to burn the rope 90s into the flight, ejecting the parachute. Once ejected, the falling parachute should deploy, drifting to the surface. During the dropsonde experiment the radiosonde signal was lost and

the balloon drifted out of sight before ejection took place. It was concluded that the sparkler was defective and the rope did not burn.

Future experiments with these low cost dropsondes should replace the sparkler with dependable mechanical equipment. Turbulence could result in an explosion as the sparkler connects the highly flammable hydrogen-filled balloon.

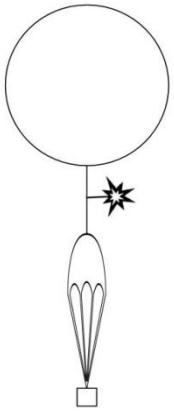

Figure 4-6: Dropsonde still attached to the balloon. As long as the balloon is in an upward direction the parachute is expected to remain closed.

4.3.5 Smoke grenades

Smoke could be a valuable tool for visualising the wind flow, its associated vorticity and turbulence. Research as early as 1969, introduced smoke to visualize wake vortices caused by, take-off and landing aircraft (Federal Aviation Administration, n.d). In this project, smoke grenades and homemade smoke bombs were used to produce smoke.

Smoke was generated at the gap exit, on the surface and from the bottom of a balloon. The smoke highlighted one rotor with an unexpected orientation (see Chapter 5) – which otherwise would have remained undetected emphasizing the value of using smoke. It quickly became apparent that one grenade did not provide sufficient smoke to visualize the airflow. It is recommended that five to 10 grenades be triggered simultaneously. It is recommended to attach a line to the balloon and to attach two grenades every 3m. These experiments need to be conducted safely; enough distance is to be left between the balloon and smoke grenade, helium can be used instead of hydrogen or even better, a drone can carry the smoke grenade. However, with exception of good photos and improved understanding of features, smoke trails can't be quantified scientifically. However, smoke remains good for visualisation and can play a major role in designing an experiment.

4.3.6 Dronesondes

Research drones could be a viable option and may provide new dimensions to an experiment. The advantage of a drone is the flight path is dictated; making it more useful than free soundings. A drone could effortlessly measure in a grid, where free-soundings measure where the wind takes them. It was initially planned to incorporate measurements from a drone in this research; however, the drone company downscaled and withdrew from the project. Some background about drones used for meteorological measurements are provided here.

The drone has to be strong enough to withstand the heights and wind strengths expected to be measured in the experiment. The downward force of the drone propellers could be too strong resulting in unusable atmospheric measurements. A way to circumvent this is to fit the equipment some distance above the propellers. It is also essential that the drone is programmed to produce drone tilt, location, height and time throughout the flight. These measurements, with the exception of drone tilt, could be achieved by attaching a radiosonde to the drone; with the added benefit of environmental temperature and pressure being reported. Lastly, the drone has to be fitted with the rest of the measurement equipment.

Measuring wind strength and direction, is the greatest challenge. An old-fashioned wind anemometer, not perpendicular to the wind, rotates slower and needs to be corrected for. Vector analysis could be used to determine the true wind speed if the drone tilt and the sensors angle to the wind is known. A sine-type graph is expected – using this, the wind can be corrected by a factor if the tilt angle is available. However, a sonic wind sensor is recommended and will most likely render more accurate results. A correction with a sonic wind sensor and the drone tilt can easily be completed through vector analysis. A wind tunnel is ideal for preliminary tests.

4.4 SUMMARY

This chapter leads on from Chapter 3 and discusses the first aim of the project. The experiment design is laid out and the lead-up to the experiment forms the basis of the chapter. The location and rationale of all AWS and radiosonde release locations are discussed. The concluding section of this chapter discusses experiments which were explored, but not feasible for inclusion in the final experiment.

CHAPTER 5 : DATA ANALYSIS

In this chapter, all data analysis is covered. The analysis consists of longer-term analysis (as defined in Section 3.3 and Table 3.1), and upper air analysis (which contains event data analysis). An analysis of all calculated parameters follow and features are analysed individually namely, blocking, gap flow or mountain waves. The features are also analysed to identify which feature exacts the greatest influence on its surrounding as well as which feature produces the most wind shear and the most turbulence.

5.1 LONGER-TERM ANALYSIS

This section discusses the AWS measured winds and how they correlate or differ qualitatively from the climatological wind. The windroses of Figure 5-1, present wind speeds and wind directions measured by all stations. A strong zonal wind component is observed in the windroses of the permanent stations (Port Elizabeth, Cape St Francis and the windfarm); which is in agreement to the climatology (see Section 3.1). An anti-clockwise wind direction shift, with height, is evident in analysing Africa Peak and upwind windroses (Figure 5-1 & 5-2). The Cape St Francis and windfarm wind directions are parallel to the Kareedouw ridge thus, suggesting the barrier blocked and deflected the winds to parallel to the barrier. The Africa Peak wind directional shift from the blocking winds (winds parallel to the ridge) suggests, on average, that it is located above this blocking region; consistent with literature (Neiman et al., 2010).

Throughout the study period, Africa Peak (1 in Figure 5-1) measured the strongest wind speed of 35.2ms^{-1}; with a gust of 44.7ms^{-1}. The Africa Peak wind speed dominates all other wind speeds in strength; which is attributed to the acceleration of the compressional effect above the ridge (similar to what Barry (1981) suggested). The increase in wind speed cannot be merely attributed to the normal speed increase with altitude, as radiosonde data indicated wind speeds dropping a few hundred meters above the Africa Peak height (however, this discussion is for AWS data and refer to Section 5.2.2.1.1.). Camo AWS (3 in Figure 5-1) measured the second highest wind speed with a 23.2ms^{-1} 10-minute average wind speed and a gust of 32ms^{-1}. The windfarm and Port Elizabeth observed, jointly, the third highest wind speed; followed by St1_baro and Cape St Francis. The low standard deviation of Camo average wind speeds shows that this is a more consistent average wind speed. Contradictory to this, the high standard deviation from the wind gust at this station,

shows this location experiences a large difference between the 10-min average wind speeds and wind gusts. This infers stronger gusts or gusts more frequently at the Camo station; second only to Port Elizabeth. Opposed to the Camo AWS (gap winds), the upwind AWSs indicate a lower uniformity in average wind speeds, together with a lower frequency of wind gusts. To isolate the effect of blocking, gap flow and mountain waves, Figure 5-2 considers cases where the environmental winds measured southwesterly wind directions (Port Elizabeth wind directions from 180 to 270°) with wind speeds greater or equal to 7ms^{-1}.

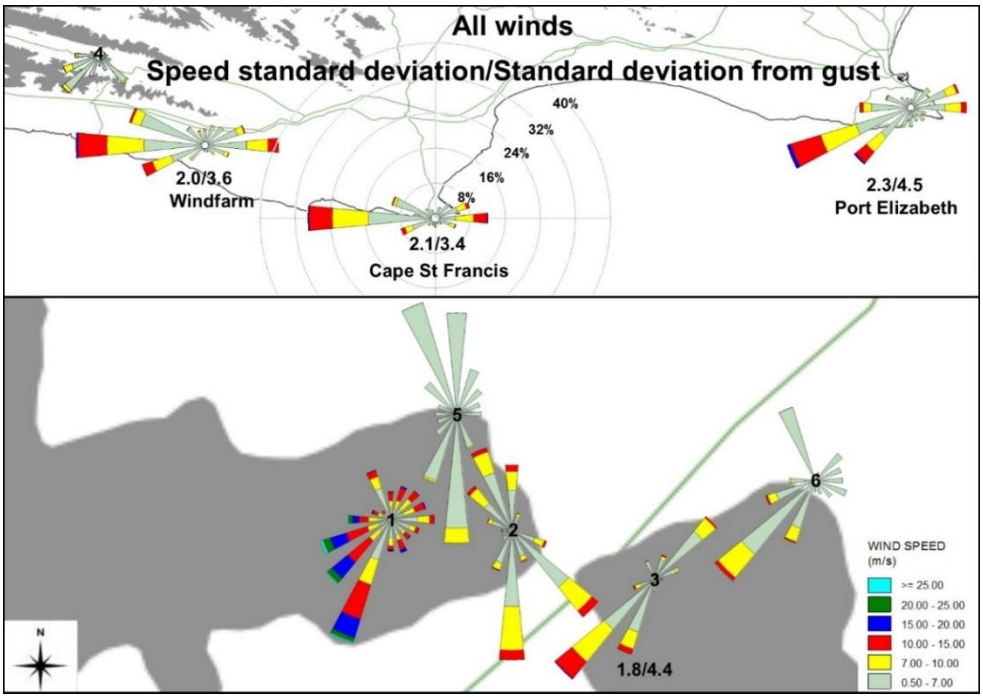

Figure 5 - 1: Map of the study site and surrounding area, where grey represents all topography exceeding 500m amsl. The semi-permanent windroses are numbered similarly to Figure 4-2. Windroses represent all winds and indicate the standard deviations below the rose; deviation from average wind speeds/deviation from gusts. All windroses are similarly plotted to Cape St Francis; on a 40% frequency windrose (meaning the outer ring represents 40% of the winds). Note the vast change in wind direction from the dominant westerly component at the Windfarm, Cape St Francis and Port Elizabeth compared to the southerly wind component in the gap.

Studying the windfarm windrose, almost all winds are deflected to an along-barrier wind direction. Provided that almost no wind directions at the windfarm exist that is close to perpendicular to the barrier; all southwesterly winds are blocked and deflected by the barrier during the study period. Interestingly, Port Elizabeth observes no southerly wind direction with a wind speed greater or equal to 7ms^{-1} (Figure 5-2); this is attributed to the study site being located in the mid-latitudes. However, this was an excessively dry season for this area

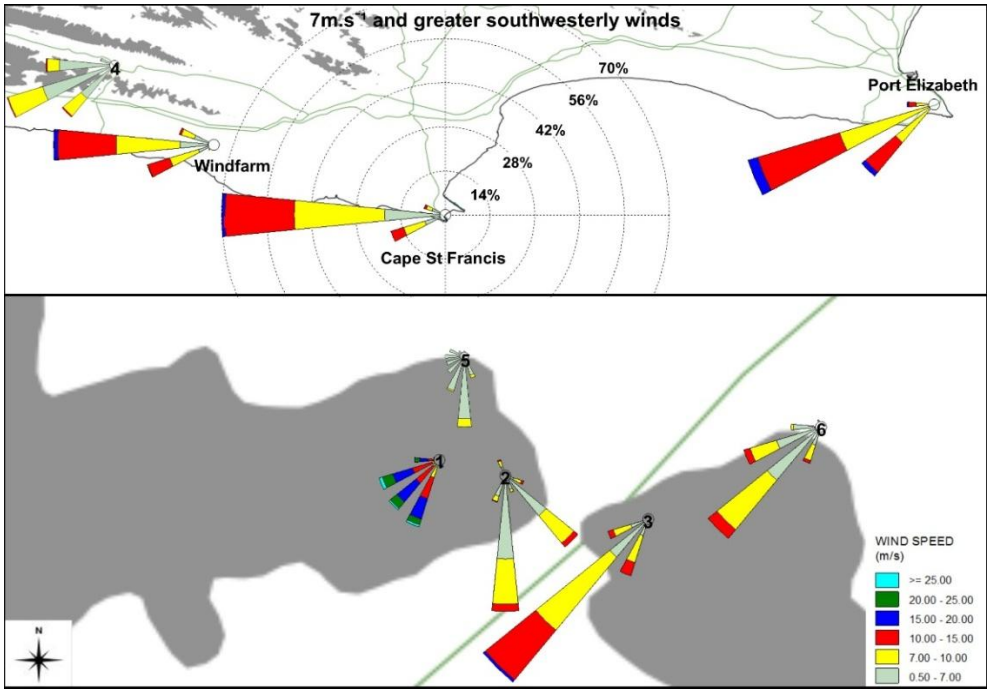

Figure 5 - 2: Windroses represent winds of when the environmental winds (Port Elizabeth) measured 180-270º (termed southwesterly) greater or equal to 7ms^{-1}. Grey represents all topography exceeding 500m amsl and the AWSs are numbered similarly to Figure 3-1 & 5-1. All windroses are similarly plotted to Cape St Francis and represent a 70% frequency windrose.

and might not be an absolute true representation. The Port Elizabeth windrose (Figure 5-2) suggests in this study all blocking, gap flow and mountain wave interactions occur when southwesterly winds occur (230 - 270°). The Cape St Francis windrose closely represent the windfarm windrose, while differing from the environmental windrose (Port Elizabeth). Given that the Cape St Francis windrose simulates the windrose in the blocking regime (windfarm windrose), it can be said that the blocking jet extends to Cape St Francis and thus beyond the end of the Kareedouw ridge; which is responsible for its formation. Windroses in the gap (bottom Figure 5-2), confirms gap flow is present in the 60 - 90° wind direction deviation from the blocking region; deviating to a more southerly direction. Wind speed in the gap is slower than in the blocking regime with limited observations greater than 15ms^{-1}. Total average wind speeds (calculated over the availability periods) revealed; Cape St Francis with the strongest wind speed of 5.8ms^{-1}, Port Elizabeth (environmental wind) in second place with 5.6ms^{-1} and Camo (gap wind) rivalling in third place with 5.5ms^{-1}. Evaluated for wind strength, the blocking region dominates (windfarm and Cape St Francis winds), followed by environmental (Port Elizabeth) and gap (Camo) wind speeds. Even though the gap wind speeds are similar to the environmental wind speed, the 90° wind direction change

suggests gap flow is significant and will induce directional shear leading to turbulence (significant for low-level flying). To briefly apply this to the agriculture sector, the sharp directional changes in such a localized environment can have a marked influence on erosion and soil transport if correct agricultural practices are not employed. For example, if an orchard or tree lane in the gap region is planned according to the general wind direction of the blocking regime erosion of the topsoil would be rapidly eroded. This highlights the need for a fine scale study as opposed to large scale studies, not only for the agricultural sector, but all sectors.

The southern section of the gap windroses mimics one another in Figure 5-1 and 5-2; from this one can say that gap flow takes place either, in conjunction with blocking or it is driven by blocking. The wind direction of the upwind blocking jet (windfarm) greatly minimises the exposure of the gap; reducing its cross-sectional area. Gap flow is, therefore, more likely driven by blocking. Blocking can enhance the temperature and pressure gradients and can result in the spilling of blocked flow through the gap; rather than the winds forcing their way through the gap (as in conventional Venturi theory). A typical example of a strong pressure gradient would be, when blocking increases the pressure upwind and the continental low is situated over the interior; keeping the Midvalley AWSs pressure low.

Wind directions and wind speeds in Figure 5-3 plainly show the effect of across-barrier pressure gradients on the wind. The strong negative pressure gradient windrose (Class 1 in Figure 5-3) exhibits 90% of flow from the southwest as well as, stronger winds (greater frequency of the 10-20ms^{-1} wind speeds) than in any of the other windroses. A slightly weaker pressure gradient (-3 to -2hPa – Class 2) presents 70% of wind flow from a southwesterly wind direction, with the largest portion of wind speed observations located in the 10-15ms^{-1} class. Class 3 (-2 to -1hPa), presents a decrease in the frequency of flow from the southwest and interestingly, 30% of flow now origninate from the northeast. A higher pressure in the Langkloof valley (Midvalley AWS – 4) and a lower upwind pressure (windfarm AWS) results in a dominant northeasterly wind direction in the gap (Class 4). The weakest pressure gradient (Class 4) accounts for the lowest frequency of wind flow from the south west and the lowest frequency of the 10-15ms^{-1} wind speed class. Another observation is that stronger negative pressure gradients (Class 1) result in an anti-clockwise turn with an increased frequency of south-southwesterly wind directions. An example of a strong negative pressure gradient would be on a clear day when blocking increases the upwind pressure and the daytime thermals north of the ridge rise to reduce the pressure on the lee side. This will result in strong windflow from south of the ridge to the north of the ridge.

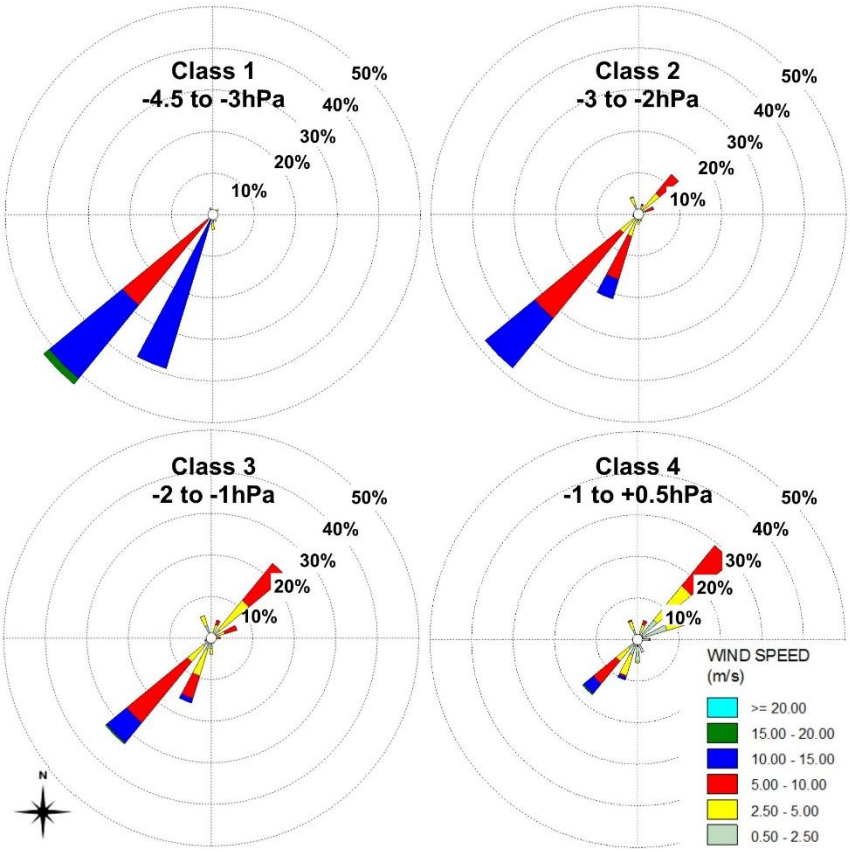

Figure 5 - 3: Camo AWS windroses for four different pressure classes; determined by subtracting windfarm AWS from Midvalley AWS pressures which has been reduced to sea-level pressure. The legend is slightly adapted, from previous windroses, to be more sensitive to weaker wind speeds. Note the dominant northeasterly component with a positive/weak gradient and southwesterly wind directions with a strong negative pressure gradient.

The temperature gradient windroses of Figure 5-4 demarcate a similar but opposite tendency to the windroses in Figure 5-3. The 5 to 10°C temperature gradient (Class 1), results in ±65% of wind directions from the southwest. Class 2 exhibits ±60% of wind directions from the southwest, with a slightly greater than before westerly component. Interestingly, this class is associated with the maximum wind speed (thin strip of 15-20ms^{-1}). Class 3, the weak negative temperature gradient, causes a definite changeover from dominant southwesterly wind directions to northeasterly wind directions. Contrary to the tendency observed in the pressure gradient winds, the stronger negative temperature gradient windrose (Class 4) depicts less defined wind directions and lower wind speeds. In the daytime, a warm continental interior and a cool oceanic temperature would cause a typical example of a positive gradient.

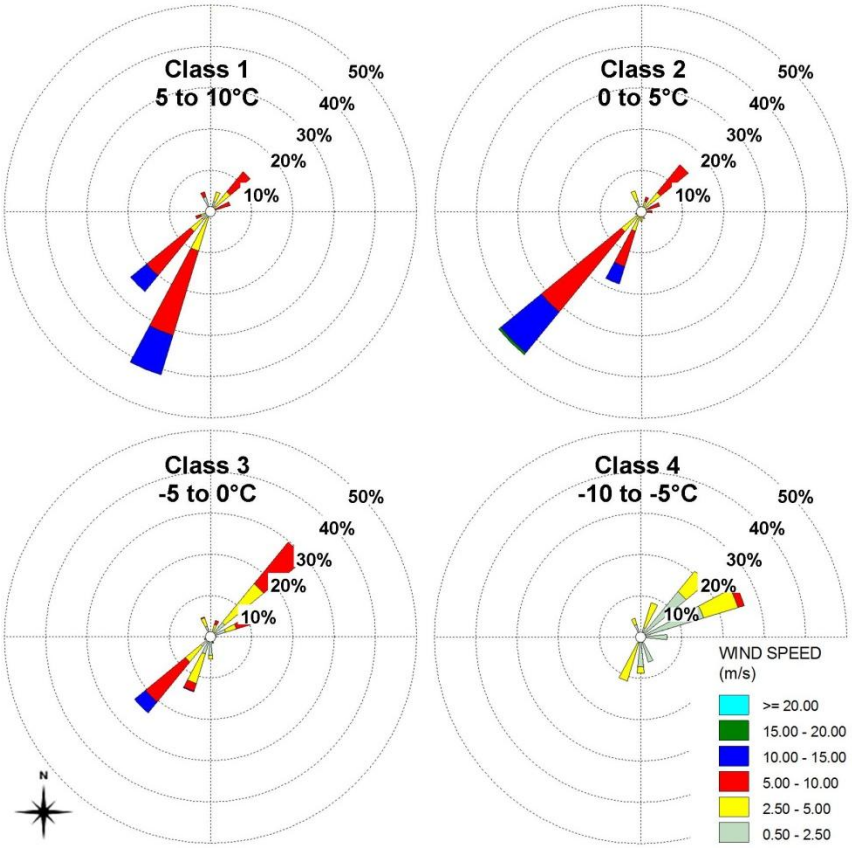

Figure 5 - 4: Windroses of Camo wind directions and wind speeds, for different temperature gradient classes, are determined by subtracting windfarm AWS temperatures from Midvalley AWS temperatures. Note that the strong southwesterly wind component for the positive temperature gradients.

The daytime Camo windrose, in Figure 5-5, corresponds closely to Class 2, in Figure 5-4. Similarly, the night-time windrose corresponds to Class 3, in Figure 5-4. Considering the gap location, this relates to a warmer daytime valley with a cooler upwind side as influenced by the ocean. Overnight cooling of the land, while the ocean retains its heat, provides a negative temperature gradient. Class 2 and 3, in Figure 5-4, mainly consist of day and night temperature gradients.

A low-level inversion is more probable at night and should act as a lid, causing acceleration in wind speeds similar to the Venturi-effect. However, when examining the Camo windroses for the day and night hours, the day-time winds are stronger. This may present a falsely view; that the nocturnal inversion does not aid to accelerate wind speeds at night. However, the truth is that the across-barrier temperature gradient during the day results in stronger gap wind speeds and thus contaminating the nocturnal inversion investigation. The effect of the daytime temperature gradient is substantiated by, the environmental wind speeds (Port Elizabeth windrose in Figure 5-5) being stronger in the day

as well as the above-mentioned investigation; regarding Figure 5-4. To remove all temperature and synoptic forcing, the environmental wind speed (Port Elizabeth) was subtracted from the Camo wind speeds, producing normalised windroses (Figure 5-5 right). Night-time windroses, in Figure 5-5 & 5-6, has stronger wind speeds with a greater frequency of positive wind speeds. To briefly apply this to the renewable energy sector would mean that there is generally stronger winds during the day leaving a deficiency during the evening, no matter the location. This deficiency is exacerbated by solar panels not producing electricity at night. To make optimal use of the wind at night is thus key and a good position to do this is in the gap.

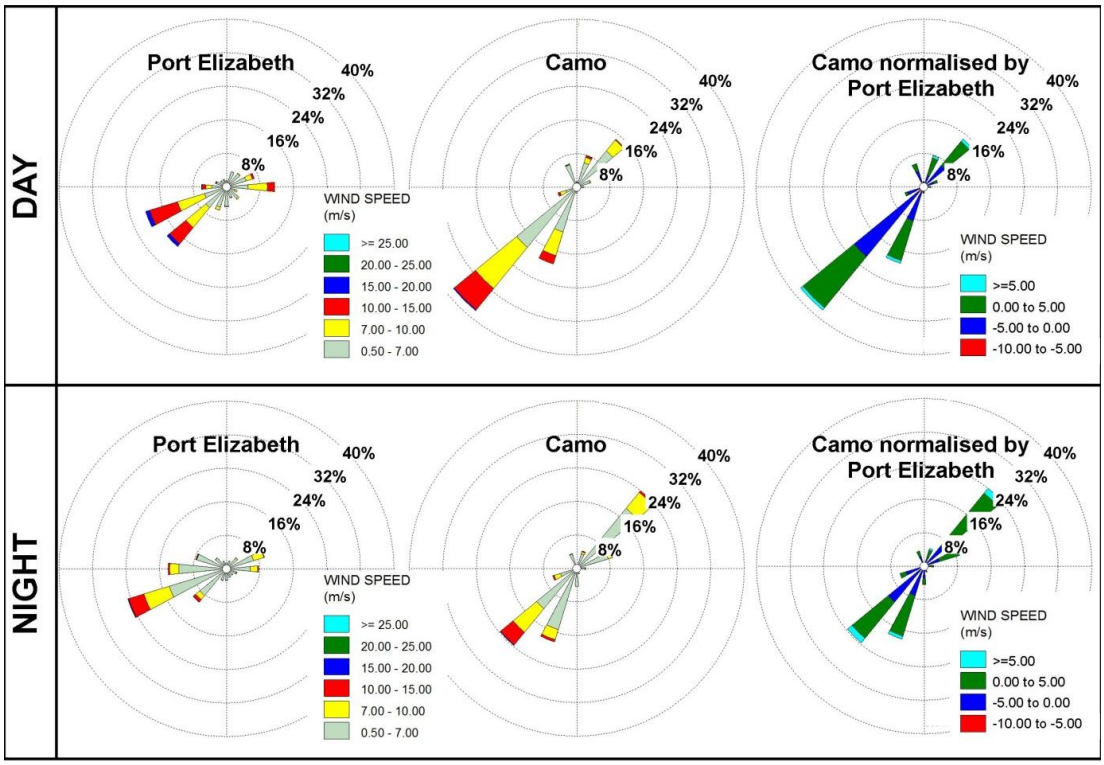

Figure 5 - 5: Nocturnal effects on gap flow, illustrated by the environmental windrose (Port Elizabeth), the gap AWS windrose (Camo) and a normalised windrose for the day (6:00-17:50) and night (18:00-5:50) hours. The Camo AWS represents the gap wind directions and wind speeds. The normalised windrose demarcates Camo wind directions and wind speeds accordingly (Camo wind speeds - environmental wind speeds). The normalised windrose shows that stronger winds occur under the nocturnal inversion.

The peak shift during night hours, in Figure 5-6, suggests that wind speeds are differently affected at night than during the day. The higher number of positive normalised wind observations indicate that gap wind speeds are stronger than environmental wind speeds at night, suggesting that the nocturnal inversion positively influence gap wind speeds. Investigating event data, one event included radiosonde ascents at sunrise. However,

investigating an ascent temperature at sunrise (Figure 5-8), no low-level inversion close to ridge height is detected. One possible factor responsible for no inversion is the turbulent environment; that would quickly destroy a nocturnal inversion. Another possibility is that the inversion is not the responsible factor but rather another process. One such a process can be katabatic flow down the mountain enhancing speeds (as on Figure 5-6), but one have to question why anabatic winds at daytime not result in the same speed increase. To study this effect of the nocturnal inversion, ascents are required during weak synoptic and non-turbulent conditions. The reader is reminded that a very short data span were available for the Midvalley AWS (Table 3-1), on which this analysis was based.

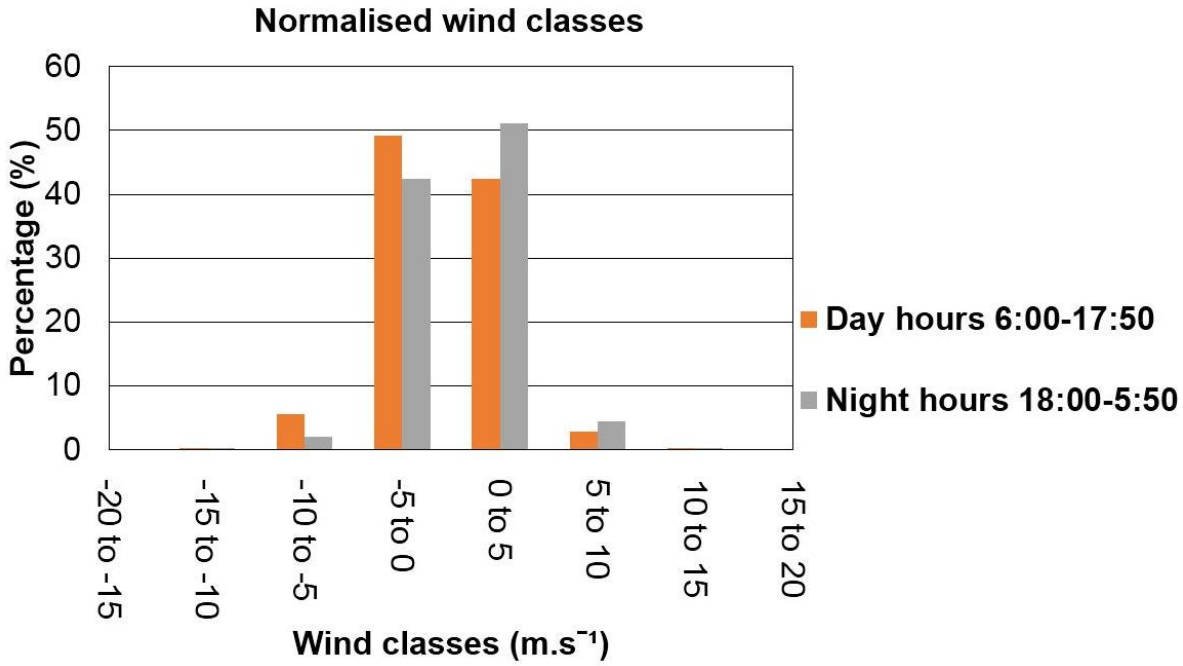

Figure 5 - 6: Day and night hours, normalised wind speed graph; depicting Camo wind speeds normalised by environmental (Port Elizabeth) wind speeds. The day hours have stronger negative wind speeds and the night hours stronger positive wind speeds.

5.2 EVENT ANALYSIS

Nineteen radiosonde ascents sampled six events, during the period of June to December 2017. The event of 26 October 2017 formed the basis of analysis as it comprised of the full experimental data and consisted of a good blend of blocking, gap flow and mountain wave processes. In this section, all discussions and figures pertain to the event on 26 October 2017, unless otherwise stated.

5.2.1 Event investigation

The event on 26 October 2017, consisted of five radiosondes; one at each release location and two in the gap location (Figure 3-1). A break of 2.5hrs, separated the two Gap radiosondes. The event span was from 06:30 to 13:30. During this period no precipitation was observed and the event is classified as uninfluenced by downdrafts; induced by precipitation. A weakened tail of a cold front is observed on the bottom right of the satellite image with showers offshore of the coast, in Figure 5-7. The unstable showers suggests an unstable environment; which is confirmed by the unstable skew-T in Figure 5-8. The skew-T indicates a conditionally unstable layer from the surface, capped by a strong inversion at 2500m; which should reflect mountain waves if formed. Another factor possibly contributing to the instability, is the interaction of the post-cold frontal air drifting over the warm Agulhas current (which is identified by the line of showers stretching from Plettenberg Bay (PB – Figure 5-7 & 5-9) parallel up the coast toward the east).

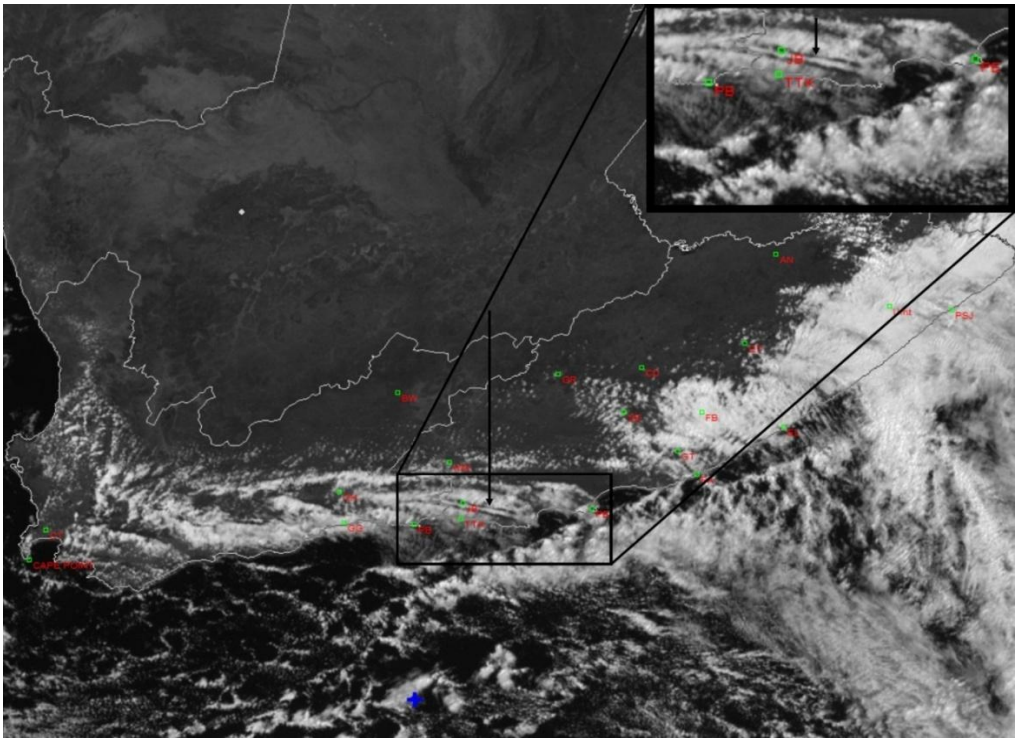

Figure 5 - 7: High-resolution visible Eumetsat Meteosat Second Generation satellite image at 14:00. The arrow indicates the study site. The inset indicates a primary mountain wave over the Tsitsikamma/Kareedouw ridge. Towns within the inset include Plettenberg Bay (PB), Tsitsikamma (TTK), Port Elizabeth (PE) and lastly, in the Langkloof valley between the Tsitsikamma and Suuranys ridges - Joubertina (JB). Image copyright Eumetsat 2017.

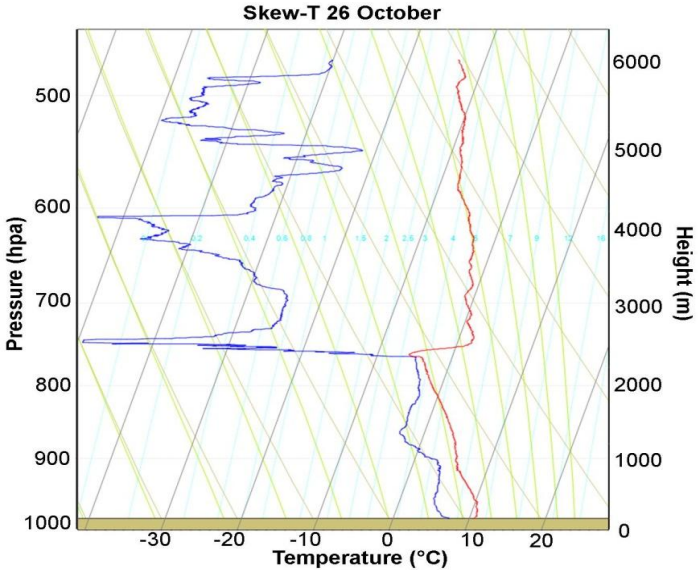

Figure 5 - 8: Skew-T plot of the Upwind radiosonde on 26 October 2017. Note the unstable layer from 400m, capped by a strong inversion at 2500m.

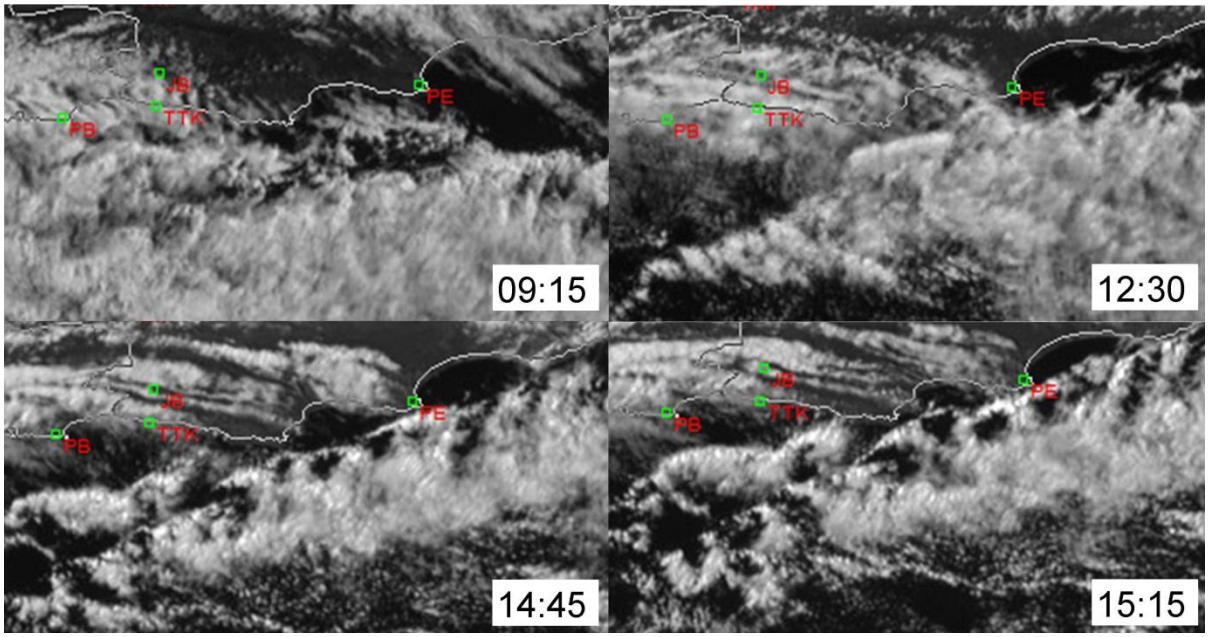

Figure 5 - 9: Evolution of mountain waves with time, as observed from the high-resolution visible Eumetsat Meteosat Second Generation channel. Image copyright Eumetsat 2017.

The satellite image (Figure 5-7) portrays a primary mountain wave over the Tsitsikamma/Kareedow ridge. Four satellite images, in Figure 5-9, show the evolution of mountain waves throughout the day. At 9:15 there were multiple east-northeastward moving, short wavebars. These short wavebars coincide with more cellular clouds closer to the coast; suggesting a more unstable environment. Two hours after the initial development, the short wavebars dissipated and the Tsitsikamma/Karreedouw ridge shaped a stationary mountain

wave (similar to the 12:30 image). By 14:45 the system forms a second mountain wave over the Suuranys ridge and finally, 6hrs after initial development, three mountain wave bars are distinguished.

Analysis of synoptic conditions, reveal a cold front passing south of the study site overnight. Data from European Re-analysis (ERA-interim in Figure 5-10 and 5-11) reveal the cold front, supported by a broad midlevel trough up to 500hPa. On the surface, the high pressure ridges in from behind the cold front. Satellite altimetry confirms offshore southwesterly wind directions; with wind speeds of 10 to 15ms^{-1} (south of the oval Figure 5-12). The wind directions indicate a deflected alongshore wind with the wind speeds broadly increasing towards the coast; with near-shore wind speeds reaching 15 to 20ms^{-1}. Unfortunately, the satellite did not pass directly over the study site, but general wind direction tendencies infer along-barrier wind directions, south of the study site. The change in wind direction near the coast is consistent with the pressure nose suggested by the mean sea level pressure map (Figure 5-10). The pressure nose forms as the pressure increases upwind of the barrier and in the blocking area, altering synoptic conditions.

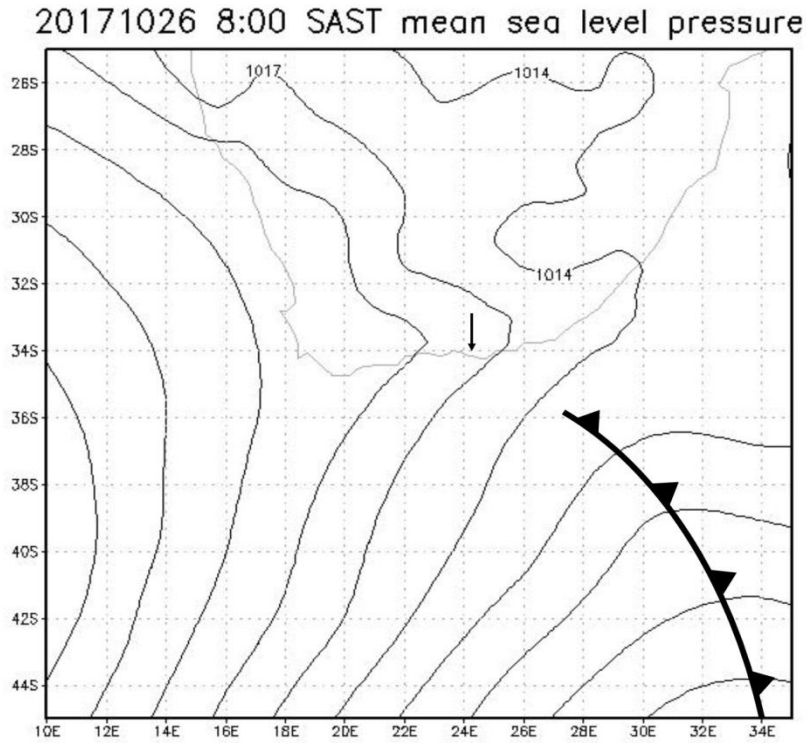

Figure 5 - 10: Mean sea level chart compiled from 75 x 75km ERA-interim data. A surface cold front is indicated in-line with the suggested isobars and the satellite imagery at the time. The arrow indicates the study site – as in all other similar figures.

The sea-level pressure along the coast in Figure 5-10, suggests a west-southwesterly geostrophic wind direction. Applying Feltz et al. (2008), the initial east-northeastward (Figure 5-9) moving mountain waves, infer the same west-southwesterly wind direction at the mountaintop. The wind directions from Africa Peak (red windbarb 1 in Figure 5-13) confirm this concept; however, the Upwind Gap and Midvalley radiosondes (blue windbarbs A, B & C) at ridge height do not. Radiosonde measurements (blue windbarbs A, B & C in Figure 5-13) at peak height indicate a westerly flow with a southwesterly turn at the Suuranys ridge (blue windbarb D). The Midvalley radiosonde (blue windbarb C) wind direction indicates a north-northwesterly channelling down the Langkloof valley. The surface stations indicate a significant wind direction deviation from the observed upper air wind direction, especially in the gap (red windbarb 1, 2 & 3). The maximum wind speed, in Figure 5-13, is observed by the Africa Peak AWS (red windbarb 1) at 25.1ms^{-1}. The Cape St Francis AWS in the upwind/blocking region measures at 19.9ms^{-1} wind speed, while AWSs in the gap (red windbarb 2 & 3) measured the slowest wind speed. In relation to St1_baro (red windbarb 2), the stronger wind speed at the Camo AWS (red windbarb 3 in Figure 5-13) is contributed to the station being more exposed to west-southwesterly wind directions.

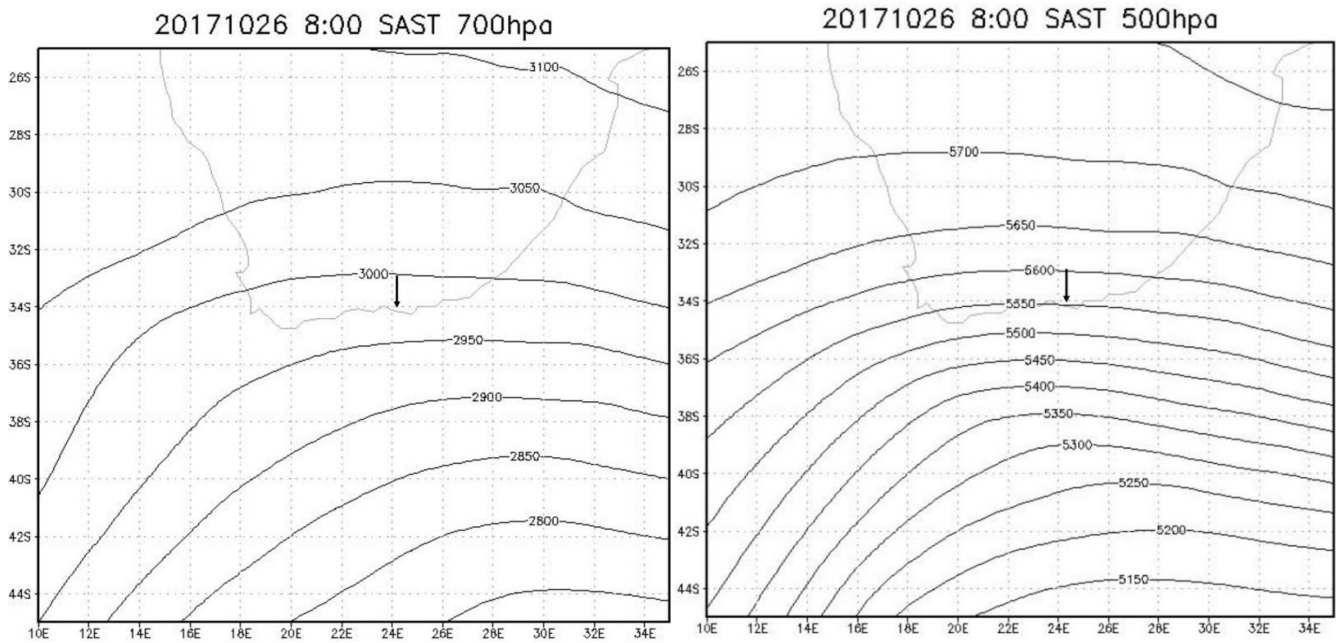

Figure 5 - 11: Upper air analyses for 700 (left) and 500hPa (right) on 26 October 2017 at 08:00. A broad upper trough is identified south of South Africa. The figures were compiled similarly to Figure 5-10.

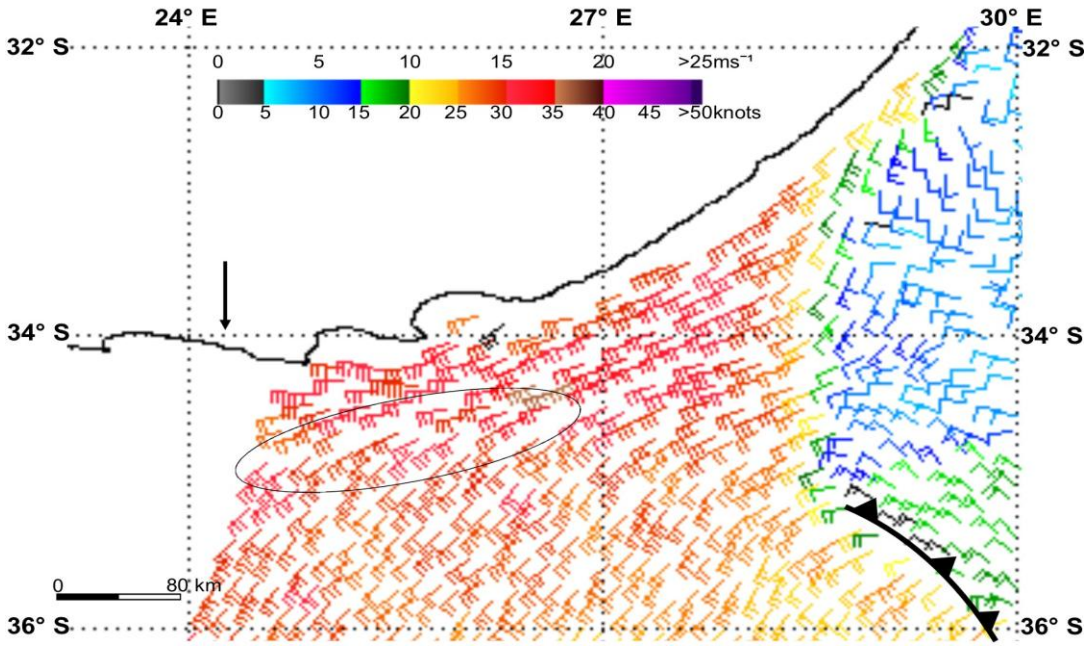

Figure 5 - 12: Satellite altimetry wind directions and wind speeds from NOAA ASCAT-B at 08:46 on 26 October 2017. The weak tail of the cold front is drawn in the bottom right and a wind direction change boundary, encircled. Black wind barbs indicate wind speeds influenced by precipitation and not trusted. A single flag on a barb indicates 5ms^{-1} and a short or half flag demarcates 2.5ms^{-1}.

The wind directions in Figure 5-13, clearly dictates the radiosonde flight paths as depicted in Figure 5-14. All flight paths have a dominant west-to-east direction, with deviations in places. The southwesterly components of the Gap AWS and the Suuranys radiosonde are visible in the interesting kinks in the Midvalley radiosonde (indicated by the stars in Figure 5-14) as well as the Gap radiosonde inset. Graphs in Figure 5-14, denote areas of radiosonde, increased and decreased, ascent rates. To highlight the updrafts and downdrafts more clearly, the cumulative normalised ascent rate (dash-dot line) is plotted on the height versus distance profiles. The vertical lines on the graphs indicate areas where the updrafts and downdrafts of the respective radiosondes correlate. Further analysis of the graphs, reveal updraft and downdrafts exceeding 5km in altitude. Figure 5-14, in detail, discussion to follow later in the chapter.

5.2.2 Diagnosing incoming flow interacting with terrain

The layered Froude number (Figure 5-15) has a minimum value of ~0.14, from 260 to 460m. This minimum, below mountaintop, specifies the area of maximum blocking, while a sharp increase from 460 to 700m implies a weakening in the blocking regime. The

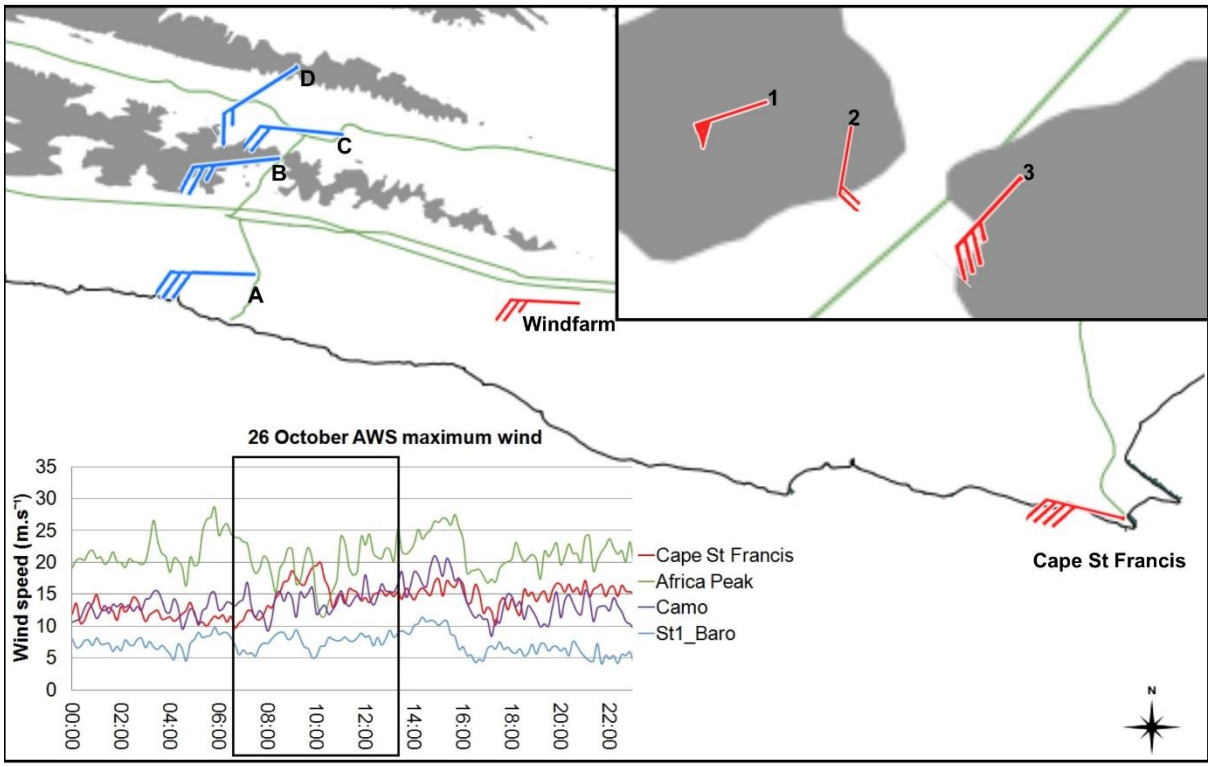

Figure 5 - 13: Map surrounding the study area depicting wind barbs. Red wind barbs indicate maximum wind speeds and average wind directions as observed by AWS stations during the event. Blue barbs indicate radiosonde measured wind directions and wind speeds at peak height (819m), and plotted at the release location. A triangle flag on a barb indicates 25ms^{-1}, a single flag indicates 5ms^{-1} and a short or half flag demarcates 2.5ms^{-1}. At this time the Africa Peak wind sensor was confirmed faulty and is used here as an underrepresentation of true values. The wind speed graph indicates the evolution of the 10-min maximum wind speed throughout the day, with the event hours highlighted in the block. Grey represents all topography exceeding 500m amsl.

weakening of the regime is attributed to the height (460m) of the gap. The increase in the Froude number at gap level, suggests that air flows through the gap, weakening the blocking region and forming gap flow. The calculated mountain Froude number of 0.35-0.5 (by employing two different layered averaging methods), propose that mountain waves can form. However, considering the mountain wave formation criteria of section 2.1.3, the wind direction should limit mountain wave formation.

5.2.2.1 Blocking

Blocking parameters provide information and estimations on the blocking region and its associated jet. The Burger number (Equation 2.4) was much greater than 1 and further

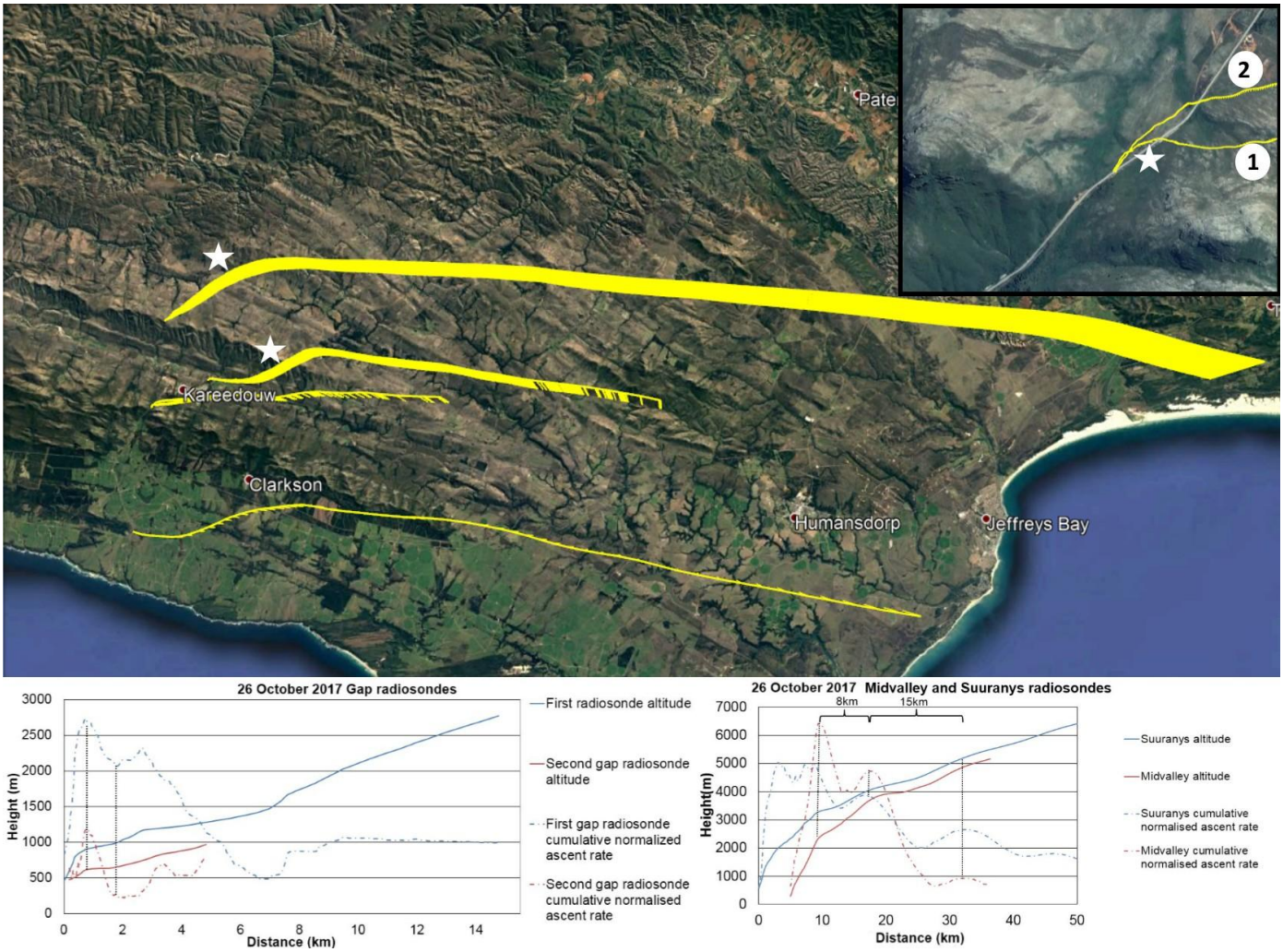

Figure 5 - 14: Radiosonde flight path overlaid on Google Earth. The top right inset depicts the first (1) and the second (2) radiosonde flight paths in the gap region. The radiosonde height profiles (solid lines) and the cumulative normalised ascent rates (dash-dot lines) are illustrated at the bottom. To make the Midvalley and Suuranys radiosondes more comparable, the Midvalley radiosonde were adjusted by the distance it is downwind from the Suuranys release location; 5km. The stars indicate the interesting kinks in the radiosonde flight path.

indicates (with the Froude number) that blocking is complete. This implies that below 819m, flow runs not over the mountain, but is rather deflected. The Froude derived height scale (Equation 2.3), suggests a shallow blocking jet depth of 210-300m (depending on which layered averaging is employed). The jet top is thus, established between 420-510m amsl and correlates to the observations in Figure 5-15 & 5-16. In Figure 5-16 (right), the rapidly increasing ù (along-barrier) wind becoming abruptly constant, from 520m, confirms the jet depth. Provided the Froude number is less than one, condition 1 of Equation 2.5 and 2.6 is

applied. The Rossby Radius equation, suggests a jet width of 39km and the thermal wind equation proposes a 3.1ms^{-1} increase in the ù wind.

Satellite altimetry observations, consistent with literature, illustrate an increase in wind speed with a wind direction change; to a barrier parallel wind direction (Overland & Bond, 1995). The encircled area in Figure 5-12, characterises the narrow zone between the environmental winds and the winds blocked by the Kareedouw-Tsitsikamma ridge. The satellite altimetry, in Figure 5-12, proposes a jet width of at least 80km; double the width the Rossby Radius suggested (39km). In Figure 5-12, the observed stronger winds are consistent with the thermal wind proposition as postulated in Section 5.2.1, but futher investigations are required to confirm this. Radiosonde data, in Figure 5-16 (middle), display a blocking jet with a maximum wind speed of 16.5ms^{-1}; maintained from 520 to 680m before decreasing in wind speed of up to 1000m. The blocking jet is nearly parallel to the barrier and the maximum wind speed consists of 15.9ms^{-1} ù wind and 4.5ms^{-1} ù (cross-barrier) wind (Figure 5-16 right). The ù wind increases from surface to well above the mountaintop; possibly attributed to an increase in height. An increase in height takes a parcel closer to the gap height, or if already above gap height, the gap widens and airflow can more easily spill to the lee side; ultimately increasing the ù wind with height.

The strongest blocking event was observed on 8 June 2017 (Figures 5-17 & 5-18). The 8 June 2017 event is the only event that observes the maximum wind speed of the day in the blocking region (Figure 5-18 middle & right). The maximum wind measures 24ms^{-1} ù wind and a total wind speed of 26ms^{-1} from direction 270°. The maximum wind speed occurs at mountain height and increases by 11ms^{-1} from the surface measurement; of 15ms^{-1}. The change in wind direction (Figure 5-18 left) and decrease in ù wind speed above mountain height, indicates a rapid deterioration in the blocking characteristics. The 8 June 2017 event, calculated a mountain Froude number of 0.5, with the height scale underestimating the blocking jet depth by 300m. The Rossby Radius suggests a width of 65km and the thermal wind equation a wind speed increase of 5ms^{-1}; unfortunately, no satellite altimetry was available to test the accuracy of these parameters.

The only event deviating from the general findings, as far as the blocking region is concerened, is 13 September 2017 (red line in Figure 5-17). Synoptics for 13 September 2017 includes, a pre-frontal coastal low that passed the coastline and produced shallow southwesterly winds. This was influenced by warm prefrontal northwesterly winds above mountaintop; the induced mixing with the cool surface southwesterlies created unfavourable conditions for blocking and mountain wave development. The 13 September 2017 event,

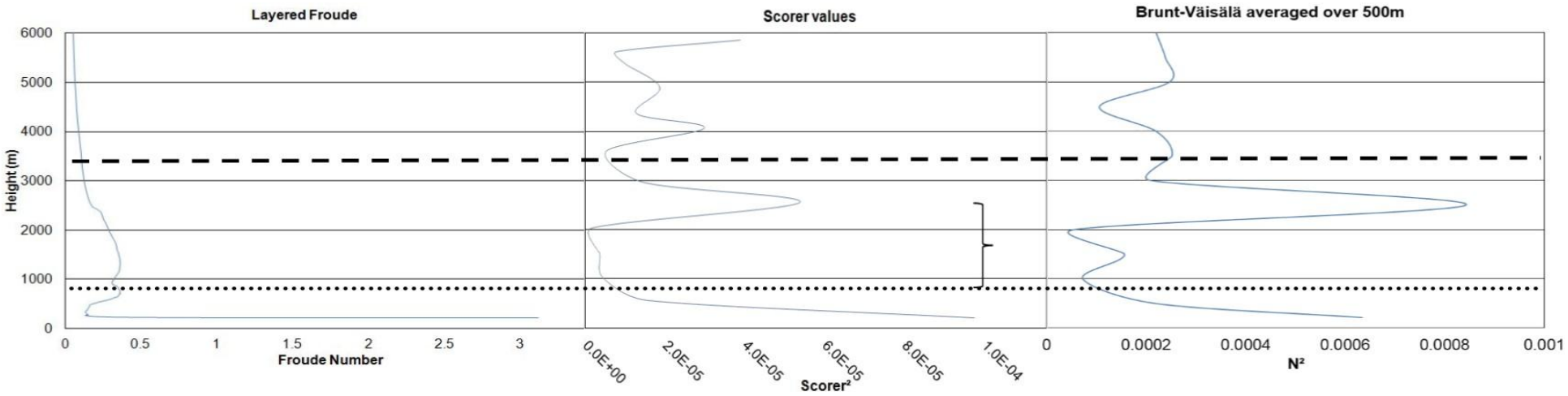

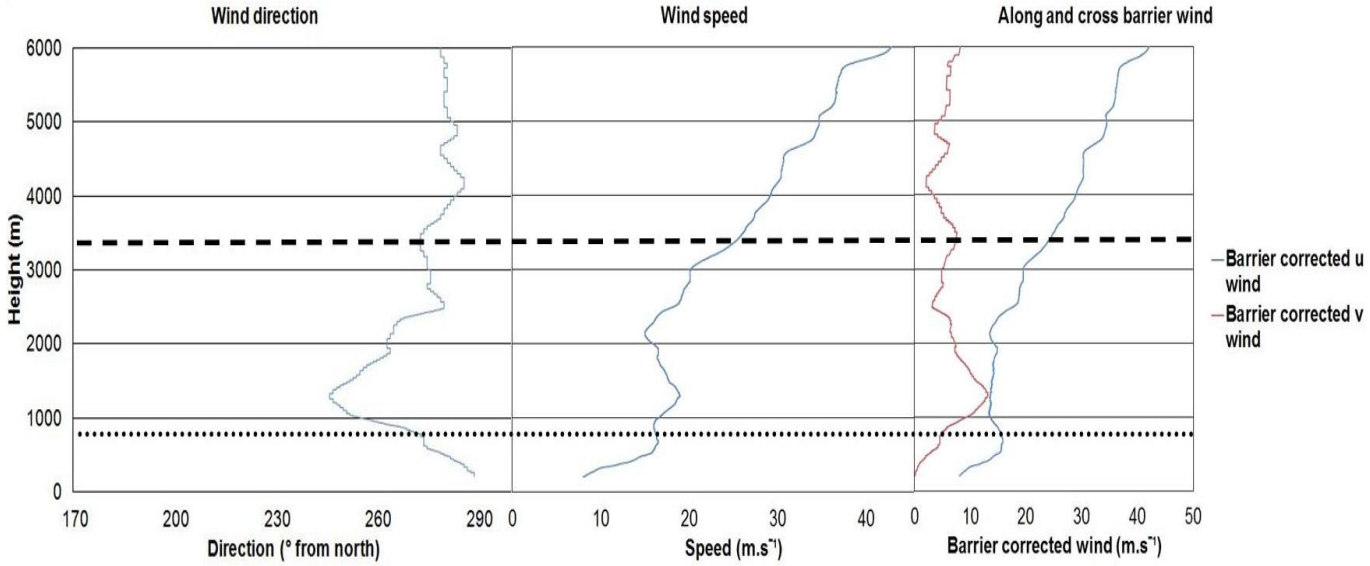

Figure 5 - 15: Calculated parameters from the Upwind radiosonde released at 06:30 on 26 October 2017. The graphs include the layered Froude parameter (layered from the surface to the respective height), Scorer parameter and the Brunt-Väisälä parameter. The block bracket stipulates where the wavenumber suggest trapped mountain waves to develop. The dotted line is the height of Africa Peak and the dashed line is the height where the radiosonde passed over the ridge (3350m), as in all other similar images.

Figure 5 - 16: Upwind radiosonde observed wind direction, wind speed and barrier corrected ù and ѵ winds.

was also the only event without any mountain wave features in the data or on satellite imagery. The rest of the events followed in close simularity and are well represented in the 26 October 2017 event. All observations different from the 26 October 2017 event, are discussed in this dissertation.

5.2.2.1.1 *Turbulence produced by blocked flow*

The blocking regime broadly portrays a turbulence free zone, and is indicated by the little to no fluctuations in the ETI (Figure 5-19). The uniform building to the blocking jet maximum, visible in Figure 5-16 & 5-18 (middle & right), results in little turbulence. Most blocking events highlighted turbulent areas directly above the blocking jet and the ridge height (800-1300m). This transition zone observes large wind direction and wind speed changes (Figure 5-16 to 5-18); responsible for the associated turbulent fluxes. This transition zone originates where deflected blocking jet returns to environmental flow, combined with winds interacting with the barrier as well as a frequently contrasting environmental wind flow.

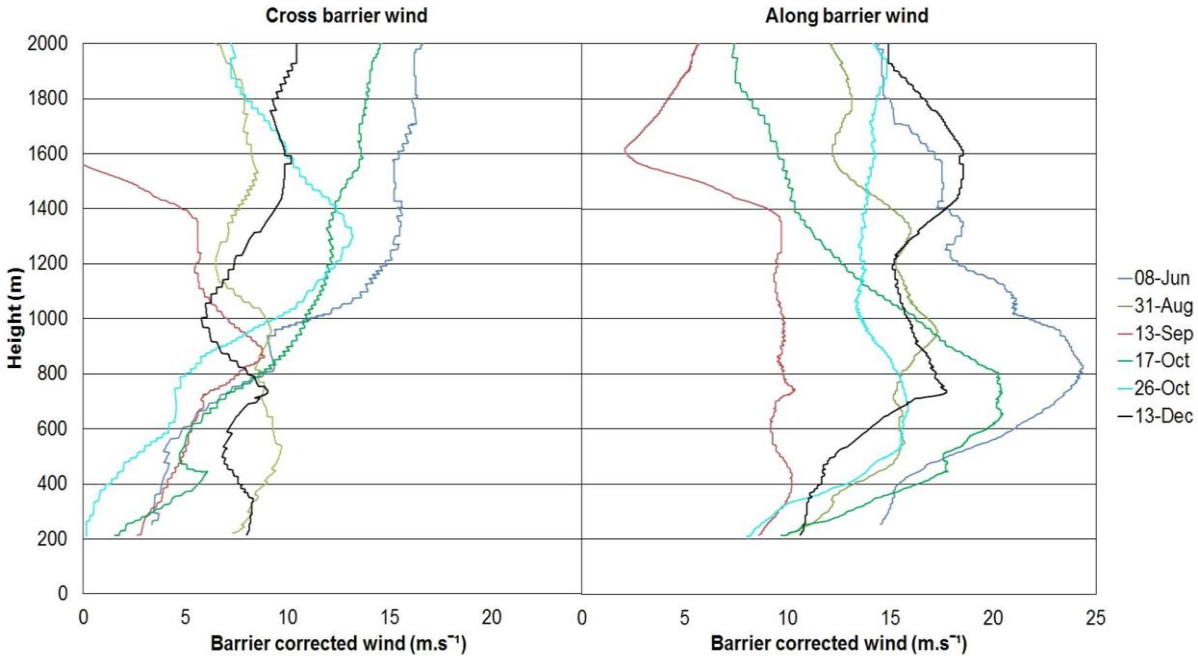

Figure 5 - 17: Barrier corrected ѵ and ù winds of all events. All events depicted a mountain Froude value less than one, indicative of blocking conditions.

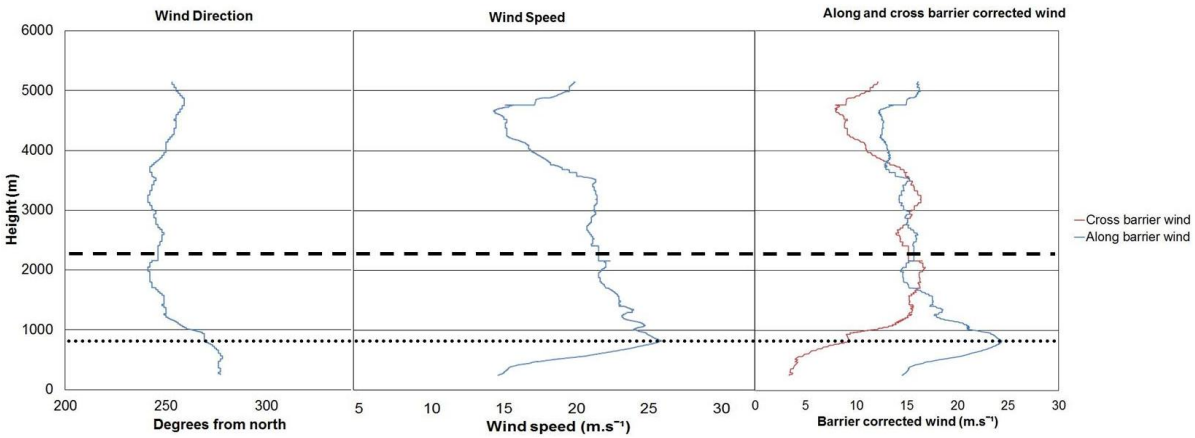

Figure 5 - 18: Wind direction, wind speed and the barrier corrected winds of the Upwind radiosonde on 8 June 2017. Maximum wind speeds, throughout the ascent, occur at peak height. The dotted line is the height of Africa Peak and the dashed line is the height where the radiosonde had passed over the ridge.

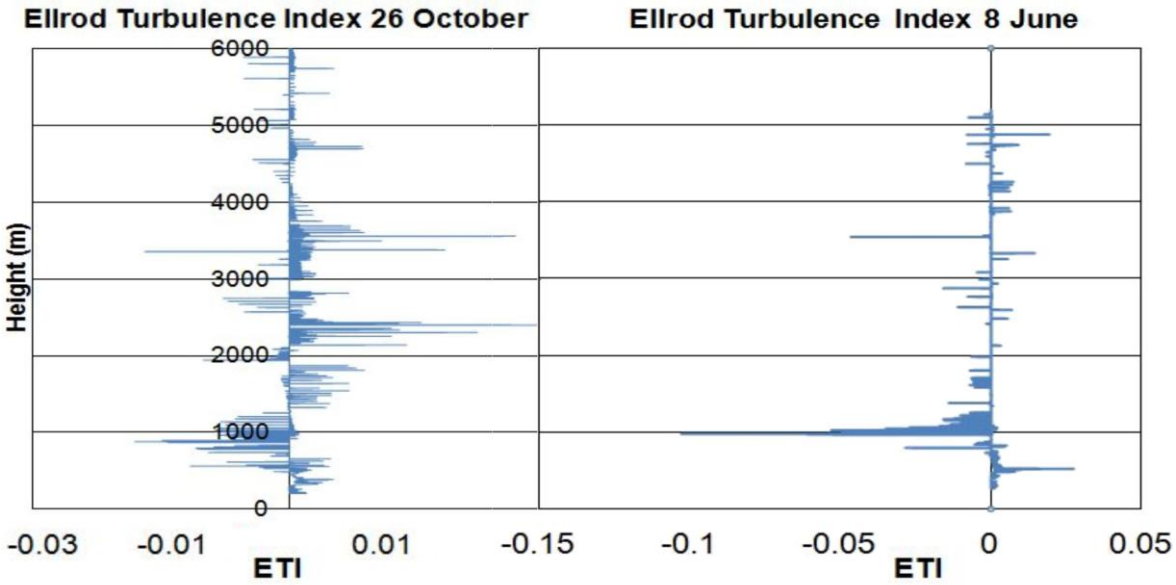

Figure 5 - 19: Ellrod Turbulence Index (ETI) in the blocking regime on 26 October 2017 (left) and 8 June 2017 (right). The turbulent fluxes in the blocking region are significantly lower than the fluxes above ridge height.

5.2.2.2 Gap flow

The weakening in the blocking region, as seen in Figure 5-15 (left – Froude values), is evidence that gap flow is present. The 26 October 2017 event had two Gap radiosonde releases. The first Gap radiosonde deviated strongly to the east (Figure 5-14).

The second radiosonde continued in a north-northeastward direction, joining the mean westward flow down the Langkloof valley and losing signal at 970m amsl. The radiosonde track, in Figure 5-14, presents a deviation from the synoptic west-southwesterly flow and thereby confirming gap flow. Investigating the wind speed at gap level (460 to 819m), two maximums of 12.3 and 12.5ms^{-1} are observed; at 600 and 819m respectively in Figure 5-16 (middle). Similar to the AWS data, the gap jet is significantly lower than the blocking jet (16.5ms^{-1}). This demonstrates that when evaluated for wind strength only, the blocking region produces a stronger jet than the gap region.

All wind direction and wind speed observations, of all the Gap radiosondes, are similar. The wind direction profiles indicate sheared environments, with rapid changes from a southerly to a westerly flow; from the surface to 700m (Figure 5-20 & 5-22). The above-mentioned directional shear, analysed with the top right inset in Figure 5-14, simulates gap divergence or an eddy. All Gap radiosondes (except the 13 September 2017 and the second 26 October 2017 Gap radiosondes) wind speeds increased rapidly with height up to ridge height whereby, the wind speeds weakened or remained constant in height (Figure 5-22 3rd graph from left).

The 26 October 2017 event shows an interesting combination of features. The ѵ wind speed (Figure 5-20 right) remains approximately constant throughout the layer; with two minor peaks of 5.2ms^{-1} (470m) and 5.9ms^{-1} (630m). The ù wind speed increases sharply up to 11.1ms^{-1} at 630m, thereafter it remains almost constant in height. Also at 630m, Froude values change from subcritical to supercritical values (Figure 5-20 left) and irregular potential temperatures are observed (Figure 5-21). Coinciding with this height, is an updraft changing into a downdraft suggesting a wavelike feature; as suggested by the cumulative normalised ascent rate in Figure 5-14. It is noted that the discussed changes, all fall within the radiosonde instrumentation bias; however, provided they all occur at the same height, three potentially severe turbulence producing possibilities are suggested. *Firstly,* a hydraulic jump feature/expansion fan (as expected by Saito (1992) – dotted line in Figure 5-21), *secondly,* downslope mountain winds penetrating from ridge height simulating an expansion fan (as observed by Colle & Mass (2000) – dash-dot line), and *thirdly* the radiosonde measured the change-over from eddy conditions at the gap exit to environmental conditions. The potential temperature analysis, in Figure 5-21, reveals inferred wind flow and displays two possible wavelike features. The analysis in Figure 5-21 rules out the second possibility of winds penetrating from the ridge height; observed in

the Africa Peak potential temperature (287.5K) inferred wind flow not penetrating down the lee ridge.

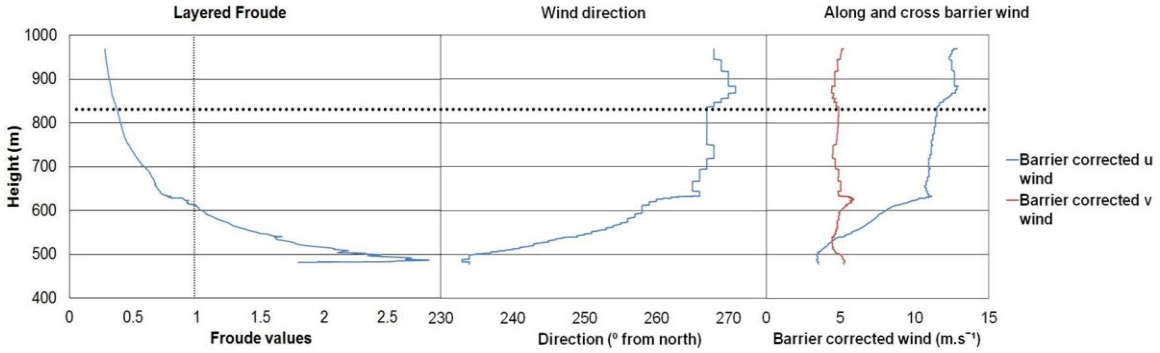

Figure 5 - 20: The second Gap radiosonde of 26 October 2017 depicting the layered Froude, wind direction and barrier corrected wind graphs. The vertical dotted line on the Froude graph stipulates the subcritical to supercritical transition at 630m.

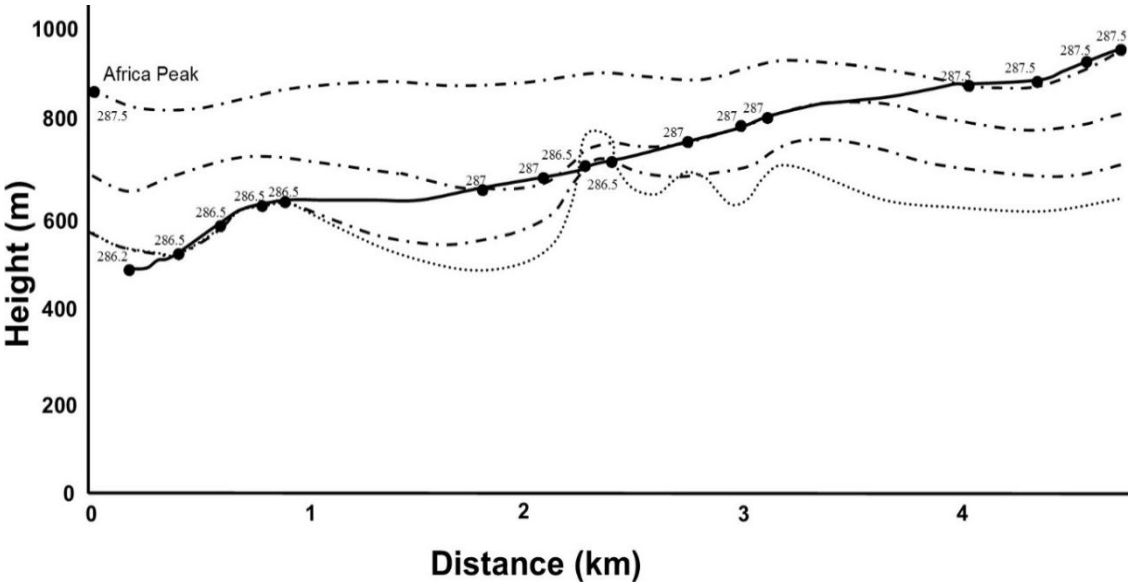

Figure 5 - 21: The potential temperature plot, of the 26 October 2017, second Gap radiosonde representing inferred wind flow at the gap exit. The hand-drawn plot suggests two possible flows. The dotted line indicates a possible expansion fan with a hydraulic jump at 2.2km, downwind of the gap centre-line. The dash-dot line indicates a downdraft from the gap, with a vertical correction simulating an expansion fan at 900m amsl, weakening rapidly downstream. The solid line is the actual radiosonde flight path. Potential temperature from the Africa Peak AWS was plot, in order to rule out downdrafts down the lee slope.

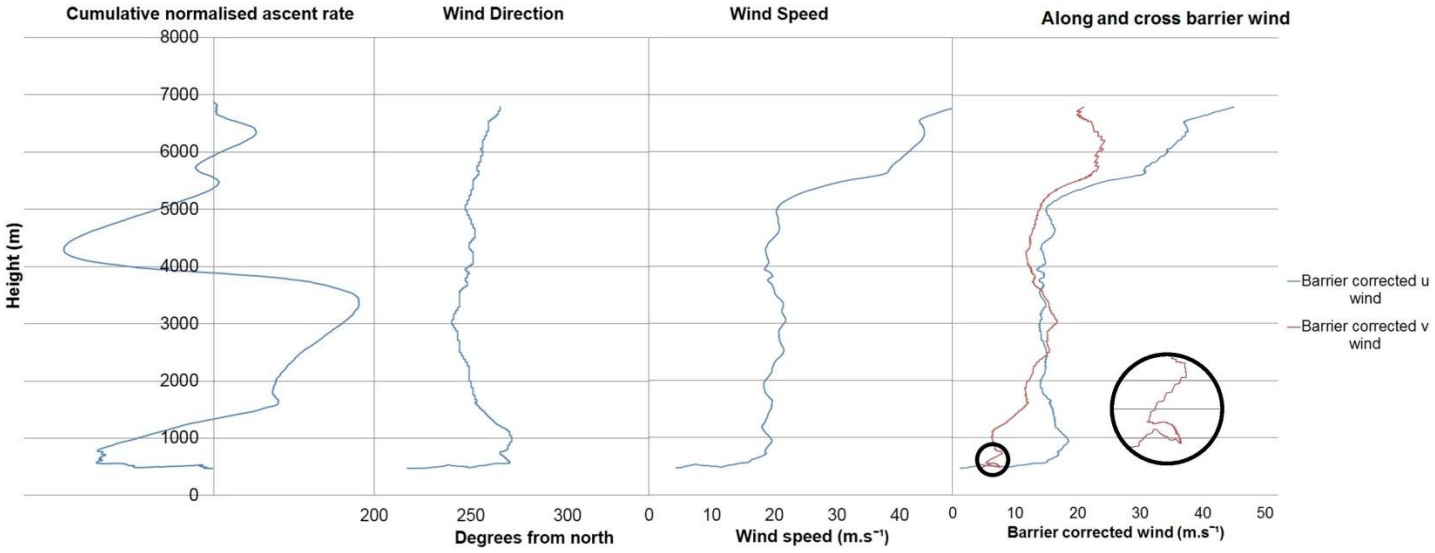

Figure 5 - 22: Gap radiosonde, on 8 June 2017, depicting wind direction, wind speed and the associated barrier corrected ù and ѵ winds with height. The barrier corrected ѵ wind speed, enlarged in the circle.

The Gap radiosonde, on 8 June 2017, produced a similar irregular potential temperature plot, suggesting another turbulent gap exit region. The first 3km of its flight, included localised updrafts in a dominant downdraft; at times losing up to 50m altitude over 500m horizontal distance. The downdrafts triggered a profile similar to a mountain wave loop sounding (section 5.2.2.3) as observed in Figure 5-22 and 5-23 (circled). This event also revealed the sharpest increase in wind speed, with a change from 4.3ms^{-1} at the surface to 18.8ms^{-1} at peak height (Figure 5-22 3rd graph from left). The Froude profile (Figure 5-23 left) demarcates multiple back-and-forth changes from supercritical to subcritical values; between 460 and 610m. Examining the potential temperature profile of the first 100m, a turbulent region is evident (Figure 5-23 right encirclement). Another out of the ordinary observation, which correlates with the above mentioned heights, is the ѵ wind speed increasing and decreasing (Figure 5-22 right); this change, exceeded the instrumentation bias and is a definite observation. An unexplained phenomenon, is the ѵ wind mimicking the cumulative normalised ascent rate above ridge height; a decrease in the ѵ wind speed correlates with the downdraft and an increase with the updraft.

In all events, the gap flow governing Bernoulli equations (Equation 2.7 & 2.8) yielded inaccurate wind speeds at the gap exit. This was because the colder blocked air produced a lower temperature at the entrance than at the exit; which is a reported

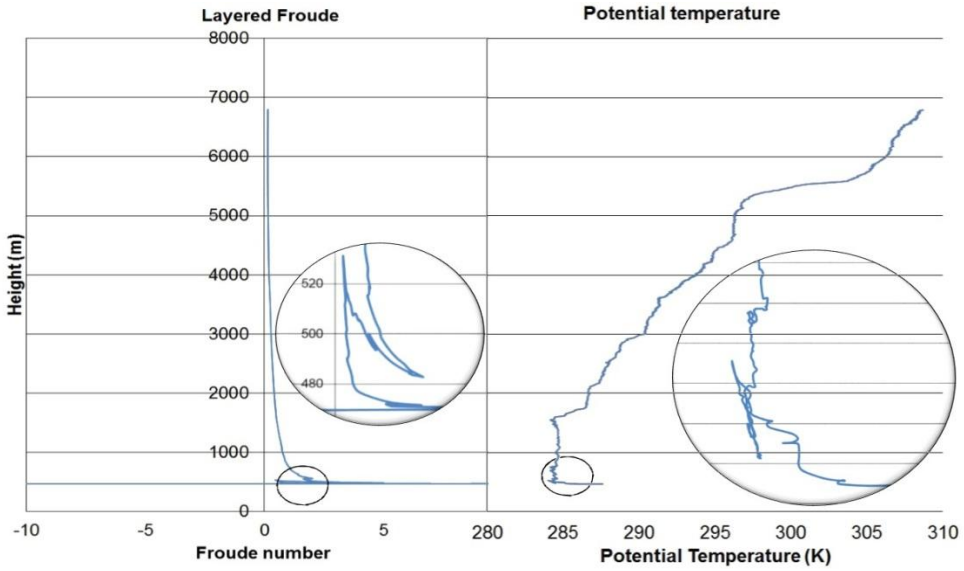

Figure 5 - 23: Layered Froude number and potential temperature, on 8 June 2017, plotted with height. The enlarged areas represent the encircled areas on the main graphs. Flow turned from supercritical to subcritical and back to supercritical at 510m, and finally back to subcritical at 610m.

weakness of the Bernoulli equation for compressible fluids (Gaberšek & Durran, 2004). The Bernoulli equation for incompressible fluids (Equation 2.7) performed better but underestimated the jet strength significantly, contrary to what Mass et al. (1995 cited in Gaberšek & Durran, 2004) suggested.

5.2.2.2.1 *Turbulence produced by gap flow*

On 26 October 2017, the two Gap radiosondes observed updraft and downdrafts in similar locations. The two radiosondes drifted at different altitudes and flight paths however, the onset and end of the downdrafts are at the same distance from the gap. The first Gap radiosonde, on 26 October 2017, produced a rapid ascent rate followed by its first downdraft at peak height (819m in Figure 5-14). The maximum updraft observed during this ascent, was 6.6ms^{-1}. Of all Gap radiosondes, the 8 June 2017 event observed the strongest downdraft; 6.8ms^{-1} at 517m. This peak downdraft was followed by a peak updraft observation of 4.5ms^{-1} at 527m. Such turbulent variations in updraft and downdrafts were not uncommon and were observed by multiple Gap radiosondes.

Not indicated, is the vorticity values that attained peak clockwise rotational values at 630m; measured from the second radiosonde on 26 October 2017. Observations of secondary and tertiary clockwise peak rotations were at 480 and 540m respectively. The peak clockwise rotational values, which coincided with subcritical Richardson values, suggest severe rotors or a hydraulic jump; again coinciding with the observations discussed in Figures 5-20 and 5-21. The first anti-clockwise rotational peak observation was shortly above mountaintop; this was identified as a rotor and is expectantly mountain wave or thermal related. Thermals generated by the warm northerly slope, interacting with colder air spilling over the mountain, have the capacity to produce a rotor. All three rotational areas portrayed peak turbulence values on the Ellrod Turbulence Index, which performed well in this case.

On 8 June 2017, Gap radiosondes were found to be the most turbulent. The radiosonde indicated extreme updraft and downdraft variations, the highest values of vorticity and contained a possible severe rotor. Van der Mescht (2012) suggested a constant potential temperature with height, peak rotational values and the Richardson number below 0.25, indicates a severe rotor. On 8 June 2017, the potential temperature remained constant up to 1600m (Figure 5-23 right); a chaotic vorticity region was indicated by multiple clockwise and anti-clockwise rotations with multiple Richardson values below 0.25 in the same layer. However, these observations extend to above mountaintop and suggests mountain waves interacted with the gap flow. In this event, the Ellrod Turbulence Index performed poorly, only highlighting the first 100m of the ascent as turbulent.

During the event of 8 June 2017, the downdrafts recorded in the gap region ($6.8ms^{-1}$) exceeded the downdrafts recorded above mountain height ($2.1ms^{-1}$), i.e. mountain wave induced. Even though 8 June 2017 was only a modest mountain wave event, it is evident that on occasions, gap flow produces more severe vertical velocities than mountain waves.

5.2.2.3 Mountain waves

On 26 October 2017, multiple variations of mountain waves are visible in all four timeslots in Figure 5-9. The morning mountain waves progress, with the average wind direction, while the afternoon mountain waves are observed to be stationary. The short morning mountain waves presumably form over the mountaintops, similar to mountain

waves over an isolated peak. As the day progresses the short mountain waves move away; with mountain waves taking a linear shape (Feltz et al., 2008). The stationary mountain waves mirror the orientation of the barrier, even though the wind direction is blowing at an angle of 50° - 80° from perpendicular (Figure 5-16 right); where 30° from perpendicular is the prescribed minimum requirement for mountain wave formation.

Multiple formation criteria are not met however, mountain waves are still observed. Apart from the undesirable wind direction (the winds were 50° - 80° from perpendicular; Figure 5-16 right), large wind directional shear (Figure 5-16) should have limited formation. Noted, is that not only the total wind speed but also the v̀ wind speed exceeds 7ms^{-1} from shortly above peak height to 2000m. The Scorer profile, the stability increase and the wavenumber criteria suggest trapped mountain waves below 2500m (bracket in Figure 5-15). The large increase in stability values at 2500m, suggest that minimal wave energy should be lost at the mountain wave reflection point. The surface stable layer is located in the blocking region and not a representation of the lee conditions; such a layer at ridge height would complete an almost perfect stability profile.

The Midvalley radiosonde (Figure 5-24) initially compares well to the Scorer profile (Figure 5-15 middle). The Midvalley radiosonde follows a steep updraft from the surface to 2500m (Figure 5-24 right) before going into a downdraft. The downdraft continued for ±500m horizontally and after a brief discontinuation of laminar flow, another updraft and a steep downdraft follow. Although the first mountain wave reflection point correlates to the Scorer profile, other mountain wave reflection points observed include 4000 and 5000m; suggesting non-trapped mountain waves (at least not trapped below 2500m). The radiosonde observed a peak upward ascent rate of 11.7ms^{-1} at 1450m, which translates to an updraft of 8.3ms^{-1}; after the mean balloon ascent rate was subtracted. In this event, the maximum mountain wave induced downdraft reached 3.3ms^{-1} at 3950m; which is consistent with the steepest part of the cumulative normalised ascent rate and peak vorticity values as seen in Figure 5-24. The Ellrod Turbulence Index highlights the peak downdraft area and the disruption of laminar flow between 2800 and 3200m as turbulent, contrary to the updraft area. Figure 5-24 again shows the v̀ wind speed increasing in the updraft and decreasing in the downdraft of the cumulative normalised ascent rate. Similarly, the ù wind speed deviates between 2500 and 4000m, with the combined effect resulting in the sharp deviation in the Midvalley balloon flight path, as in Figure 5-14.

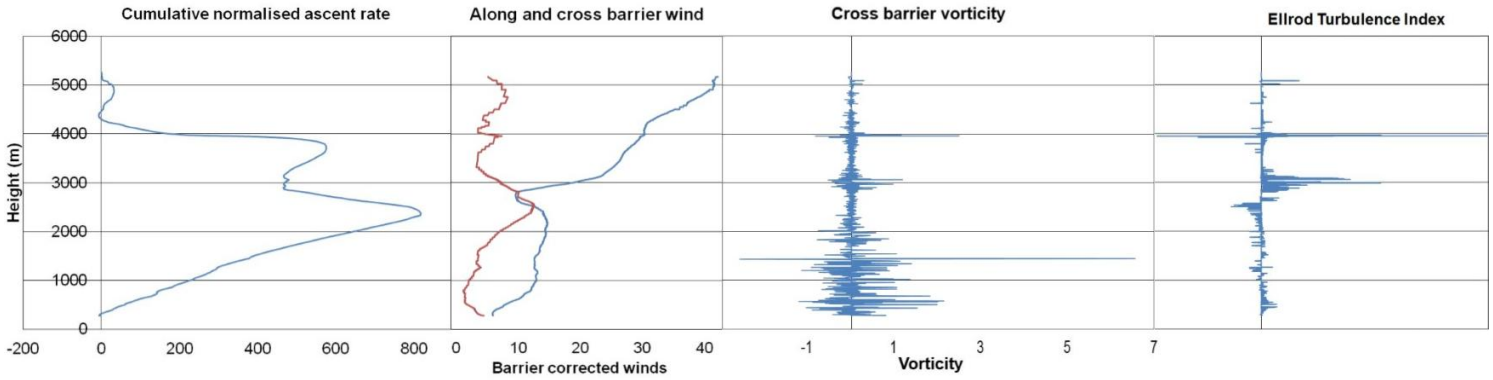

Figure 5 - 24: Midvalley radiosonde cumulative normalised ascent rate, ù (blue) and ѵ (red) winds, vorticity and the Ellrod Turbulence Index of 26 October 2017.

The Suuranys radiosonde shows similar updraft and downdrafts to the Midvalley radiosonde, although shorter lived with a smaller amplitude (Figure 5-25 left). Maximum updraft and downdraft values included 7 and 4ms^{-1} respectively. The Ellrod Turbulence Index suggested maximum turbulence values at 3300m with vorticity values peaking at multiple heights between 3000 and 4500m. The Suuranys radiosonde corresponded less with the Scorer parameter, with the mountain wave reflection point occurring at 2000m. Between 2000 and 3300m, the potential temperature indicates a deviation in normal flow with a non-uniform cumulative normalised ascent rate. This suggests an increase in turbulence however, vorticity values and the Ellrod Turbulence Index demarcates a non-rotating and non-turbulent flow. The cumulative normalised ascent rate indicates other possible mountain wave reflection points at 4000 and 5150m.

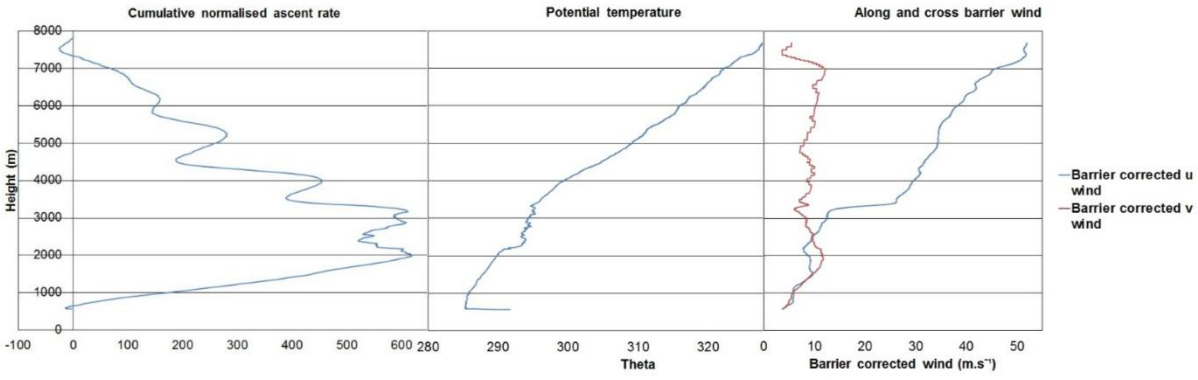

Figure 5 - 25: Cumulative normalized ascent rate, potential temperature, ù and ѵ winds of the Suuranys radiosonde on 26 October 2017.

On two mountain wave occasions, downdrafts induced radiosondes to lose height for prolonged periods; on 31 August and 13 December 2017. The double information at 4000m in Figure 5-26, on both skew-T's, are examples of radiosondes losing altitude. On 31 August 2017, an accidental slow ascending balloon was released measuring an average ascent rate of 0.8ms^{-1}. The low ascent rate made the radiosonde more susceptible to updraft and downdrafts, producing an interesting skew-T (Figure 5-26 left). Weak downdrafts of 4.6ms^{-1} resulted in the radiosonde to lose 630m of altitude over 4.5km (4400 to 3800m in Figure 5-27). Showers during the ascent rendered measurements questionable and possibly influenced by precipitation induced downdrafts. To eliminate the possibility of showers, the topography was plotted (blue line in Figure 5-27) below the radiosonde ascent rate. The topographical influence is evident and the radiosonde probed vertical propagating mountain waves above the individual ridges and downstream mountain waves. The radiosonde flight path shows mountain waves out of phase with the topography at 30 and 42km however, at 55km a mountain wave in-phase with topography is identified (radiosonde followed an almost exact profile of the surface ridge in Figure 5-27) and suggests a vertical wavelength of 3500m (Durran, 2013); when the surface is used as 1000m. Assuming the reduced ascent rate at 60km is mountain wave-induced, the primary and downstream mountain waves demonstrate crests at the same height. This infers equal amplitude and thus little to no energy loss in the downstream mountain wave. A conserved mountain wave is normally reflected by a strong inversion or strong wind speeds; in this instance a wind speed increase of 8ms^{-1} was identified as the responsible parameter that induced reflection. Another interesting feature is that, with exception of the mountain wave-induced drying of temperature on the skew-T, Figure 5-26 on the left can be regarded as unstable throughout; proving that stable conditions during mountain wave events are not a pre-requisite.

On 13 December 2017, a loop sounding is observed (note the loop in the parameters in Figure 5-28) by a Gap radiosonde penetrating a visible mountain wave (lenticular cloud on the main photo in Figure 5-29). The Gap radiosonde measured an average ascent rate of 2.5ms^{-1} and a maximum downdraft of 5.1ms^{-1} at 3800m; losing 200m altitude over 6.1km. In this event, updrafts in the gap region reached 6.7ms^{-1} and updrafts in a mountain wave reached 5.6ms^{-1} (3400m in Figure 5-28 left). Similar to 31 August 2017, the temperature warms and the dewpoint temperature decreases in the downdraft (Figure 5-26 right), simulating false stable areas at 1200 and 2500m. Another

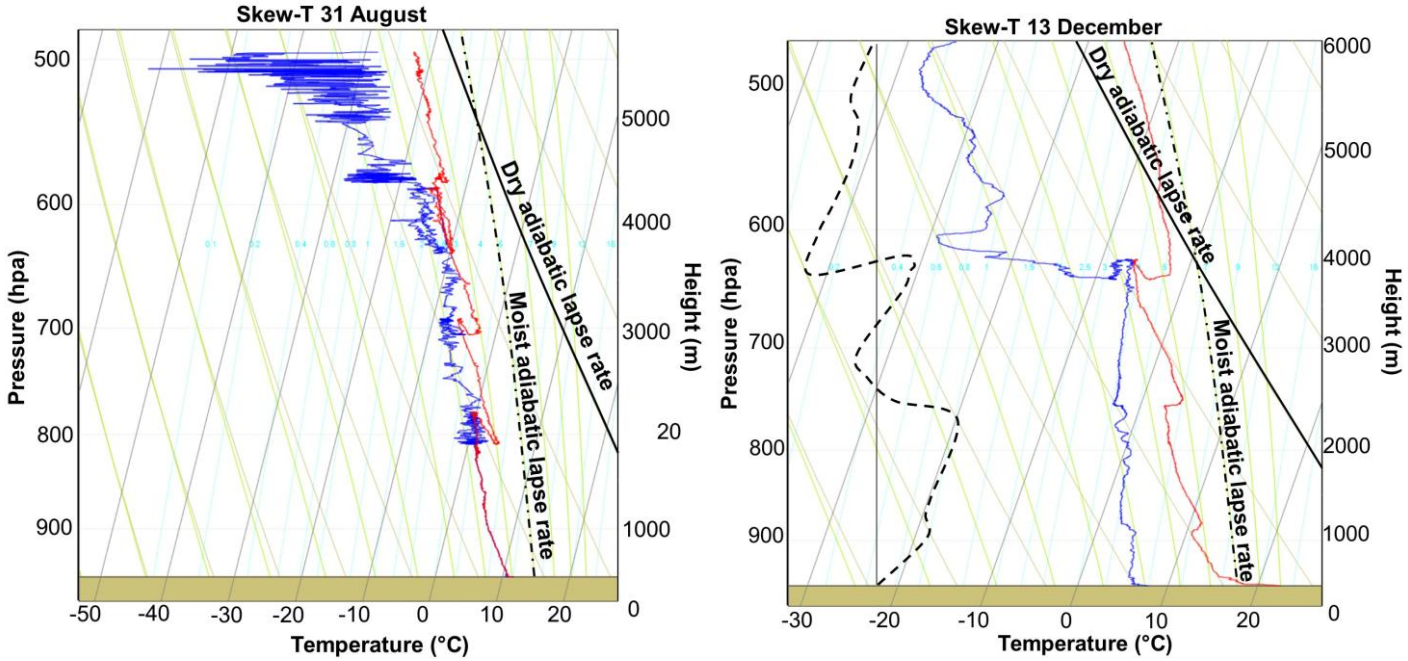

Figure 5 - 26: *Skew-T's of the Suuranys radiosonde on 31 August 2017 (left) and the Gap radiosonde on 13 December 2017 (right). The dotted line on 13 December 2017 demarcates the cumulative normalised ascent rate, indicating the updrafts (rightward slant) and downdrafts (leftward slant) of the ascent. The red line represents temperature and the blue line the dewpoint temperature. Note the warming of temperature in the downdrafts and the moistening of the profile in the updrafts.*

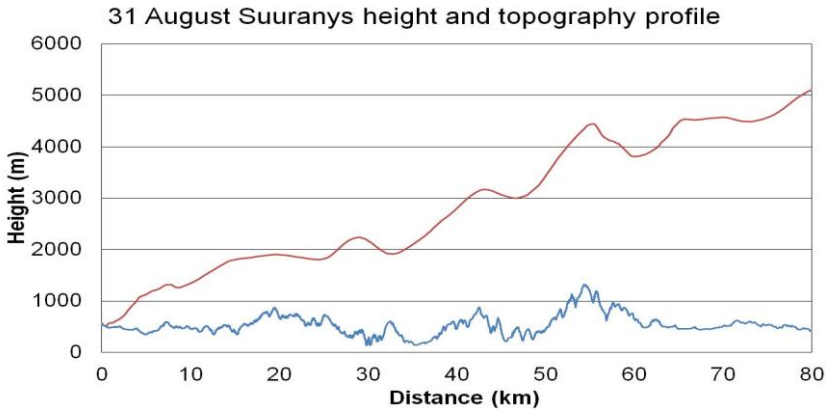

Figure 5 - 27: Altitude versus distance (red line) for 31 August 2017 Suuranys accidental low buoyancy balloon. The blue line represents the underlying topography below the radiosonde flight path.

observation on the skew-T is the temperature following the moist adiabatic line to the top of the updraft (even though the parcel is not saturated). This updraft renders the mountain

wave parcel of air more stable than the environment, resulting in the onset of a downdraft driven by the buoyancy force. In the downdraft, the parcels warm-up and follow the dry-adiabatic lapse rate (Figure 5-26 right). Studying the skew-T, multiple mixed layers are detected showing signs of a lifted mixing layer between 1000 – 2500m & 2500 – 3500m. These, reasonably well-mixed layers, highlight the importance of mountain waves in transporting air and momentum vertically.

In a mountain wave system, Van der Mescht (2012) observed maximum wind speeds halfway between the updraft and downdraft. On 31 August and 13 December 2017 (Figure 5-26 & 5-28), evidence of this exists with wind speeds initially increasing in the downdraft, becoming constant before decreasing as the downdraft near the end. In the updraft, a similar tendency is observed.

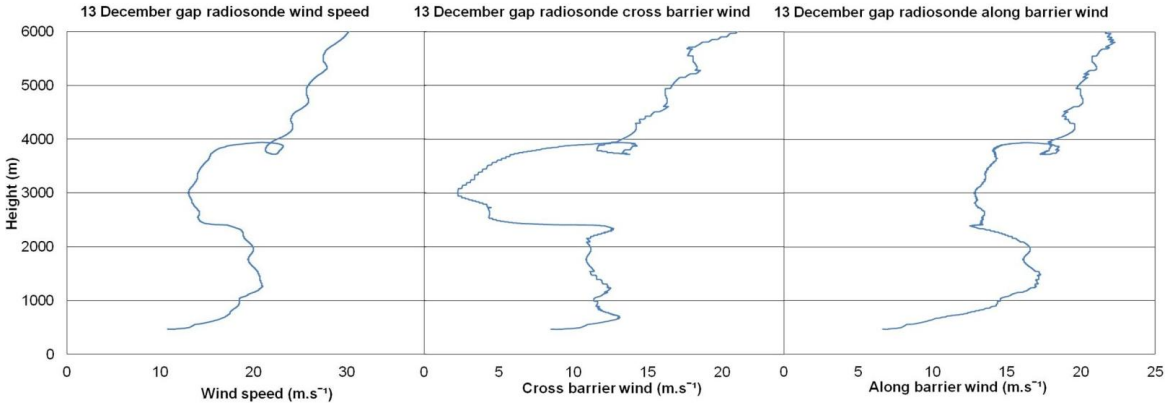

Figure 5 - 28: Wind speed and the barrier corrected winds (ù and ѵ) of the loop sounding of 13 December 2017; classified as such, due to the loop in the data at 3800m and not due to the radiosonde doing a physical loop.

On 13 December 2017, the mountain wave lost intensity downwind; as seen by the decrease in amplitude in the potential temperature plot of Figure 5-30. The wavelength of the system is arguably conserved which is evident by studying the distance between consecutive mountain wave peaks. The mountain waves generated by the Kareedouw ridge are not in-phase with the Suuranys ridge, due to the wave peak not directly above the Suuranys mountaintop. However, the downdraft descends in-phase with the Suuranys lee slope, as is seen in the downdraft hugging the lee slope of the Suuranys ridge. A shorter wavelength would have resulted in the location of the downdraft above the upwind rise of the Suuranys ridge; destroying the mountain wave system leaving only a turbulent area. On 13 December 2017, the Scorer parameter indicated trapped mountain waves below 3400m. The drop in altitude at 3800m (Figure 5-30 at 20-25km) is evidence that the

Scorer parameter did not accurately predict the vertical extent of the mountain wave system.

Figure 5 - 29: The main image depicts a visible lenticular mountain wave responsible for the drop in altitude on 13 December 2017. The photo views the mountain from the upwind side. Note how the different streamlines become visible and converge on top of the mountain wave. The three inset photos on top are from the same mountain wave system. The top left image depicts the start of Kelvin-Helmholtz waves on top of a mountain wave to the east of the main photo. The Kelvin-Helmholtz waves probably formed because of the streamlines converging on top of the mountain wave, resulting in instability in the system, as the more rapid wind speeds on top of the mountain wave and slower wind speeds in the mountain wave interact. The middle and right photos indicate lenticular clouds in the background with rotor clouds on the lee side of the Kareedouw ridge.

It is worth mentioning that during the 13 December 2017 event, a smoke grenade attached to the Gap radiosonde revealed a rotor rotating along a north to south axis. This rotor was observed visually below mountaintop (at approximating 700m amsl) and of which the rotation axis of this rotor, made the rotor unexpected. Deductive reasoning points that these rotors are still mountain wave related and probably attributed to the mountain waves observed at 09:15 on Figure 5-9. Calculating the vorticity values along this north to south axis, confirmed this unexpected and unexplained rotation during all events (with exception of 9 September 2017) between 764 and 805m.

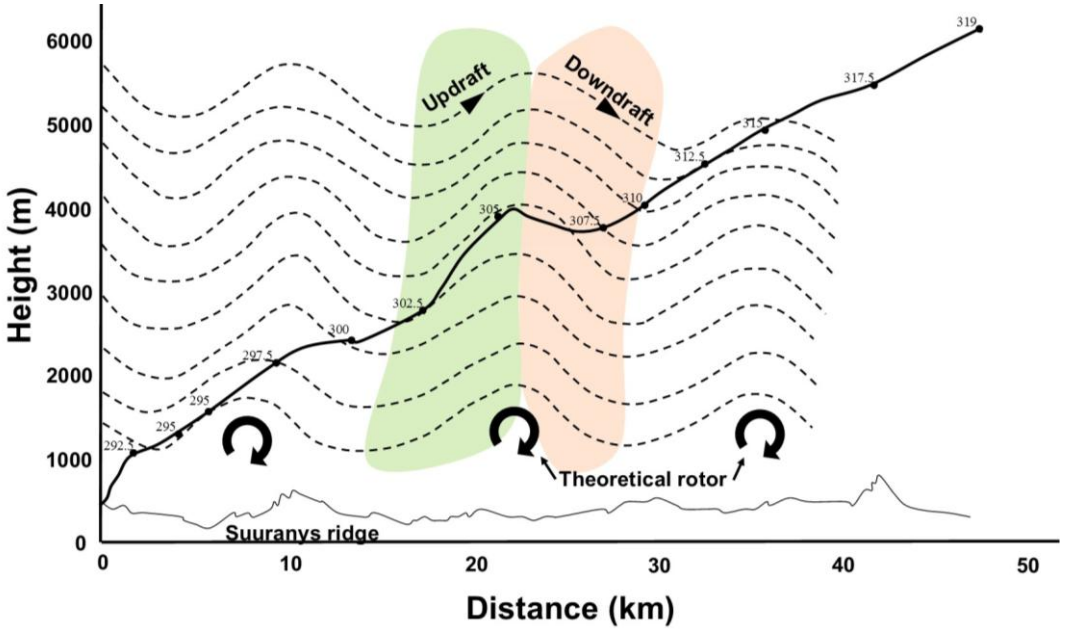

Figure 5 - 30: Potential temperature inferred plot of wind flow from the second Gap radiosonde on 13 December 2017. The plot was drawn by hand and suggests mountain waves (dashed line) triggered by the Kareedouw ridge, losing intensity downwind. The thick solid line demarcates the actual radiosonde flight path and the thin line, the underlying topography. The interpolated rotors as well as updrafts and downdrafts are indicated on the figure.

5.2.2.3.1 *Turbulence produced by mountain waves*

The severity of mountain waves, are linked by Grubišić & Lewis (2004) to vertical velocities, altitude variations and wavelength (see Table 2-2). Measuring the distance between mountain wave peaks on 26 October 2017 (bottom right inset in Figure 5-14), the Midvalley and the Suuranys radiosonde profiles indicate a wavelength of 8 and 15km. In order to measure this accurately, it is required that the radiosonde drifts perpendicular to the mountain waves so that the shortest distance between the crest and trough are measured. As the radiosondes drifted with the average wind direction and not perpendicular to the mountain waves, the derived wavelength cannot be trusted. Measuring the wavelength manually on satellite imagery yielded an 8-10km wavelength. In comparison, the Kareedouw ridge is 6-7km upwind of the Suuranys ridge in a southwesterly direction. The Grubišić & Lewis (2004) definition of the parameters measured on 26 October 2017 (wavelength = 8km, altitude variation = 1000m, updraft =

8.3ms^{-1} and downdraft = 6.8ms^{-1}) suggest moderate mountain waves. Classifying criteria of most events, revealed a dominant moderate mountain wave and at times a mixture of criteria falling in the severe category.

Rotors are another classifying factor for the severity of mountain waves. On 26 October 2017, a severe anti-clockwise rotor was observed at ridge height in the Gap radiosonde (see section 5.2.2.2.1). The Midvalley radiosonde could be used to identify a severe rotor at 1500m, 3000m and 4000m. The Ellrod Turbulence Index showed the rotors as turbulent, with exception of the midvalley rotor at 1500m.

5.3 SUMMARY

This chapter evaluated the data obtained during this project to characterise blocking, gap flow and mountain waves. All parameters mentioned in Chapter 2 and 3 were calculated and discussed. Event and AWS data were predominantly analysed separately. The 26 October 2017 event formed the basis of the event analysis, as it displayed a good spread of the three features. Other event data were only analysed if it portrayed a deviation from the information obtained from 26 October 2017. In this chapter blocking, gap flow and mountain waves were analysed individually to determine which feature produced the strongest wind, wind shear and the most turbulence. Chapter 6 combines the analysis and discussion of all three features as a combined system.

CHAPTER 6 : DISCUSSION

The complexities of real-life examples often result in features being individually analysed or simplified. There is no doubt that meteorological features are complex and influence one another, which makes individual analysis less accurate. In this chapter, the experiment design is discussed following into a discussion of the different features as a combined system. Closing this chapter, the analysed results are compared to other studies and discussed with regards to turbulence.

6.1 EXPERIMENT

The experimental phase revealed that careful consideration is required to optimally design an experiment. An in-depth study of theory and the environment needs to precede the design phase. The design is to be tested with smoke grenades in event conditions before the design is finalised. To determine the feasibility of the experiment, the equipment needs to be left in the field to observe an event. This is to determine whether all features are indeed observed. As Olivier & Rautenbach (2002) rightly states that accessibility is one of the most important factors when deciding where to place a measuring system. In this dissertation, the data from the best AWS location (Africa Peak AWS) proved fruitless; the reason being, it was inaccessible to visit frequently to determine functionality.

6.2 BLOCKING, GAP FLOW AND MOUNTAIN WAVE INTERACTION

The winds surrounding Cape St Francis (Figure 5-1, 5-2 and 5-12) indicate blocking jet characteristics downwind of the Kareedouw ridge; while Port Elizabeth winds do not. This suggests that the blocking jet (Figure 6-1) originates in the blocking regime and penetrates up to 30km downwind from its blocking barrier; similar to a gap jet penetrating downwind of its formation gap (Gaberšek & Durran, 2004). In this dissertation, a strong blocking jet that is 80km wide, and extends up to peak height (600m deep) is observed in the radiosonde data. The jet display similar characteristics to the Vancouver

Island in British Columbia, but simply on a larger scale (Overland & Bond, 1995). This blocking region positively and negatively influences the formation of both gap flow and mountain waves. The sea level pressure increase within the blocking region makes blocking the feature that exacts the greatest influence on its surroundings together with, enhancing the pressure gradient - driving gap flow. By applying the along-barrier momentum equation this pressure increase should be calculated in a follow-up study (Overland & Bond, 1995). Contrary to the blocking driving gap flow, the deflected blocking jet negatively impacts gap flow, by reducing the gap cross-sectional area exposed to the wind; resulting in gap wind speeds being slower than the blocked environmental wind speed. The v̀ wind (cross-barrier) marginally increases from the Upwind radiosonde to the Gap radiosonde, which indicates airflow through the gap; reducing the upwind pressure and thus weakening the blocking region (as the 26 October 2017 case depicts). It can be said that the blocking regime positively and negatively influences gap flow and in turn gap flow weakens the blocking regime.

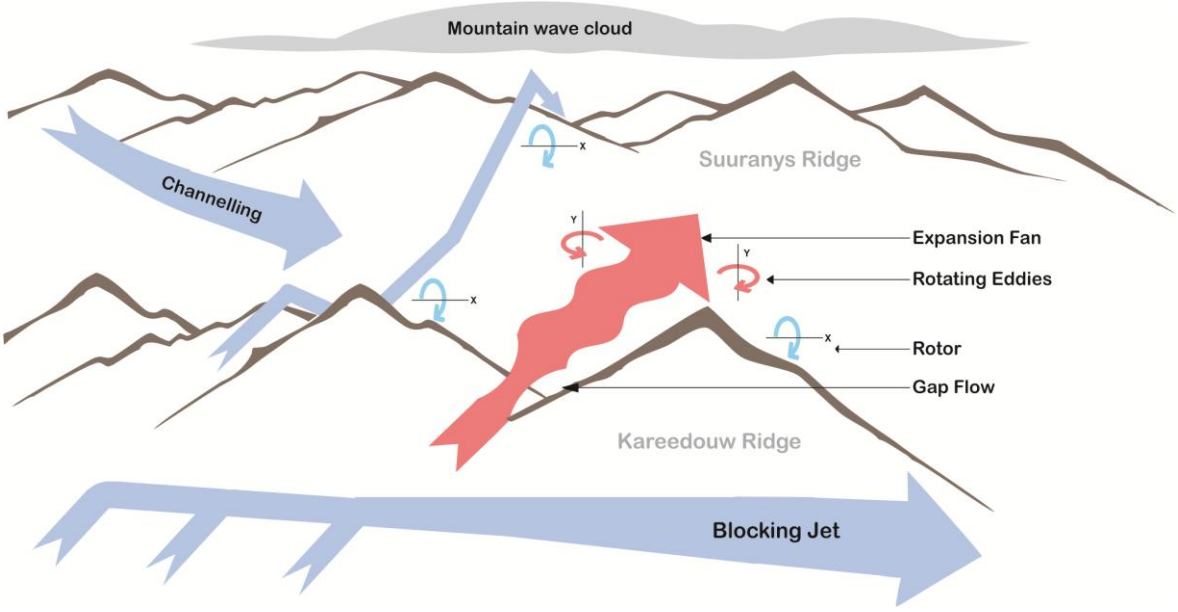

Figure 6 - 1: Flow processes observed in complex mountainous terrain.

Following the release, the Gap radiosondes followed one of two contradicting tendencies; either maximum updrafts were observed, or the radiosonde rapidly lost altitude. A radiosonde losing altitude combined with divergence is attributed to cold stable air spilling through the gap. At times the diverging flow is associated with changing Froude values, varying potential temperature values, a wind speed acceleration and multiple small updrafts and downdrafts; forming an expansion fan (Figure 6-1). Rapid

discontinuities in the ѵ wind profiles of Gap radiosondes, suggest gap flow swiftly changing to environmental conditions at the exit; this is usually associated with a hydraulic jump. Diverging cases, without rapid updrafts and downdrafts, are attributed to rotating eddies; originating from the gap divergence (red circular arrows in Figure 6-1). A more pronounced right (eastern) flank divergence is attributed to the channelled flow down the Langkloof valley, superimposing itself on the divergence. In this dissertation it was found that the gap jet seemed uninfluenced by mountain waves; contrary to what most studies suggest (Gaberšek & Durran, 2004). Probable explanations for this is likely the small scale topography, the gaps within this ridge, the dynamic barrier of the blocking region and/or the unstable conditions surrounding the study site.

Mountain waves were not influenced by gap flow but by rather by the blocking regime. The blocking regime presents a dynamic barrier (Neiman et al., 2010); and in experiements conducted in this dissertation the dynamic barrier transition zone lies in the area of rapid wind direction and speed changes above the ridge height (Figure 5-16). Air approaching the coast is forced to rise above the dynamic barrier, which ends abruptly and is walled by the mountain barrier. At ridge height, along-barrier blocked flow (hence the unfavourable mountain wave formation wind direction at ridge height) and the air above the dynamic barrier, accelerates downward into transitional flow (Figure 2-4); forming a mountain wave, similar to Feltz et al. (2008). The observations in this dissertation clearly indicate that the incident wind direction, during mountain wave formation, is not important. It is the theory that any cross-barrier wind speed (ѵ) exceeding $7ms^{-1}$, will result in mountain wave formation. This theory explains the formation of the cap cloud, but not the development of downstream mountain waves parallel to the barrier. The author is of the opinion that the unexplained variations in the ѵ wind speed, during mountain wave updrafts and downdrafts (discussed in section 5.2.2.1.1), possibly contribute to this. The multiple different forms of mountain waves observed, is consistent with literature on broad spectrum mountain waves (Smith & Kruse, 2017). It would be interesting comparing the momentum fluxes of the respective waves.

None of the events resulted in more than three downstream mountain wave clouds on satellite imagery; indicative of a low energy mountain wave system. The low energy system is attributed to; a less than perfect incident wind direction, large wind direction changes with height and no pronounced increase in stability at the ridge height. Mountain waves are observed in unstable conditions, but there seems to be a limit on the instability

that a mountain wave system can handle. For example, in the vicinity of cold unstable frontal showers, satellite imagery depicted mountain waves disappearing, however, only to re-appear shortly after the shower moved off. Even in these low energy mountain waves, parameters indicate severe rotors (Figure 6-1); associated with severe turbulence below the ridge height.

6.3 EVALUATION OF BLOCKING, GAP FLOW AND MOUNTAIN WAVE PARAMETERS

The different fluid dynamical equations exhibited variable stages of success. The Froude derived height scale and the Froude number proved accurate, if compared to radiosonde measured wind direction and wind speed. The Burger equation was useful but not required. Both Bernoulli equations, governing gap flow, proved less useful. Analysing the equations, a lower temperature in the blocking region (than the gap exit region) and air spilling, rather than funnelling into the gap, renders the equations not useful. The gradient windroses (Figure 5-3 and 5-4) clearly state the influence of the temperature gradient and pressure gradient on the gap wind direction and wind speed. Strong gradients would predominantly occur during strong synoptic conditions and weak gradients during weaker synoptic conditions; driving gap flow. Lack of satellite altimetry data made the evaluation of the blocking parameters: thermal wind equation and the Rossby Radius equation, difficult.

The mountain wave Scorer parameter and the wave trapping condition performed poorly. The poor performance is attributed to the airmass being a mixture of stable and unstable layers and the close vicinity to the cold fronts. It is known that the Brunt-Väisälä frequency is undefined in unstable layers, however, due to the lack of other parameters; the frequency was nevertheless incorporated in the calculations of all parameters – producing uncertainty in the calculations. The moist Brunt-Väisälä parameter (Durran & Klemp, 1982) also did not render useful results. As Feltz et al. (2008) rightly mentions in the vicinity of a cold front, airmasses are continuously changing. This changing environment renders the Scorer parameter calculated from a single ascent not useful.

6.4 COMPARISON TO OTHER STUDIES

The *blocking* regime correlated well with what Parish (1982) and Neiman et al. (2010) observed in the Sierra Nevada region. The ѵ wind speed mostly increases (Figure 2-2) from the surface to well above the mountaintop and the ù wind strength always peaks below or at the mountaintop. This increase in ѵ wind speed with height, is attributed to the barrier deflecting less flow; as an increase in height produces a less continuous barrier (more gaps in the barrier).

In this dissertation, the strongest *gap flow* jet ($21ms^{-1}$), was observed below mountaintop on 31 August 2017. The highest wind speed increase in the gap ($15ms^{-1}$ over 250m) and the greatest wind direction change (55° over 100m); relating to the most turbulence, was observed on 8 June 2017. These observations reveals that this gap jet is the weakest gap jet (which is again attributed to the upwind blocking jet reducing the cross-sectional area of the gap); when compared to other studies (Table 2-1). However, the large wind direction and wind speed changes from upwind into the gap and to the lee-side, indicates gap flow is still significant and deserves further investigation.

To the knowledge of the author, these *mountain waves* are the most severe mountain waves measured up to date in South Africa; when classified according to vertical velocities. This shows that mountain waves originating in an unfavourable environment can be of equal or greater intensity to mountain waves forming over larger topographical areas and in more favourable atmospheric conditions. Mountain waves in a non-idealised environment, similar to the mountain waves in this dissertation, are thought of as more severe – as it is less predictable and often unexpected by pilot and forecaster.

6.5 TURBULENCE

The blocking region exhibits the strongest winds, also interestingly enough, the least turbulence. The constant increase in wind direction and wind speed (Figure 5-11, 5-12 & 5-13), throughout the blocking layer, ensures no disruptions in flow. Above the blocking region, large changes in wind direction and wind speed are observed; indicating a turbulent region. A pilot should remain below the transition zone (changing from blocking to environmental conditions – usually below ridge height) to avoid turbulence.

Wind speeds in the gap flow regime are weaker than in the blocking regime. However, gap flow produced significant wind direction and wind speed changes. Turbulence was also identified by the Ellrod Turbulence Index, Vorticity values and the Richardson number. The large variety of features observed and its contrasting nature results in the gap region to be a complex area and best avoided by pilots.

Broadly speaking results from this dissertation show that mountain waves and gap flow produce equally severe downdrafts. Occasionally, gap flow induced vertical velocities, exceeds mountain wave induced vertical velocities posing a greater hazard. However, in mountain waves, these vertical velocities exist over larger areas; influencing aircraft over a longer and more widespread area. In combination with the mountain waves, multiple observed severe rotors pose a hazard.

To distinguish between the features responsible for turbulence below ridge height remains difficult. No direct influence of gap flow could be found on mountain waves, however, turbulence generated from gap flow does interact with mountain wave features. Similarly, mountain wave induced rotors and downdrafts influences gap flow; at times, muddling everything below mountain ridge as turbulent and again best avoided by pilots.

The Ellrod Turbulent Index performed reasonably well in resolving the turbulent areas. The Richardson number as a standalone parameter, as used by Doyle et al. (2009) and Van der Mescht & Eloff (2013), was less practical. The parameter produced a lot of noise when applied to fine resolution data and highlighted turbulent areas throughout the atmosphere. The ascent rate as used by Van der Mesht & Eloff (2013) and Grubišić & Billings (2007) yields too much data which then becomes noise, rather than being interpretable. The cumulateive normalised ascent rate was a good solution to this and proved usefull in data analysis and interpretation. Although radiosondes and AWSs were sufficient in this experiment, no length scale could be measured for turbulent eddies. Fluid mechanics suggest the Reynolds number to quantify turbulence, however without the length scale this and the eddy dissipation rate cannot be calculated.

6.5.1 Forecasting mountain wave and its associated turbulence

This dissertation identifies stability and wind direction of lesser importance to mountain wave formation. Any cross-barrier wind component (v̀) exceeding $7ms^{-1}$ can result in mountain wave formation; even if the wind exists some distance above ridge

height. Wind direction changes and stability is found not to negatively impact on the severity of mountain waves, however, it does impact the range that this feature extends downwind. A frontal tail, almost parallel to the coast, greatly assisted in the forecasting of these mountain waves – even when model winds and stability were indicating unfavourable conditions. This is significant as this mountain run from west to east and perpendicular to what the International Civil Aviation Organization suggests. Contradicting another suggestion by literature is that these cold fronts seemed responsible for formation, rather than causing the breaking-up of the trapped mountain waves.

Classifying severity of mountain waves with regards to wavelength and amplitude is not useful. Results in this dissertation indicate that mountain waves with a short wavelength produced greater vertical velocities than those with a longer wavelength. It is concluded in this dissertation that all mountain waves are severe, regardless of formation conditions, topography and shape of mountain waves; especially in the vicinity of topography.

6.6 SUMMARY

Directional shear is described to have a compounding effect on wind shear (Ellrod & Knapp, 1992), thus in this dissertation, blocking is defined as the least turbulent and the gap the most turbulent regime. In this environment, the three regimes cannot be looked at in isolation, but all needs to be considered together for a consolidated picture.

CHAPTER 7 : CONCLUSIONS AND RECOMMENDATIONS

7.1 INTRODUCTION

On 16 December 2015, there was a light aircraft crash, near a gap in the mountains close to Kareedouw, which sparked the research in this dissertation. Personal communication with the pilot of this aircraft revealed that he found himself unconscious after a sudden onset of turbulence, approximately 2km downwind of the final crash site. A mountain wave or its associated rotor was likely responsible for the burst of turbulence the pilot experienced. As the aircraft crash site was a further 2km upwind of the initial turbulence, it is theorised that one of the passengers took control of the aircraft before it crashed. The crash site was immediately upwind of the gap exit, where the wing first impacted the valley side ridge. It is likely that the passenger lost control within the gap; in the area that is now identified as a significantly turbulent gap region. No observations were available 16 December 2015 but the measurements done on 8 June 2017, as part of the research for this dissertation, describe similar meteorological conditions. In this instance, an aircraft flying at 500m, planning to exit through the gap from the lee side to the upwind side, would have observed a wind direction and wind speed change from 220° at 4.5ms^{-1} to 280° at 25ms^{-1}. Such a wind change will result in severe turbulence and will be sufficient to bring down an experienced pilot.

The ridge (Africa Peak) measured the maximum wind speed in the cases investigated as part of this research. The maximum wind speed forms as the compressional effect above the mountain increases the pressure gradient force, which dominates the frictional force, ultimately leading to a stronger wind. The blocking region was the second strongest wind speed region and the jet that protruded the furthest downwind of its exit region. Gap flow measured weaker than the ridge and blocking region, but measured stronger than the lee side surface wind speeds. However, the most turbulence-producing feature was; gap flow, followed by mountain waves and lastly blocking.

In this dissertation, blocking, gap flow and mountain waves were analysed with the help of AWSs data (taken over a year between 2017/2018) and radiosondes data (of six

events within the same period). Observations of gap flow and blocking were evident in both radiosonde and AWS data but observations of mountain waves were only evident in radiosonde data. Automatic weather station data successfully captured gap flow, where across-barrier temperature and pressure gradients as well as blocked air spilling through the gap were the main driving forces. Radiosonde data captured blocking; where cold southwesterly winds from the vicinity of the cold front over the ocean, was the driving force. All events showed some indication of blocking and all, but one event observed mountain waves. Mountain waves were mostly short-lived and two events dissipated before all measurements were completed. This dissertation highlights the hazard that small-scale mountain waves pose to aviation and emphasises the lack of knowledge on this feature near unstable airmasses and small-scale topography. Other lesser important mountain wave characteristics observed in this study were; the deviation of the v̀ wind in the updraft and downdraft (mimicking the cumulative normalised ascent rate) and the important role mountain waves can play at distributing air vertically; changing the surrounding conditions and the vertical temperature and dewpoint profiles (as in Figure 5-26).

Even though gap flow was more successfully characterised using AWS measurements, radiosonde measurements highlighted some interesting features associated with gap flow. Contrasting features were measured from the gap exit; two events observed a feature simulating an expansion fan, two radiosondes measured extreme updrafts within the gap (exceeding mountain wave updraft measurements), and the remaining radiosondes lost altitude in a diverging flight path from the exit. The important conclusion is that all features within the gap region are turbulent and dangerous for the aviation sector.

This dissertation does not go into depth of the application of the results to other sectors, such as the renewable energy sector. However, briefly, the consistency of the wind in the gap, combined with the stronger flow at night, transforms this into an optimal location for supplementing a micro-energy production network. The stronger flow at night would supplement the energy deficiency left by the day dependent solar panels; making the micro-network more viable.

The different objectives of this dissertation lead to the following conclusions:

7.1.1 Objective 1: Experiment design

The experiment designed for this dissertation was successful in measuring blocking, gap flow and mountain waves. The data obtained from the experiment successfully characterised the features and allowed preliminary insight into how the different features interact. However, to obtain an even better understanding of these interactions, some improvements to the experiment design are required:

- This experiment was insufficient to effectively measure and resolve fine-scale features such as expansion fans, diverging eddies and rotors. Given the severity of these features, further in-depth studies are required with better equipment.
- The link between the evolution of the blocking, gap flow and mountain wave regimes are such that a constant area monitoring is required in order to understand their correlation to one another. A Doppler RADAR or LIDAR will be perfectly suited for such a study.
- Creative thinking is encouraged in designing an experiment such as this. For example, smoke or dronesondes can add a new aspect to a project while reducing the costs involved.
- Consider the equipment bias if fine-scale features are expected.
- To optimise data, observational events and the expected satellite pass-overs are to be synchronised. In this dissertation, only one event had satellite altimetry winds available; this greatly inhibited the blocking analysis.
- The experiments conducted as part of this research rendered very much data, all of which have not been examined to its full potential. Future field studies, such as this, should consider that the number of events does not have to be vast but that a few events might already provide insight into the phenomena.

To design an effective experiment, requires the consideration of many factors. To initiate the experiment design, it is required to answer the 6 W's of design:

- Why – Why is this important? Will the results warrant the financials and time required to complete the study?

- Who – Who can assist with this study? Who can benefit from this study? Who are the relevant role-players? From whom do you need to get permission to do the experiment? Who did similar work, and what can you learn from them?
- What – What will be measured? What features and processes will follow from this? What is required to characterise these features? What are the initial conditions, and do this need to be measured?
- Where – Where is the optimal location to measure these features and what are the limiting factors (such as accessibility)? Where does what equipment need to be placed?
- When – When will this take place? How long will the experiment last? How frequent is this phenomenon observed? When are you most likely to have optimal results? Is a preliminary study required in order to understand when and where the phenomenon is expected?
- Whereby – By which methods and means will this be achieved? How will this project be completed?

Smoke should be deployed before the experiment design and if possible after the final design. This will greatly assist in designing an experiment and to test the rationale of the experiment.

7.1.2 Objective 2: Analyse data using parameters

The data were successfully analysed using parameters to identify and characterise the different features. However, some parameters proved not useful in the analysis. Fluid dynamics successfully characterised blocking with parameters such as, the Froude number, Burger number and the Froude derived height scale. The Burger number was useful but was not required; as the Froude number already described the flow successfully. Insufficient altimetry data limited the testing of the thermal wind equation and the Rossby Radius equation. Gap flow parameters performed poorly where the pressure increase and temperature decrease in the blocking region rendered the Bernoulli equation unusable. Another possible explanation can be that flow in the gap is turbulent and the Bernoulli equation is only valid for steady flow. In weaker temperature gradients, wind direction and wind speed in the gap agree better with the thermal wind theory. Additional investigation is required to determine the feasibility of using temperature and pressure gradients to characterise gap flow. The night-time inversion positively accelerates the

wind speed within the gap, as one can expect from the Venturi-effect. Mountain wave parameters were mostly unsuccessful in characterising mountain waves. The Brunt-Väisälä parameter, only defined for stable conditions, resulted in an inaccurate Scorer parameter during most of the events, as the atmosphere was unstable. Not applying the Scorer parameter contradicts all that literature suggest. For occasions when the relative humidity was greater than 80%, the moist Brunt-Väisälä parameter (Durran & Klemp, 1982) was tested; but this also did not render useful results.

Turbulence indicating parameters, such as the Ellrod Turbulence Index, proved accurate while the vorticity equation proved useful in highlighting rotors and unexplained rotations. The Richardson number, contrary to what literature suggest, was unusable as a standalone parameter. The potential temperature plots and the cumulative normalised ascent rates proved extremely helpful to highlight a disruption in laminar flow.

7.1.3 Objective 3: Determine and compare the characteristics of blocking, gap flow and mountain waves, to other studies.

All events in this dissertation had some indication of blocking; even the most unfavourable event of 13 September 2017. Blocking was easily identified in the data and was comparable to other studies. When compared to literature (Table 2-1), this study was the only study where the gap jet was weaker than the upwind conditions. However, gap flow is evident in the data and was created by a different mechanism than most other studies; spilling from the upwind/blocking regime. Although the physical gap jet is weak, the features emanating from the gap exit (updrafts, downdrafts, divergence, expansion fan and horizontal rotating eddies; which frequently interacts with vertical rotating rotors) were significant. This identifies the gap region as the most turbulent region. The observation of mountain waves compared favourably to other studies and the vertical velocities were the strongest ever measured in a South African study (Van der Mescht & Eloff, 2013 and Cronje & Van der Mescht, 2013).

In this study, blocking drives gap flow by increasing the pressure and decreasing the temperature. Hereby blocking drives gap flow through the pressure gradient force and the thermal wind. Gap flow in turn weakens the blocking region by decreasing the upwind pressure when air spills to the lee-side. Blocking also influenced and contributed to mountain wave formation through a dynamic barrier. Gap flow features interacted with

mountain wave induced rotors, however, no physical influence was found on the mountain wave itself.

7.2 CONTRIBUTION TO THE FORECASTING OF TURBULENCE

Mountain wave formation criteria were revisited in this dissertation, contrasting the recommendations by Reichman (1978), Van der Mescht (2012), Barry (1981) and International Civil Aviation Organization (2005). It was determined that in mountain wave forecasting, it is best not to eliminate mountain waves when the air is unstable. Furthermore, the cross-barrier wind speed (v̀) in the vicinity of the peak is more useful than considering the total wind speed and wind direction. In this study, all mountain wave events occurred when the cross-barrier wind speed exceeded $7ms^{-1}$, however, it is unknown whether a lighter cross-barrier wind speed will also induce mountain waves. A finding was that a mixture of different airmasses and weather systems limits mountain wave formation. The interaction of cool onshore air, behind a coastal low, and the warm dry northwesterly Föhn-type wind, limited mountain wave formation. Cold fronts frequently triggered mountain waves over this west to east mountain barrier, especially if the tail of the front becomes more parallel to the coast. Unstable conditions were found to positively influence the formation of irregular complex mountain waves (as Bradbury (1991) suggested); which has been found by Uhlenbrock et al. (2006) to be more severe than linear mountain waves. According to the broad-spectrum wave theory, a similar finding is that unstable conditions trigger mountain waves off the individual ridges and peaks (short spectrum of waves) where more stable conditions trigger waves over the entire ridge (longer spectrum of waves) (Smith & Kruse, 2017 and Van der Mescht & Geldenhuys, 2017).

The author is of the meaning that simplistic forecasting of mountain wave severity is not possible. Merely classifying the severity of mountain waves, according to; wavelength, altitude variation and vertical velocities proved inadequate in this dissertation. Relying on turbulence indices to highlight all mountain wave related turbulence and its intensity also failed at times. The International Civil Aviation Organisation (ICAO) agrees that mountain wave forecasting is possible, but it remains difficult to forecast the severity of the turbulence associated with this. The ICAO suggest that a nomogram can be effective at forecasting the intensity of mountain waves; using a sea-level pressure

difference across the ridge and the cross-barrier wind speed (ν) as predictors (International Civil Aviation Organization, 2005). A numerical weather prediction product is another possible solution to attempt to forecast the severity of mountain waves.

The area below ridge height on the lee side of any mountain is best avoided by aircraft and regarded as turbulent. It is a recommendation to keep a ground clearance of at least 1.5-2 times the highest topography; in a 10km upwind radius. This will not result in total turbulence avoidance, but provide the pilot with additional time to react and minimise the expected turbulence to mountain wave turbulence only; and not a compounding effect between different features.

In conclusion, in real life, one cannot look at wind flow in complex terrain simplistically. The three features namely; blocking, gap flow and mountain waves are intertwined and cannot be seen as separate processes.

7.3 RECOMMENDATIONS

Conducting a field experiment, such as in this dissertation, is expensive. One way of limiting the cost is to analyse the data from the first experiment thoroughly in order to determine if additional data are required and to identify the shortcomings in the experiment design. Dronesoundings can provide a new dimension to experimental studies and definitely requires further investigation. In future experimental studies, different sectors should work together, as an interdisciplinary team, in order to optimise the funds available and the applicability of the data. This dissertation could easily have benefited from the input of experts from other fields, in order to ensure that the data are more applicable and widely used.

In order to fully understand the life cycle of blocking and the features at the gap exit, high-resolution area observations are required; with a low instrumentation bias (for example a LIDAR/Doppler RADAR). Given the poor understanding of blocking in South Africa and its impact on the other features and on the surface pressure, it deserves further attention and a follow-up study. Gap flow requires an investigation during weak synoptic conditions to ascertain the effect of the nocturnal inversion and to correlate the effect of the weak synoptic conditions with the strong synoptic conditions effect. Mountain wave parameters require refinement for an unstable environment. A nomogram, to determine the severity of mountain waves, can greatly contribute to the tools of a forecaster. The

unexpected rotors, attributed to the west to east moving mountain waves (09:15 Figure 5-9), observed in the smoke and the vorticity data, deserves an in-depth study. Lastly, an interesting study would test the influence of the mountain-wave-induced lifted mixing layer (similar to Figure 5-23) on the formation of severe thunderstorms.

7.4 SCIENTIFIC CONTRIBUTION

This project was a first of its kind in South Africa. The design of the experiment and the failures leading up to the design will be beneficial for other experimental based studies. Furthermore, the onset of the process to develop the dronesonde has the capability to largely impact in future experimental studies. Not only was this the first gap flow and blocking study in South Africa, it was the first study to look into the interaction of the three features. Numerical weather prediction commonly misses some finer scale features, which are then unaccounted for by many applications, studies and forecasters. Observational studies similar to this one act to question and validate the small-scale features (such as the expansion fan) observed in dynamical studies and modelling studies. A new approach, contrasting existing literature, is revealed to forecasting mountain waves on the forecasting desk. Some findings of this dissertation are widely applicable and to numerous applications, such as; the renewable energy sector, agriculture and aviation industry.

REFERENCES

Ahmad, N. & Proctor, F., n.d. *Estimation of Eddy Dissipation Rates from Mesoscale Model Simulations,* Hampton: American Institute of Aeronautics and Astronautics.

American Meteorological Society, 2012. *Glossary of Meteorology 2nd ed.* [Online] [Accessed 22 02 2016]. Available at:

http://amsglossary.allenpress.com/glossary

Australian Government, 2014. *Staying safe against in-flight turbulence.* 2nd ed. s.l.:Australian Transport Safety Bureau.

Australian Transport Safety Bureau, 2000. *Australian Government Australian Transport Safety Bureau.* [Online] [Accessed 17 May 2017]. Available at:

https://www.atsb.gov.au/publications/2009/mountain-wave-and-associated-turbulence/

Barry, R., 1981. *Mountain Weather and Climate.* London: Methuen & Co.

Bond, N. & Macklin, S., 1992. Aircraft observations of offshore-directed flow near Wide Bay, Alaska. *Monthly Weather Review ,* Volume 121, p. 150–161.

Bradbury, 1991. Wind shear and waves. *Sailplane & Gliding*, August-September, pp. 178-182.

Bradbury, T., 1992a. Sailplanes and Gliding. *Skywatch - A Beginners Guide to Clouds Part 4*, August-September, pp. 210-215.

Bradbury, T., 1992b. Sailplane and Gliding. *Skywatch - A Beginners Guide to Clouds*, October-November, pp. 256-260.

Brennan, M., Cobb III, H. & Knabb, R., 2010. Observations of Gulf of Tehuantepec Gap Wind Events from QuickSCAT: An updated Event Climatology and Operational Model Evaluation. *Weather and Forecasting,* Volume 25, pp. 646-658.

CAA, n.d. *Civil Aviation Authority Aircraft Accident Report and Executive Summary,* s.l.: CA 18/2/3/9286.

Caccia, J., Benech, B. & Klaus, V., 1997. Space–Time Description of Nonstationary Trapped Lee Waves Using ST Radars, Aircraft, and Constant Volume Balloons during the PYREX Experiment. *Journal of the Atmospheric Sciences,* 54(14), pp. 1821-1833.

Campbell Scientific, 2018. *Campbell Scientific.* [Online] [Accessed 16 02 2018]. Available at:

https://www.campbellsci.co.za

Carter, T., 2005. *The evolution of coastal lows along the South Coast of South Africa,* KwaDlangezwa: University of Zululand.

Chen, W. & Smith, R., 1987. Blocking and deflection of airflow by the Alps. *Monthly Weather Review,* 115(November), pp. 2578-2597.

Colle, B. A. & Mass, C. F., 1996. An observational and modelling study of the interaction of low-level southwesterly flow with the Olympic Mountains during COAST IOP4. *Mon. Wea. Rev.,* Volume 124, p. 2152–2175.

Colle, B. A. & Mass, C. F., 1998. Windstorms along the western side of the Washington Cascade Mountains. Part I: A high resolution observational and modeling study of the 12 February 1995 event. *Monthly Weather Review,* Volume 126, p. 28–52.

Colle, B. A. & Mass, C. F., 2000. High-Resolution Observations and Numerical Simulations of Easterly Gap Flow through the Strait of Juan de Fuca on 9-10 December 1995. *Monthly Weather Review,* Volume 128, pp. 2398-2422.

Colman, B. & Dierking, C., 1992. The Taku wind of southeast Alaska: Its identification and prediction. *Weather Forecasting,* Volume 7, p. 49–64.

Cronje, J. & Van der Mescht, D., 2013. *Investigating limiting conditions in mountain wave rotor formation: an experimental approach applied to the Outeniqua Mountains in the George Region of South Africa.* Durban, 29th Annual Conference of South African Society for Atmospheric Sciences.

De Foy, B., Clappier, A., Molina, L. & Molina, M., 2006. Distinct wind convergence patterns in the Mexico City basin due to the interaction of the gap winds with the synoptic flow. *Atmospheric Chemistry and Physics,* Volume 6, pp. 1249-1265.

De Villiers, M. & Van Heerden, J., 2001. Clear air turbulence over South Africa. *Meteorological Applications,* Volume 8, pp. 119-126.

Doyle, J. D.; Grubišić, V.; Brown, W.O.J.; De Wekker, S.F.J.; Dörnbrack, A.; Jiang, Q.; Mayor, S.D.; Weissmann, M., 2009. Observations and Numerical Simulations of Subrotor Vortices During T-REX. *Journal of the Atmospheric Sciences,* Volume 66, p. 1229–1249.

Drobinski, P., Dusek, J. & Flamant, C., 2001. Diagnostics of hydraulic jump and gap flow in stratified flows over topography. *Boundary-Layer Meteorology,* Volume 98, pp. 475-495.

Durran, D., 2013. Lee Waves and Mountain Waves. *University of Washington.*

Durran, D. & Klemp, J., 1982. On the Effects of Moisture on the Brunt-Väisälä Frequency. *Journal of the Atmospheric Sciences,* 39(October), pp. 2152-2158.

Ellrod, 1992. *A northern hemisphere clear air turbulence.* Vienna, American Meteorological Society, pp. 444-448.

Ellrod, G. & Knapp, D., 1992. Forecasting Techniques - An Objective Clear-Air Turbulence Forecasting Technique: Verification and Operational Use. *Weather and Forecasting,* Volume 7, pp. 150-165.

Federal Aviation Administration, n.d. *Wake Turbulence Training Aid,* s.l.: Federal Aviation Administration.

Feltz, W.F; Bedka, J.A; Otkin, J.A; Greenwald, T; Ackerman, S.A, 2008. Understanding Satellite-Observed Mountain-Wave Signatures Using High-Resolution Numerical Model Data. *Weather and Forecasting,* Volume 24, pp. 76-86.

Fett, R., 1993. The Kamishak gap wind as depicted in DMSP OLS and SSM/I data. *International Journal of Remote Sensing,* Volume 14, p. 403–423.

Finnigan, T.D.; ne, J.A.; Jackson, P.L.; Allen, S.E.; Lawrence, G.A.; Steyn, D.G., 1994. Hydraulic physical modeling and observations of a severe gap wind. *Monthly Weather Review,* Volume 122, p. 2677–2687.

Gaberšek, S. & Durran, D., 2004. Gap Flows through Idealized Topography. Part I: Forcing by Large-Scale Winds in the Non-Rotating Limit. *Journal of the Atmospheric Sciences,* Volume 61, pp. 2846-2862.

Grubišić, V. & Billings, B., 2007. The Intense Lee-Wave Rotor Event of Sierra Rotors IOP 8. *Journal of Atmospheric Sciences,* 64(December 2007), pp. 4178-4201.

Grubišić, V. & Lewis, J., 2004. Sierra Wave Project revisited: 50 years later. *Bulletin of the American Meteorological Association ,* Volume 85, pp. 1127 - 1142.

Hertenstein, R. & Kuettner, J., 2005. Rotor types associated with steep lee topography: influence of the wind profile. *Tellus,* Volume 57A, pp. 117-135.

Hurd, W., 1929. Northers of the Gulf of Tehuantepec. *Monthly Weather Review,* Volume 57, pp. 192-194.

InterMet Africa Systems, 2016. *InterMet Africa International Met Systems.* [Online] [Accessed 16 02 2018]. Available at:

https://www.intermetafrica.co.za/radiosondes/imet-2/

International Civil Aviation Organization, 2005. *Manual on Low-level Wind Shear,* s.l.: s.n.

International Civil Aviation Organization, 2007. *Meteorological Service for International Navigation,* s.l.: 16th Edition.

Jackson, P. & Steyn, D., 1994. Gap winds in a fjord. Part II: Hydraulic analog. *Monthly Weather Review,* Volume 122, p. 2666–2676.

Jansa, A., 1987. Distribution of the mistral: A satellite observation. *Meteorological Atmospheric Physics,* Volume 36, p. 201–214.

Kaufmann, P. & Weber, R., 1996. Classification of mesoscale wind fields in the MISTRAL field experiment. *Journal of Applied Meteorology,* Volume 35, p. 1963–1979.

Lackmann, G. & Overland, J., 1989. Atmospheric structure and momentum balance during a gap-wind event in Shelikof Strait, Alaska. *Monthly Weather Review ,* Volume 117, p. 1817–1833.

Landman, S., 2016. *Convective Scale Workshop.* s.l.:South African Weather Service.

Leeb-du-Toit, 2006. *Cloudbase: a reference manual for glider pilots,.* Worcester: Cape Gliding Club.

Macklin, S., Bond, N. & Walker, J., 1990. Structure of a low-level jet over lower Cook Inlet, Alaska. *Monthly Weather Review,* Volume 118, p. 2568–2578.

Macklin, S.A.; Overland, J.E.; Walker, J.P., 1984. *Low-level gap winds in Shelikof Strait. Proc.* Miami, FL, American Meteorological Society, p. 97–102.

Marić, T. & Durran, D., 2009. Observations of Gap Flow in the Wipp Valley on 20 October 1999: Evidence of Subsidence. *Journal of Atmospheric Sciences,* Volume 66, pp. 984-1000.

Marwitz, J. & Dawson, P., 1984. Low-level airflow in southern Wyoming during wintertime. *Monthly Weather Review,* Volume 112, p. 1246–1262.

Mass, C., Businger, S., Albright, M. & Tucker, Z., 1995. A windstorm in the lee of a gap in a coastal mountain barrier. *Monthly Weather Review,* Volume 123, p. 315–331.

Masson, V. & Bougeault, P., 1996. Numerical simulation of low level wind created by complex orography: A Cierzo case study. *Monthly Weather Review,* Volume 124, p. 701–715.

MC Systems, 2010. *MC Systems.* [Online] [Accessed 16 02 2018]. Available at: https://www.mcsystems.co.za/html/mcs_151.html

McAneny, K., Baille, A. & Sappe, G., 1988. Turbulence measurements during mistral winds with a 1-dimensional sonic anemometer. *Boundary-Layer Meteorology,* Volume 42, p. 153–166.

Nance, B. & Durran, D., 1997. A Modeling Study of Nonstationary Trapped Mountain Lee Waves. Part 1: Mean-Flow Variability. *Journal of Atmospheric Sciences,* Volume 54, pp. 2275-2291.

Neiman, P., Sukovich, E., Ralph, F. & Hughes, M., 2010. A Seven-Year Wind Profiler-Based Climatology of the Windward Barrier Jet along California's Northern Sierra Nevada. *Monthly Weather Review,* 138(April 2010), pp. 1206-1232.

Olivier, J. & Rautenbach, C.J., 2002. The implementation of fog water collection systems. *Atmospheric Research ,* Volume 64 , p. 227 – 238.

Overland, J., 1984. Scale Analysis of Marine Winds in Straits and along Mountainous Coasts. *Monthly Weather Review,* Volume 112, pp. 2530-2534.

Overland, J. & Bond, N., 1995. Observations and Scale Analysis of Coastal Wind Jets. *Monthly Weather Review,* Volume 123, pp. 2934-2941.

Pan, F. & Smith, R., 1999. Gap Winds and Wakes: SAR Observations and Numerical Simulations. *Journal of the Atmospheric Sciences,* 56(7), pp. 905-922.

Parish, T., 1982. Barrier winds along the Sierra Nevada Mountains. *Journal of Applied Meteorology,* Volume 21, pp. 925-930.

Pettre, P., 1982. On the problem of violent valley winds. *Journal of Atmospheric Sciences,* Volume 39, p. 542–554.

Pierrehumbert, R. & Wyman, B., 1985. Upslope Effect of Mesoscale mountains. *Journal of Atmospheric Sciences,* 42(10), pp. 997-1003.

Preston-Whyte, R. & P.D, T., 1988. *The Atmosphere and Weather of Southern Africa.* s.l.:Oxford University Press.

Ramachandran, G., Rao, K. & Krishna, K., 1980. An observational study of the boundary-layer winds in the exit region of a mountain gap. *Journal of Applied Meteorology,* Volume 19, p. 881–888.

Reed, T. R., 1931. Gap winds of the strait of Juan de Fuca. *Monthly Weather Review,* Volume 59, p. 373–376.

Reed, R., 1981. A case study of a Bora-like windstorm in western Washington. *Monthly Weather Review,* Volume 109, p. 2382–2393.

Reichman, H., 1978. *Cross-country Soaring.* s.l.:Thomson Publications.

RM Young, 2018. *Young.* [Online] [Accessed 16 02 2018]. Available at: http://www.youngusa.com

Saito, K., 1992. Shallow Water Flow HAving a Lee Hydraulic Jump over a Mountain Range in a Channel of Variable Width. *Journal of the Meteorological Society of Japan,* 70(June, No. 3), pp. 775-782.

Scorer, R., 1952. Mountain-gap winds: A study of surface wind at Gibraltar. *Quarterly Journal of the Royal Meteorological Society,* Volume 78, p. 53–61.

Smith, R., 1987. Aerial observations of the Yugoslavian bora. *Journal of Atmospheric Sciences,* Volume 44, p. 269–297.

Smith, R., Gleason, A., Gluhosky, P. & Grubišić, V., 1997. The wake of St. Vincent. *Journal of Atmospheric Sciences,* Volume 54, pp. 606-623.

Smith, R. & Grubišić, V., 1993. Aerial Observations of Hawaii's Wake. *Journal of Atmospheric Sciences,* 50(22), pp. 3728-3750.

Smith, R. & Kruse, C., 2017. Broad-spectrum Mountain Waves. *Journal of the Atmospheric Sciences,* Volume 74, pp. 1381-1402.

Smutz, S., 1986. *A climatology of the Sierra Nevada barrier jet. M.S. thesis paper AS-153.,* Laramie, Wyoming: Deptartment of Atmospheric Science, University of Wyoming.

Stiperski, I. & Grubišić, V., 2010. Trapped Lee Wave Interference in the Presence of Surface Friction. *Journal of the Atmospheric Sciences,* Volume 68, pp. 918-936.

Suarez, A. & Stauffer, D., n.d. *Effects of nonstationary wave structures on rotor development and evolution.* State College, Pennsylvania State University.

The COMET Program, 2017. *Eumetrain.* [Online] [Accessed 15 02 2018]. Available at: http://www.eumetrain.org/data/4/452/print_4.htm

UCAR, 2012. *Atmospheric Dust.* s.l.:COMET program, University Corporation for Atmospheric Research.

Uhlenbrock, N., Bedka, K., Feltz, W. & Ackerman, S., 2006. Mountain Wave Signatures in MODIS 6.7-μm Imagery and Their Relation to Pilot Reports of Turbulence. *Forecaster's Forum, Weather and Forecasting,* Volume 22, pp. 662-670.

University of Washington, 2014. *Navy Mesoscale Primer: Gap Winds.* Washington: Department of Atmospheric Sciences, University of Washington.

Van der Mescht, D., 2012. *Mountain wave turbulence in the lee of the Hex River Mountains,* Stellenbosch: Masters Disertation, Stellenbosch University, Department of Geography and Environmental Studies.

Van der Mescht, D. & Eloff, P., 2013. Mountain wave-induced rotors in the lee of the Hex River Mountains. *South African Geographical Journal,* 95(1), pp. 117-131.

Van der Mescht, D. & Geldenhuys, M., 2017. *Mountain waves observed in the lee of the Tsitsikamma Mountains.* Polokwane, South African Society of Atmospheric Sciences.

Wallace, J. & Hobbs, P., 2006. *Atmospheric Science: An Introductory Survey.* 2nd ed. s.l.:Elsevier.

Winant, C., Dorman, C., Friehe, C. & Beardsley, R., 1988. The marine layer off northern California: An example of supercritical channel flow. *Journal of Atmospheric Sciences,* Volume 45, p. 3588–3605.

Zängl, G., 2002. Stratified flow over a mountain with a gap: Linear theory and numerical simulations. *Quarterly Journal of Royal Meteorological Society,* Volume 128, pp. 927-949.